Dissertation

Accurate and Low-complexity Ray Tracing Channel Modeling

ausgeführt zum Zwecke der Erlangung des akademischen Grades
eines Doktors der technischen Wissenschaften

eingereicht an der
Technischen Universität Wien
Fakultät für Elektrotechnik und Informationstechnik

von
Mingming Gan

Wien, 20. November 2015

TECHNISCHE
UNIVERSITÄT
WIEN
Vienna University of Technology

Supervisor
Priv.-Doz. Dr.techn. Thomas Zemen
Digital Safety and Security Department
AIT Austrian Institute of Technology, Wien, Austria

Examiner
Prof. Claude Oestges
Institute of Information and Communication Technologies,
Electronics and Applied Mathematics (ICTEAM)
Ecole Polytechnique de Louvain, Louvain-la-Neuve, Belgium

and

Prof. Christoph Mecklenbräuker
Institut für Nachrichtentechnik und Hochfrequenztechnik
Technische Universität Wien, Wien, Austria

Abstract

The characterization of the wireless propagation channel provides the fundamental basis for wireless communications, determining the performance of practical systems. In last decades, the dramatically increasing demand for wireless system capabilities makes the study of the propagation channel become indispensable. An accurate and low-complexity channel model is of high importance for developing next generation wireless systems. Until now, there are mainly three modeling methods: empirical, statistical and deterministic models. The latter uses the geometric and electromagnetic description for a site-specific environment to evaluate the propagation paths based on geometrical optic techniques. Ray tracing (RT), a deterministic propagation prediction tool, has been widely used to simulate channel characteristics in indoor and outdoor environments. To date, RT tools include not only specular reflection, penetration through dielectric blocks and diffraction, but also diffuse scattering mechanisms. The accuracy, provided by a detailed modeling of the environment, comes at the cost of a high computational complexity, which directly scales with the number of considered propagation paths.

The goal of my thesis is to reduce the computational complexity of RT with no loss in accuracy. There are three scenarios included: wideband indoor, ultra-wideband (UWB) indoor and tunnel scenarios. A three-dimensional (3D) RT tool used in the thesis is based on the pre-existent RT tool, which was implemented in C programming language by Université catholique de Louvain, Belgium. Firstly, the RT tool is re-implemented in MATLAB, which is named conventional RT in the thesis. For the sake of accelerating the execution of the RT tool, the code is optimized through converting time-consuming algorithms to Matlab executable (MEX) functions by using MATLAB Coder. The speeding up efforts focus on reflection and diffuse scattering calculations, because the number of reflection and diffuse scattering propagation paths comprise a large proportion among all propagation paths. Compared with conventional RT, the simulation time of the revised MATLAB code is significantly reduced.

Moreover, the reduction of computational complexity of RT is considered not only for one terminal position but also for multiple mobile terminal positions in this thesis. For one terminal position, an efficient approach to generate diffuse scattering

tiles based on concentric circles is developed and evaluated for a wideband indoor scenario. It is known that channel characteristics may vary significantly over the entire bandwidth for an UWB indoor scenario. To cope with this, sub-band divided ray tracing (SDRT) has been proposed for one terminal position. However, the computational complexity is directly proportional to the number of sub-bands. Therefore, I propose a mathematical method by making SDRT almost independent of the number of sub-bands, which is named low-complexity SDRT. In addition, RT combining with a higher-order reflection algorithm is developed for intelligent transport system (ITS) in tunnel scenarios.

While simulating the radio propagation conditions for a mobile terminal, communicating in a frame based communication system indoors with several fixed nodes, the correlated temporal and spatial evolution of the channel impulse response (CIR) is of utmost concern. A RT algorithm and a low-complexity SDRT algorithm based on two-dimensional discrete prolate spheroidal (DPS) sequences is proposed for wideband and UWB indoor scenarios, respectively. In tunnel scenarios, a non-stationary vehicle-to-vehicle (V2V) channel model combining propagation graphs with RT is proposed. I include the time evolution of relevant channel parameters in the proposed model depending on the stationary time region, which are obtained based on the local scattering function (LSF).

Furthermore, the accuracy of RT is strictly limited by the available description of the environment. Based on the low-complexity SDRT implementation, I also propose a calibration method for indoor UWB low-complexity SDRT. The method estimates the optimal material parameters, including the dielectric parameters and the scattering parameters, using channel measurements and multiobjective simulated annealing (MOSA).

Finally, the accuracy of all proposed algorithms is verified by numeric simulations or measurement campaigns. The evaluation includes the power delay profile (PDP), root mean square (RMS) delay spread, angular spread, and RMS Doppler spread. Due to the complicated implementation of RT, it is hard to obtain a closed-form expression for the computational complexity. Therefore, I evaluate the simulation time of my proposed algorithms. In conclusion, all the proposed algorithms in this thesis can help to reduce the computational complexity of RT significantly.

Acknowledgement

First and foremost, I would like to express my deepest gratitude to my supervisor Priv.-Doz. Dr. Thomas Zemen for offering me the great opportunity to pursue the doctor study in Vienna. I am grateful for his endless trust, support and encouragement during my last five years' doctor study. Without his continuous help, this thesis would never have become real. I am extremely fortunate to have a supervisor who cares not only about my work but also my life in a foreign country. I also would like to thank Prof. Claude Oestges and Prof. Christoph Mecklenbräuker for their insightful discussions and precious suggestions on my publications, and for finding some time in their busy schedules to be my examiners reviewing my doctor work.

I owe my deepest gratitude to Dr. Nicolai Czink and Dr. Francesco Mani for their guidance, patience and encouragement during the beginning phase of my thesis work; to Prof. Fredrik Tufvesson for recommending me the opportunity to work at FTW and his fruitful discussions about my ideas; to Prof. Franz Hlawatsch for his interesting lectures and thoughtful advices; to those I was lucky enough to work with, Prof. Klaus Witrisal, Prof. Troels Pedersen, Prof. Florian Kaltenberger, Dr. Paul Meissner, Dr. Gerhard Steinböck, MSc. Erik Leitinger, and MSc. Markus Fröhle, for their entertaining discussions and argumentations, most importantly, for making the cooperative work enjoyable; to Prof. Zhangdui Zhong, Prof. Bo Ai, Prof. Ke Guan and Prof. Ruisi He for interesting academic discussions and the comprehensive introduction about the Chinese research status on related fields.

I also would like to thank FTW for providing me with the good working environment and network to successfully develop as a researcher. I am thankful to all my colleagues for their friendly support and highly pleasant atmosphere at FTW. Especially to MSc. Sanda Drakulic for always "pulling" me back to work at the right point; to MSc. Zhinan Xu, with whom I always had heated discussions, which made our cooperative work highly productive; to Dr. Driton Statovci and Dr. Martin Wolkerstorfer, with whom I had the pleasure to work with; to MSc. Markus Hofer, MSc. Thomas Paulin, Dr. Arian Bär and Dr. Laura Bernadó for their kindly help when I met some trifles. Not only what I learnt from all of you but also for making the office a place I was looking forward to go everyday.

I would also like to thank all friends at Vienna of the so-called "Chinese maffia".

Specially Qi Wang and Xuan Chen, you were my foothold in good and also in distressing times. Also, without Yutong Ji, Shuping Dai, Xinlin Yan, Chen Wang, Qian Xu, Hua Zhou, Boyu Zhang, Xu Gao and Da Pan, my life in Vienna would not have been as enjoyable and fun as it has been. Furthermore, I am also grateful to my students at Chinese school for the joyful time we spent together during last four years.

Although I have left my home country China quite some years ago, I am also deeply grateful to my friends Jing Wu, Liying Wan, Shuting Wang, Yufei Zuo, Xuejiao Gou, Jigong Qi, Tao An, Yingjie Liu and Yu Cao for never stopping believing in me all the time, as this encouraged me to believe in myself to achieve my objectives.

Last but not least, I am immensely grateful to all important people in my life, especially to my family in China. To my parents and sister, for their understanding and support through these years, despite having no clue about what I do, no words can express my gratitude.

Contents

List of Figures

List of Tables

Acronyms

2D	two-dimensional
3D	three-dimensional
AoA	azimuth of arrival
AZB	angular Z-buffer
BER	bit error rate
CIR	channel impulse response
CPU	central processing unit
CTF	channel transfer function
DoA	direction of arrival
DoD	direction of departure
DPS	discrete prolate spheroidal
DSD	Doppler power spectral density
EoA	elevation of arrival
ER	effective roughness
FDTD	finite difference time domain
GO	geometrical optics
GPU	graphical processing units
GSCM	geometry-based stochastic channel model
GTD	geometrical theory of diffraction

IP	interaction point
ISB	incident shadow boundary
ITS	intelligent transport system
LOS	line-of-sight
LSF	local scattering function
MEX	Matlab executable
MIMO	multiple-input multiple-output
mmW	millimeter wave
MD	mobile discrete
MIMO	multiple-input multiple-output
MoM	method of moments
MOSA	multiobjective simulated annealing
MRE	mean relative error
MSE	mean square error
NLOS	non-line-of-sight
OFDM	orthogonal frequency division multiplexing
PDP	power delay profile
PEC	perfect electric conductor
PRA	parallel ray approximation
RMS	root mean square
RSB	reflection shadow boundary
RT	ray tracing
Rx	receiver
SD	static discrete

SDRT	sub-band divided ray tracing
SoCE	sum of complex exponentials
TDL	tap-delay line
Tx	transmitter
UTD	uniform theory of diffraction
UWB	ultra-wideband
V2V	vehicle-to-vehicle
VNA	vector network analyzer

1 Introduction

The fundamental problem of communication is that of reproducing at one point either exactly or approximately a message transmitted at another point [3]. A schematic diagram of a general communication system presenting this concept is shown in Fig. 1.1. The communication channel is the transmission medium linking the transmitter (Tx) and receiver (Rx). For wireless communications, the transmission medium is the radio channel between the Tx and the Rx. The Tx and the Rx antennas may or may not be considered as a part of the radio channel depending on the wireless system under consideration.

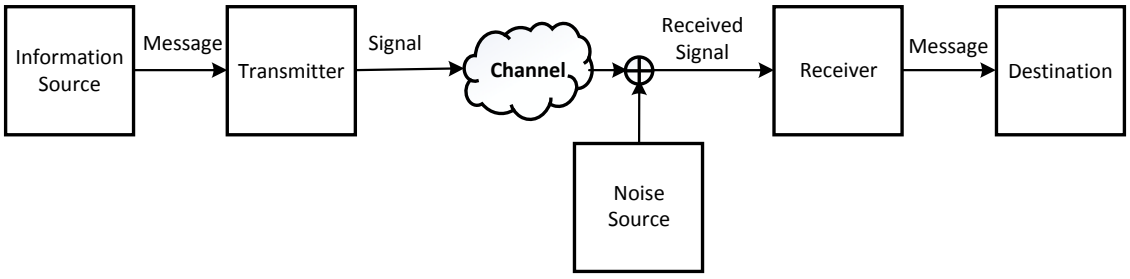

Figure 1.1: Diagram of a general communication system.

The radio channel takes into account multiple effects which are generated by the signal - an electromagnetic wave interacting with the surrounding environment of the wireless communication system. These multiple effects are considered as multipath propagation. In some cases, a line-of-sight (LOS) connection may exist between the Tx and the Rx. Besides the LOS path, mechanisms behind electromagnetic propagation are diverse, but can generally be attributed to reflection, diffraction, and diffuse scattering [4]. A simple plot of multipath propagation is shown in Fig. 1.2. Each propagation path has its distinct amplitude, delay - the run time of the electromagnetic wave, direction of departure (DoD) at the Tx, and direction of arrival (DoA) at the Rx [1].

The channel properties play an important role in determining the information-theoretic capacity and the specific wireless system behavior. In last decades, the

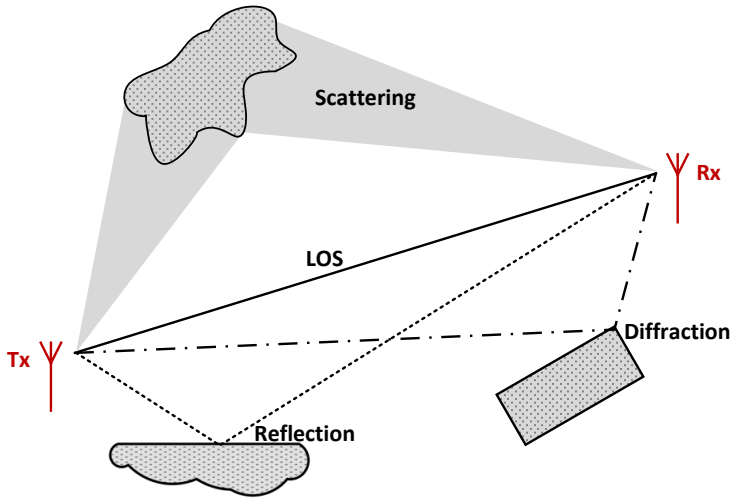

Figure 1.2: Simple plot of multipath propagation.

evolution of wireless communications has been accelerated at an extraordinary pace to fulfill modern lifestyle requirements. In order to keep pace with this ever-increasing demand, the study of new wireless communication standards is indispensable for increasing data rate and maximizing the utilization of the limited spectrum. The currently proposed 5G [5], the main technologies of which are massive multiple-input multiple-output (MIMO) and millimeter wave (mmW) systems, aims at providing unlimited access to information and sharing data anywhere, anytime by anyone and anything for the benefit of people, businesses and society. The performance of these technologies is highly determined by wireless propagation channels. Therefore, it is essential to know and understand the behavior of wireless channels.

In order to characterize the property of wireless channels, there are two approaches: i) propagation channel measurements and ii) channel models. Propagation channel measurements are usually applied for capturing the temporal and spatial behavior of wireless channels. However, performing channel measurements is a complicated process that requires huge data storage, significant financial resources, and manpower efforts [6]. Therefore, for the design, simulation and planning of wireless communication systems, channel models reflecting the important properties of wireless channels are widely needed.

1.1 Background

In this section, I briefly present the channel characteristics, which are relevant for designing wireless communication systems. Moreover, I give a general overview of channel models.

1.1.1 Channel Characteristics

As the starting point, the simplest possible scenario is considered: one Tx and one Rx antenna in free space. In this case, the received power P_{Rx} by the Rx antenna can be expressed as a function of the distance d between the Tx and the Rx in free space, which is also known as ***Friis's law***, defined as [1]

$$P_{\mathrm{Rx}}(d) = P_{\mathrm{Tx}} G_{\mathrm{Tx}} G_{\mathrm{Rx}} L_{\mathrm{fs}}, \tag{1.1}$$

where P_{Tx} is the transmitted power, G_{Tx} and G_{Rx} are the Tx and Rx antenna gains, and L_{fs} is the free space loss factor, respectively. L_{fs} is expressed as

$$L_{\mathrm{fs}} = \left(\frac{4\pi d}{\lambda}\right)^2, \tag{1.2}$$

where λ is the wavelength. The validity of Friis's law is restricted to the far field of the antenna. In general, ***path loss*** is defined as the attenuation with distance of an electromagnetic wave when it propagates in the environment. Usually, this law is approximated with the following equation as [7]

$$L = L_0 \left(\frac{d}{d_0}\right)^{\gamma}, \tag{1.3}$$

where L_0 is the path loss at the reference distance d_0 and γ is the path loss exponent. γ indicates how fast the path loss increases with distances. In general, this value can be deduced from measurements [8], [9].

In fact, the path loss is a parameter to predict only the local mean behavior of the channel [10]. Actually, the received power is not constant but varies for a fixed distance in a given environment. A random variation of the received signal around the mean path loss is called ***shadowing*** or ***large-scale fading***. Shadow fading is caused by big obstacles between the Tx and the Rx that attenuate the received power [7]. The effects of shadowing on the received power occur on a large scale - typically a few hundred wavelengths. Shadowing can be modeled as a log-normal random variable both in outdoor [11] and indoor [8] scenarios.

On a short-distance scale, the received power still varies significantly. These fluctuations happen on a scale that is comparable with wavelengths, so it is named

small-scale fading. It is caused by constructive and destructive interference of different propagation paths that contribute to the received power. Fading can be modeled as a random process and, commonly, it can be described by two probability distribution: i) Rayleigh distribution, when all paths have the same average energy, and ii) Rice distribution, when there is a dominant path, e.g. LOS [1]. There is an example in Fig. 1.3 to illustrate the received power versus the distance due to the effect of path loss, large-scale fading and small-scale fading.

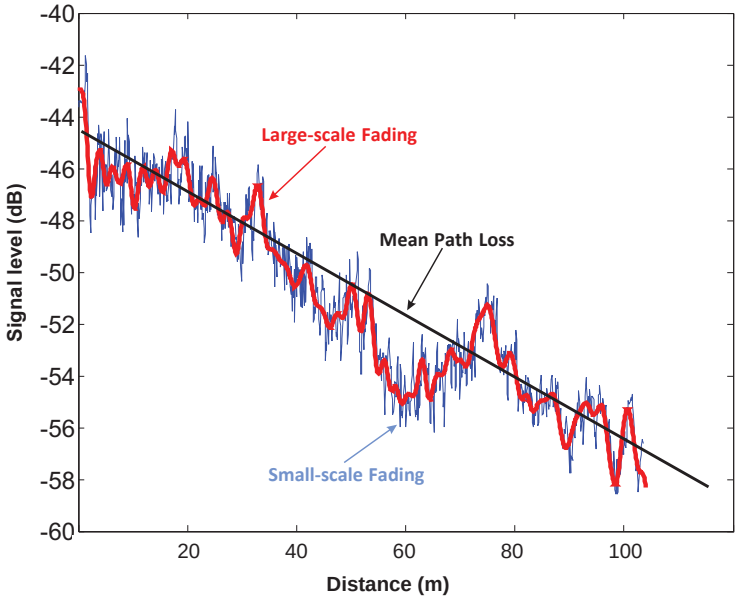

Figure 1.3: An example of path loss, large-scale fading and small-scale fading.

Each propagation path arriving at the Rx antenna travels along a different route with a different path length, which results in a different delay τ. The ***power delay profile (PDP)*** provides the information about how much power is received by the Rx within a delay region $[\tau, \tau_{\max}]$, where $\tau_{\max}$ is the maximum delay. A Rx with bandwidth B cannot distinguish between echoes arriving at τ and $\tau + \Delta\tau$, where $\Delta\tau = 1/B$ is the delay resolution. The PDP can be obtained from the complex ***channel impulse response (CIR)*** $h(t, \tau)$ as [1]

$$P_{\mathrm{h}}(\tau) = \int_{-\infty}^{\infty} |h(t, \tau)|^2 dt, \tag{1.4}$$

The ***root mean square (RMS) delay spread***, a measure of delay dispersion

of the channel, is defined as

$$\sigma_\tau = \sqrt{\frac{\int_0^\infty \tau^2 P_\mathrm{h}(\tau)d\tau}{\int_0^\infty P_\mathrm{h}(\tau)d\tau} - \tau_\mathrm{m}^2}, \tag{1.5}$$

where τ_m is the mean delay defined as

$$\tau_\mathrm{m} = \frac{\int_0^\infty \tau P_\mathrm{h}(\tau)d\tau}{\int_0^\infty P_\mathrm{h}(\tau)d\tau}. \tag{1.6}$$

If the Rx is moving, a shift of the received frequency occurs, called the Doppler shift. The Doppler shift is determined by the speed of the movement in the direction of wave propagation, $v\cos(\beta)$, where v is the speed of the moving Rx and β is the angle between the Rx moving direction and the direction of the propagation wave. The Doppler shift is given as [1]

$$\nu = -\frac{v}{\lambda}\cos(\beta) = -f_\mathrm{c}\frac{v}{c}\cos(\beta) = -\nu_\mathrm{max}\cos\beta, \tag{1.7}$$

where f_c is the carrier frequency, c is the speed of light, and $\nu_\mathrm{max} = -f_\mathrm{c}v/c$ is the maximum Doppler shift. The Doppler spectral density $P_\mathrm{B}(\nu)$ can be computed in complete analog way calculating the PDP as

$$P_\mathrm{B}(\nu) = \int_{-\infty}^{\infty} |B(\nu, f)|^2 df, \tag{1.8}$$

where $B(\nu, f)$ describes the spreading of the input signal in the Doppler and frequency domain. The Doppler-variant transfer function is defined as

$$B(\nu, f) = \int_{-\infty}^{\infty} H(t, f)exp(-j2\pi\nu t)dt, \tag{1.9}$$

where $H(t, f)$ is the ***channel transfer function (CTF)***

$$H(t, f) = \int_{-\infty}^{\infty} h(t, \tau)exp(-j2\pi f\tau)df. \tag{1.10}$$

This function describes the spreading of the input signal in the time and frequency domains. The ***RMS Doppler spread*** is defined as

$$\sigma_\nu = \sqrt{\frac{\int_{-\infty}^{\infty} \nu^2 P_\mathrm{B}(\nu)d\nu}{\int_{-\infty}^{\infty} P_\mathrm{B}(\nu)d\nu} - \nu_\mathrm{m}^2}, \tag{1.11}$$

where ν_m is the mean Doppler shift defined as

$$\nu_\mathrm{m} = \frac{\int_{-\infty}^{\infty} \nu P_\mathrm{B}(\nu)d\nu}{\int_{-\infty}^{\infty} P_\mathrm{B}(\nu)d\nu}. \tag{1.12}$$

The ***coherence bandwidth*** B_{coh} and ***coherence time*** t_{coh} are related to the RMS delay spread and RMS Doppler spread, respectively. B_{coh} is a measure of the range of frequencies over which the channel can be considered as flat [4]. The "uncertainty relationship" between B_{coh} and σ_τ is given as [12]

$$B_{\mathrm{coh}} \gtrsim \frac{1}{2\pi\sigma_\tau}. \tag{1.13}$$

If the bandwidth of the transmitted signal is $B \ll B_{\mathrm{coh}}$, fading across the signal bandwidth can be considered constant and we can refer to it as ***flat fading***. On the other hand, if $B \gg B_{\mathrm{coh}}$, different frequency components of the signal are affected by decorrelated fading resulting in ***frequency selective fading*** [7]. The definition of t_{coh} is analogous to B_{coh}, which also has a "uncertainty relationship" with the RMS Doppler spread. In Fig. 1.4, relationships between system function, correlation functions, and condensed parameters for ergodic CIR are summarized as described in [1].

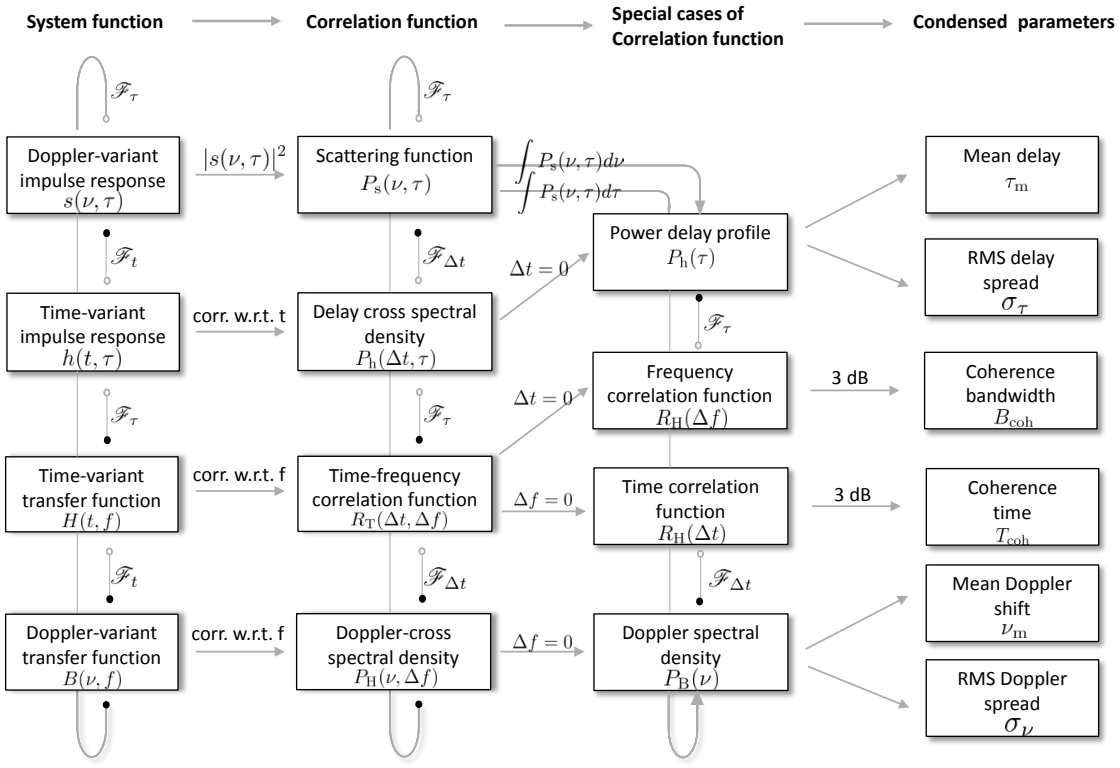

Figure 1.4: Relationships between system function, correlation functions, and condensed parameters for ergodic CIR as described in [1].

1.1.2 Channel Models

Channel models have two main applications [1]: i) we need simple channel models reflecting the important properties of propagation channels for designing and testing wireless systems, and ii) designers of wireless networks are interested in optimizing a given system in a specific geographical region. Three main categories of channel modeling approaches are used for both applications [1]: i) ***stored channel impulse responses*** directly obtained by channel measurements in a certain area, ii) ***stochastic channel models*** predicting the probability density function of the CIR or equivalent functions over a large area, and iii) ***deterministic channel models***, also known as site-specific models, using geometric and electromagnetic information from a database for a deterministic solution of Maxwell's equations to predict the CIR or equivalent functions in a certain location. In the following, I concentrate on reviewing stochastic and deterministic channel models.

Stochastic models describe the channel through the specific statistical properties of the fading process, without assuming an underlying geometry. For a ***narrowband channel***, statistical channel models are used in outdoor scenarios to predict channel characteristics, mainly path loss. The parameters involved in this case are the distance between Tx and Rx, building height, antenna heights, carrier frequency and type of measurements environment (e.g. urban, suburban, rural etc.). The most popular model in this category is the ***Okumura-Hata model*** [13]. Path loss (in dB) is written as

$$L_{\mathrm{dB}} = A + B\log(d) - C, \tag{1.14}$$

where A, B, and C are factors that depend on the frequency, antenna heights and type of propagation environment. Statistical channel models are also available for indoor scenarios, for example, the multi-wall ***COST231 model*** considers the number and type of walls and floors that a wave crosses [14]. The main advantage of these models is their simplicity together with their low computation complexity.

The most commonly used ***wideband channel model*** is the ***tap-delay line (TDL) model*** described as [1]

$$h(t,\tau) = a_0\delta(\tau-\tau_0) + \sum_{l=1}^{L} c_l(t)\delta(\tau-\tau_l), \tag{1.15}$$

where a_0 is the LOS component which does not vary along time, $\delta(\cdot)$ denotes Dirac function, τ_0 is the delay corresponding to the LOS path, l is the index of the fading tap, N is the total number of fading taps, $c_l(t)$ is a zero-mean complex Gaussian random process, whose autocorrelation function is determined by its associated Doppler spectra and τ_l is the delay of the $l-$th tap.

The second classic wideband channel model is the ***Saleh-Valenzuela model*** for indoor propagation [15], which assumes a priori existence of clusters. A cluster is defined as a collection of objects that are similar to each other in some agreed-upon sense [6]. In the radio channel sense, a cluster is defined as a group of multipath components that have similar delay of arrival and angular parameters. The CIR based on the Saleh-Valenzuela model is mathematically described as

$$h(\tau) = \sum_{l=0}^{L} \sum_{k=0}^{K} c_{k,l}(\tau)\delta(\tau - T_l - \tau_{k,l}), \tag{1.16}$$

where l is the index of the cluster, L is the total number of clusters, k is the path index of the $l-$th cluster, K is the total number of paths of the $l-$th cluster, $c_{k,l}$ is the gain of the $k-$th path of the $l-$th cluster, T_l is the delay of arrival of the $l-$th cluster and $\tau_{k,l}$ is the delay of arrival of the $k-$th path measured from the beginning of the $l-$th cluster. Within each cluster, the delay of arrival of each path inside the cluster and the relative delay of the clusters themselves are assumed to be Poisson distributed, while the power is assumed to have an exponential decay.

Another important family of stochastic models is the ***geometry-based stochastic channel model (GSCM)***. The basic idea of GSCMs is to place an ensemble of point scatterers according to a certain statistical distribution or at physically realistic positions, assign them different channel properties, determine their respective signal contribution and finally sum up the total contribution at the Rx [16]. Consequently, each propagation path intrinsically includes amplitude, delay and angular information [17]. The double-directional, time-variant, complex CIR as the superposition of L paths (contributions from scatterers) is given as [16]

$$h(t, \tau, \Omega_{\mathrm{R}}, \Omega_{\mathrm{T}}) = \sum_{l=1}^{L} c_i e^{jkd_l(t)} \delta(\tau - \tau_l)\delta(\Omega_{\mathrm{R}} - \Omega_{\mathrm{R},l})\delta(\Omega_{\mathrm{T}} - \Omega_{\mathrm{T},l}) g_{\mathrm{R}}(\Omega_{\mathrm{R}}) g_{\mathrm{T}}(\Omega_{\mathrm{T}}), \tag{1.17}$$

where Ω_{R} and Ω_{T} are the angular information at the Rx and the Tx side, l is the index of the propagation path, c_l, τ_l, $\Omega_{\mathrm{R},l}$, and $\Omega_{\mathrm{T},l}$ are the complex amplitude, excess delay, DoA and DoD of the $l-$th path, $g_{\mathrm{T}}(\Omega_{\mathrm{T}})$ and $g_{\mathrm{R}}(\Omega_{\mathrm{R}})$ are the Tx and the Rx antenna patterns, respectively, $e^{jkd_l(t)}$ is the corresponding distance-induced phase shift and $k = 2\pi/\lambda$ is the wave number. A subgroup of GSCMs is the cluster based model, e.g., ***WINNER II*** [18] and ***COST2100*** [19] etc. The aim of these models is to directly characterize clusters, rather than single propagation paths. Characterization of clusters includes the location of clusters in space and different related parameters that each cluster yields.

In stochastic channel models, either for the deviation of the model or its parameterizations, measurements need to be carried out for specific scenarios. It is obvious

that the critical step of such an approach is to establish a representative scenario for carrying out measurements. However, using derived models or extracted parameters in scenarios which are different as the original one might have some risks. This leads me to introduce ***deterministic channel models***, because they are based on the actual physical propagation of electromagnetic waves in a specific scenario. The physical propagation of electromagnetic waves actually contains the geometric and electromagnetic information in the specific-site under consideration. It is noteworthy that the accuracy is highly related to the description of the scenario. Moreover, deterministic channel models suffer from a main problem - high computational complexity.

The most accurate methods, based on a given scenario database, are the ones that are directly derived from Maxwell's equations, employing either integral or differential equation formulations. Integral equations are most often variations of the method of moments (MoM), while the differential equation formulations include the finite difference time domain (FDTD) method [1]. Due to their complexity, their application is impractical for large scenarios. The most commonly used family of deterministic models is the ray-based approach, that approximates Maxwell's equation following geometrical optics (GO) high-frequency criteria [10]. A ray presents the propagation of an electromagnetic wave here.

There are two types of ray-based deterministic propagation models: i) ***ray launching*** and ii) ***ray tracing (RT)***. The difference lies in the algorithm used to find the rays between the source and the observation point [20]. For ray launching, the Tx antenna launches rays in all possible directions depending on a pre-defined angular resolution. In a considered point-to-point communication, this approach has a drawback. It is necessary to define an area of a certain extension, normally a sphere around the Rx, to collect rays. If the defined area is too large it may include rays that are not actually seen by the Rx, while if this defined area is too small some relevant rays might be omitted [21]. Ray launching might be a suitable tool for wireless coverage prediction, where it provides channel characteristics in the whole environment that has been subdivided into multiple tiles. RT determines all rays that go from one Tx location to one Rx location. It relies on GO and the uniform theory of diffraction (UTD) to evaluate all propagation paths as they interact with the environment. Current RT tool not only considers LOS, reflection and diffraction components, but also penetration and diffuse scattering components. The detailed principles are depicted in Chapter 2.

1.2 State of Art in Ray Tracing

In literature, we can find several contributions about RT both for outdoor [22–31] and indoor scenarios [32–42]. For describing the ***basic element*** used in the RT tool, e.g. buildings in outdoor scenarios or walls and furniture in indoor scenarios and so on, there exist different methods. Facets are used in [33], [37], while polygons are used in [27], [43]. In addition, a vector oriented pixel grid/database is applied in [26], [35], [28], [41] and the Google Maps database is applied in [31]. The RT tool used in this thesis describes each basic element as ***a rectangular parallelepiped*** [30].

There are different methods to build the ***geometrical scenario*** in RT. Early RT tools are two-dimensional (2D) [22], [34], which assume that the propagation takes place in a 2D plane, either the horizontal or the azimuth plane. If both the Tx and the Rx antennas are at the same height and only a rough analysis of channel characteristics is needed, 2D RT provides a sufficient approximation [10]. Hybrid techniques are also developed, where the three-dimensional (3D) rays are produced by combining the results of a 2D RT tool, one in the horizontal and the other one in the vertical plane [23], [32]. The most common implementation is ***full 3D RT***, which is a good candidate to estimate site-specific space-time channel characteristics. Based on 3D RT, the whole environment is described by a 3D database, where interactions occur in 3D space and 3D antenna radiation patterns are employed.

Regarding the type of ***propagation mechanisms***, in addition to ***LOS***, ***reflection*** and ***diffraction*** are usually considered based on GO and UTD algorithms. ***Penetration*** or ***wall transmission*** is also implemented in some RT tools in indoor scenarios [44–47]. In an advanced RT tool, a ***diffuse scattering*** model is included as well. Diffuse scattering proves to be an important factor in determining time and angle dispersion of radio signals in indoor environments [37], [48]. It is shown that diffuse scattering also plays a key role in urban propagation, with an impact on both narrowband and wideband parameters in most cases [27]. In [40], it is presented that the diffuse scattering accounts for 10% the total CTF energy in mmW indoor scenario. Moreover, the importance of diffuse scattering in THz communication channels is underlined in [49]. The most popular model of diffuse scattering is presented in [2], which is based on the effective roughness (ER) approach. The model has been implemented in outdoor scenarios [27], [50], [51] and indoor scenarios [52], [37], [53], [42].

As mentioned, the main drawback of deterministic channel models is their large ***computational complexity***. Until now, some techniques have been implemented to accelerate the RT tool. In [23], [32], hybrid techniques enhance the concept of

"illumination zones", which is the area that an image can give a valid reflection path. These techniques make the higher-order reflection images narrow and prevent the number of images increasing dramatically. In [33], an angular Z-buffer (AZB) algorithm is proposed to speed up the RT tool, which is an algorithm based on the light buffer technique used in computer-aided graphic design. In [28], in order to save the computation time, the described 3D urban RT model divides the coverage area into a near-reception region, where all ray contributions are computed, and a far-reception region, where only the dominant contributions that propagate over rooftops are predicted. After integrating diffuse scattering into RT, the computation time increases significantly. In [49], there are 400 scattering tiles with the same size placed around each specular reflection interaction point. Currently, an approach, which efficiently utilizes the potential and capabilities in the graphical processing unitss (GPUs), is proposed to provide the high performance of computations for RT [54–56].

The ***validation*** of RT in a specific scenario is essential. I give a brief overview over which kind of channel properties can be characterized depending on different information. For instance, for wideband channel characteristics, the RMS delay spread is a very common metric to be estimated by RT [27], [26], [32], [35]. The PDP can also be evaluated to compare simulations and measurements [23], [24], [32]. For determining the characteristics of a mobile channel, the Doppler shift and the RMS Doppler spread can be predicted and validated [57], [58]. RT simulations can also be used for evaluating the statistical performances of a communication channel. The capacity of a MIMO wireless system is estimated based on RT [34]. Moreover, the bit error rate (BER) of a MIMO multiband orthogonal frequency division multiplexing (OFDM) system is computed from measurements and simulations in [59].

1.3 Outline and Contributions

The goal of my thesis is to reduce the computational complexity of RT with no loss of accuracy. There are three scenarios included: wideband indoor, ultra-wideband (UWB) indoor and tunnel scenarios. This thesis consists of four chapters, as well as the introduction and the conclusions. The content of this document is to a great extent also included in the following peer-reviewed publications:

[60] M. Gan, F. Mani, F. Kaltenberger, C. Oestges, and T. Zemen, "A ray tracing algorithm using the discrete prolate spheroidal subspace," in *IEEE International Conference on Communications Workshops (ICC)*, June 2013, pp. 5710-5714.

[61] P. Meissner, M. Gan, F. Mani, E. Leitinger, M. Frohle, C. Oestges, T. Zemen, and K. Witrisal, "On the use of ray tracing for performance prediction of UWB indoor localization systems," in *IEEE International Conference on Communications Workshops (ICC)*, June 2013, pp. 68-73.

[62] M. Gan, P. Meissner, F. Mani, E. Leitinger, M. Frohle, C. Oestges, K. Witrisal, and T. Zemen, "Low-complexity sub-band divided ray tracing for UWB indoor channels," in *IEEE Wireless Communications and Networking Conference (WCNC)*, April 2014, pp. 305-310.

[63] M. Gan, P. Meissner, F. Mani, E. Leitinger, M. Frohle, C. Oestges, K. Witrisal, and T. Zemen, "Calibration of indoor UWB sub-band divided ray tracing using multiobjective simulated annealing," in *IEEE International Conference on Communications (ICC)*, June 2014, pp. 4844-4849.

[64] M. Gan, X. Li, F. Tufvesson, and T. Zemen, "An effective subdivision algorithm for diffuse scattering of ray tracing," in *XXXIth URSI General Assembly and Scientific Symposium (URSI GASS)*, August 2014, pp. 1-4.

[65] M. Gan, Z. Xu, V. Shivaldova, A. Paier, F. Tufvesson, and T. Zemen, "A ray tracing algorithm for intelligent transport systems in tunnels," in *IEEE 6th International Symposium on Wireless Vehicular Communications (WiVeC)*, September 2014, pp. 1-5.

[66] M. Gan, Z. Xu, M. Hofer, G. Steinböck, and T. Zemen, "A sub-band divided ray tracing algorithm using the DPS subspace in UWB indoor scenarios," in *IEEE 81st Vehicular Technology Conference (VTC-Spring)*, May 2015, pp. 1-5.

[67] G. Steinböck, M. Gan, P. Meissner, E. Leitinger, K. Witrisal, T. Zemen, and T. Pedersen, "Hybrid model for reverberant indoor radio channels using rays and graphs," in *IEEE Transactions on Antennas and Propagations*, 2015, submitted.

The chapters are organized as follows:

Chapter 2: Ray Tracing Channel Model
In this chapter, GO and UTD approaches evaluating all propagation paths as they interact with the environment are outlined. The basic principle of conventional RT is introduced and the involved propagation mechanisms are presented. This chapter

gives the basic knowledge of the implementation of propagation mechanisms which are used to simulate the interactions of rays with the environment. RT includes three major wave propagation mechanisms: (i) LOS, (ii) specular mechanism as well as (iii) diffuse scattering. The specular mechanism refers to reflection, penetration and diffraction. The geometrical relationships between the incidence and the reflected/penetrated/diffracted rays are based on optical principle. Complex dyadic coefficients for reflection and penetration are obtained using Fresnel formulas [68], while the diffraction coefficient is calculated by the UTD [69]. Furthermore, the most popular model of diffuse scattering [2] is presented.

Chapter 3: Ray Tracing for Wideband Indoor Scenarios
For the sake of accelerating the execution of the RT tool, the Matlab code of RT is optimized through converting time-consuming algorithms to Matlab executable (MEX) functions by using MATLAB Coder. The speeding up effort focuses on the reflection and diffuse scattering calculations, because the number of reflection and diffuse scattering propagation paths comprise a large proportion among all propagation paths. Compared with conventional RT, the simulation time of the revised Matlab code is significantly reduced.

Besides speeding up the code, an efficient approach to generate diffuse scattering tiles based on concentric circles is developed and evaluated [64]. The proper tile size is defined according to the system bandwidth. The method significantly reduces the computational complexity of RT with no loss in accuracy. The method is verified by evaluating the PDP, RMS delay spread and RMS angular spread.

Moreover, for a wideband indoor scenario, I am also interested in simulating radio propagation conditions for a mobile terminal, communicating in a frame based communication system indoors with several fixed nodes. The correlated temporal and spatial evolution of the CIR is of utmost concern. A RT algorithm based on two-dimensional discrete prolate spheroidal (DPS) sequences is proposed [60]. With this method the computational complexity can be reduced by more than one order of magnitude for indoor scenarios. The accuracy of this low-complexity DPS subspace based RT algorithm is verified by numeric simulations.

Chapter 4: Ray Tracing for UWB Indoor Scenarios:
For an UWB system, channel characteristics may vary significantly over the entire bandwidth. To cope with this, sub-band divided ray tracing (SDRT) has been proposed. However, the computational complexity is directly proportional to the

number of sub-bands. In order to significantly reduce the computational complexity of SDRT, I propose a mathematical method by making SDRT almost independent of the number of sub-bands, which is named low-complexity SDRT [62]. The accuracy of the low-complexity SDRT algorithm is verified through a measurement campaign.

It is known that the accuracy of SDRT is strictly limited by the available description of the environment [61]. Based on the low-complexity SDRT implementation, I also propose a calibration method for indoor UWB low-complexity SDRT [63]. The method estimates the optimal material parameters, including the dielectric parameters and the scattering parameters, using channel measurements and multiobjective simulated annealing (MOSA). This calibration can improve the accuracy of SDRT in terms of the PDP and RMS delay spread for all test locations including those not considered by the calibration.

Furthermore, although I have proposed the low-complexity SDRT algorithm for one terminal position, the computational complexity is still extremely high when involving multiple mobile terminal positions. To cope with this, I propose an algorithm to reduce the computational complexity of SDRT for multiple mobile terminal positions [66]. The algorithm uses a projection of all propagation paths on a subspace spanned by two-dimensional DPS sequences at each sub-band. It is important to note that, since the geometrical information of propagation paths is the same in all sub-bands, the subspace dimension and basis coefficients in frequency dimension do not need to be recalculated at different sub-bands. I justify the simplifications of the proposed method by numerical simulations. The effect of antenna characteristics on the proposed algorithm is evaluated as well.

Chapter 5: Ray Tracing for Tunnel Scenarios:
In this chapter, I apply RT for tunnel scenarios, because this scenario has not been studied adequately until now. Radio wave propagation mechanisms inside a tunnel are different from typical outdoor and indoor situations. Since the tunnel represents a significant type of vehicular environments, understanding the channel characteristics for the in-tunnel scenario is crucial for intelligent transport system (ITS) design. In this work, real-world in-tunnel vehicle-to-vehicle (V2V) radio channel measurements are evaluated according to the local scattering function (LSF). The LSF is a useful quantity for characterizing non-stationary time-variant channels, which is a short-term representation of the power spectrum of the observed fading process. I suggest to combine an approximate algorithm for higher-order reflection components with conventional RT as the first step to reduce the computational complexity, where the RT tool includes the moving objects in the scenario [65].

In [67], we have proposed a hybrid model for reverberant indoor radio channels using rays and graphs. As the second step, we propose a non-stationary V2V channel model combining RT with propagation graphs in tunnels. The graph theory is applied to predict reverberation effects of electromagnetic waves. A so-called directed propagation graph can be set up according to the propagation scenario. It is used to model the higher-order reflection tail and the contribution from independent scatterers. To obtain the parameter settings for the propagation graph, we use RT and the approximated higher-order reflection algorithm. The proposed model allows me obtaining more accurate PDP, RMS delay and Doppler spreads. The numerical simulations show good agreement with measurements.

2 Ray Tracing Channel Model

GO is an approximation that can be used to describe the propagation mechanisms of high frequency electromagnetic waves. Based on GO, propagation is described in terms of rays, where a ray is just a model for the path taken by the electromagnetic radiation emitted by a source [10]. Rays are always perpendicular to the local wavefront, so that they are collinear with the wave vector. The main properties of a ray is i) that of being a straight line and ii) that of being mutual independent to other rays. Besides the LOS, there are four basic mechanisms governing the propagation of electromagnetic waves in a mobile communication systems, which are reflection, penetration, diffraction and diffuse scattering. The implementation of the propagation mechanisms is used to simulate the interactions of rays with the environment. The 3D RT tool used in this thesis is written in MATLAB based on a pre-existent RT tool implemented in the C programming language by Université catholique de Louvain, Belgium [10]. In order to distinguish with the further improved work, the RT tool built up at the starting point is named conventional RT. The RT geometry is described depending on a cartesian coordinate system and the simulation environment is generated using perpendicular parallelepiped. Any object is homogeneous and represents a furniture or a slab of the structure in the indoor scenario. The input parameters of 3D RT are

- frequency,
- positions of Tx and Rx antenna,
- 3D radiation patterns of Tx and Rx antenna,
- 3D coordinates of every object in the propagation environment,
- permittivity and conductivity of the object materials, and
- relevant parameters related to different propagation mechanisms, such as reflection order, scattering coefficient, and an indicator for the perfect electric conductor (PEC).

Moreover, the output parameters of each propagation path are

- 3D coordinates of all the relevant interacting points along the propagation path,
- total path length, which can be used to calculate the delay,
- complex electric field based on the propagation mechanism,
- index indicating the type of the propagation path,
- corresponding propagation coefficients.

In this chapter, the basic concepts and the implementation of relevant propagation mechanisms are presented. The mechanisms are introduced in the order of the development of the RT tool. The fundamental problem consists in the calculation of the electric field received at the Rx side in amplitude, phase and polarization, where the electric field is a complex vector. In the following, I take the single order case as an example for each propagation mechanism to present how to calculate the complex electric field. For the multiple order case, we can use the same way as the single order case to calculate the complex electric field.

2.1 Line of Sight

For wireless communications, free space propagation is the simplest case in which the signal propagates directly from the Tx antenna to the Rx antenna, which has been explained in Section 1.1.2. The received complex electric field of the LOS path E_{LOS} at an observation point $\mathbf{P}$ at center frequency f_{c} can be expressed as

$$E_{\mathrm{LOS},\mathbf{P}}(f_{\mathrm{c}}) = A(f_{\mathrm{c}}, s) \cdot [\bar{g}^{\mathrm{R}}_{\mathrm{LOS}}(f_{\mathrm{c}})]^* \cdot [\bar{g}^{\mathrm{E}}_{\mathrm{LOS}}(f_{\mathrm{c}})] \cdot \bar{E}_0 \cdot e^{\frac{-j2\pi f_{\mathrm{c}} s_{\mathrm{LOS}}}{c}}, \tag{2.1}$$

where $A(f_{\mathrm{c}}, s) = c/(4\pi f_{\mathrm{c}} s)$ is the free space path loss and s is the total path length between Tx and Rx. Here $s = s_{\mathrm{LOS}}$, where s_{LOS} is the shortest distance between the Tx and the Rx. $\bar{g}^{\mathrm{E}}_{\{\cdot\}}(f_{\mathrm{c}}) = \bar{g}^{\mathrm{E}}_{\{\cdot\}}(f_{\mathrm{c}}, \theta_{\mathrm{E}}, \phi_{\mathrm{E}})$ and $\bar{g}^{\mathrm{R}}_{\{\cdot\}}(f_{\mathrm{c}}) = \bar{g}^{\mathrm{R}}_{\{\cdot\}}(f_{\mathrm{c}}, \theta_{\mathrm{R}}, \phi_{\mathrm{R}})$ are complex vectors accounting for the Tx/Rx antenna polarization and amplitude gains in the direction of the propagation wave, $\theta_{\{\cdot\}}$ and $\phi_{\{\cdot\}}$ indicate the azimuth and elevation directions of the transmitted/received wave, $[\cdot]^*$ designates the complex conjugate, and $\bar{E}_0$ is the emitted field, which is a vector.

2.2 Reflection Mechanism

When a radio wave propagating in one medium impinges upon another medium having different electrical properties, the wave is partially reflected and partially

transmitted. If the plane wave is incident on a homogenous dielectric, part of the energy is reflected back to the first medium and part of the energy is transmitted into the second medium. If the second medium is a PEC, all incidence energy is reflected back into the first medium without loss of energy [4]. In this section, the mathematical calculation of the reflected field and the calculation for finding the reflected path in RT are introduced.

2.2.1 Reflection

Reflection, or specular reflection occurs when an electromagnetic wave impinges upon an object which has very large dimensions compared to the wavelength of the propagating wave [4]. Moreover, if the standard deviation of the surface roughness is significantly smaller than the wavelength, incidence waves can still be seen as specularly reflected [70]. The surface acts as a flat mirror, on which the impinging wave is reflected in a single direction. This is defined by the law of reflection. It states that the incidence ray, the reflected ray, and the normal to the surface where the reflection point lies are in the same plane and the angle of reflection ϑ_{ref} is equal to the angle of incidence ϑ_{inc}. Both angles are measured with respect to the normal to the surface. The illustration of the reflection mechanism and the plane of the incidence and reflected wave are depicted in Fig. 2.1.

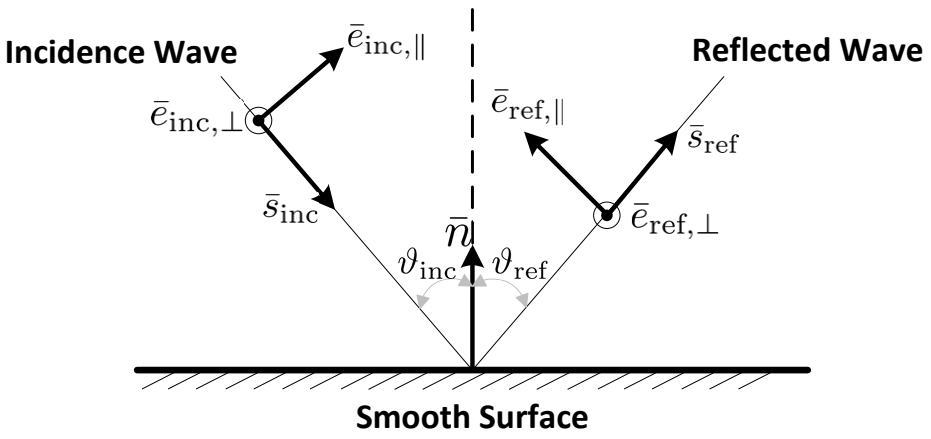

Figure 2.1: Illustration of the reflection mechanism and the plane of the incidence and reflected wave.

In Fig. 2.1, there is a smooth surface with unit normal vector $\bar{n}$. The incidence wave is defined by a unit vector $\bar{s}_{\text{inc}}$ in its direction of propagation, while a unit

vector $\bar{s}_{\text{ref}}$ indicates the direction of propagation of the reflected wave. The angle of incidence and the angle of reflection are given by

$$\vartheta_{\text{inc}} = -\arccos(\bar{n} \cdot \bar{s}_{\text{inc}}) \tag{2.2}$$

and

$$\vartheta_{\text{ref}} = \arccos(\bar{n} \cdot \bar{s}_{\text{ref}}), \tag{2.3}$$

respectively. Reflection can be described by adopting a ray-fixed coordinate system, in which the electric field can be decomposed into two components: i) a parallel component and ii) a perpendicular component to the plane of the incidence and reflected wave [10]. The parallel unit vectors, $\bar{e}_{\text{inc},\parallel}$ and $\bar{e}_{\text{ref},\parallel}$ for the incidence and reflected field respectively, can be evaluated as

$$\bar{e}_{\text{inc},\parallel} = \frac{\bar{s}_{\text{inc}} \times (\bar{n} \times \bar{s}_{\text{inc}})}{|\bar{s}_{\text{inc}} \times (\bar{n} \times \bar{s}_{\text{inc}})|} \tag{2.4}$$

and

$$\bar{e}_{\text{ref},\parallel} = \frac{\bar{s}_{\text{ref}} \times (\bar{n} \times \bar{s}_{\text{ref}})}{|\bar{s}_{\text{ref}} \times (\bar{n} \times \bar{s}_{\text{ref}})|}, \tag{2.5}$$

where $|\cdot|$ indicates the vector norm. Consequently, the perpendicular unit vectors $\bar{e}_{\text{inc},\perp}$ and $\bar{e}_{\text{ref},\perp}$ are evaluated as

$$\bar{e}_{\text{inc},\perp} = \bar{s}_{\text{inc}} \times \bar{e}_{\text{inc},\parallel} \tag{2.6}$$

and

$$\bar{e}_{\text{ref},\perp} = \bar{s}_{\text{ref}} \times \bar{e}_{\text{ref},\parallel}. \tag{2.7}$$

According to the law of reflection, the reflected ray lies in the same plane of the incidence ray, which results in $\bar{e}_{\text{inc},\perp} = \bar{e}_{\text{ref},\perp} \triangleq \bar{e}_{\perp}$.

The first-order complex electric field of the reflected path E_{ref} at an observation point $\mathbf{P}$ on a perfect dielectric at center frequency f_{c} in RT can be expressed as

$$E_{\text{ref},\mathbf{P}}(f_{\text{c}}) = A(f_{\text{c}}, s) \cdot [\bar{g}^{\text{R}}_{\text{ref}}(f_{\text{c}})]^* \cdot \overline{\overline{\mathbf{R}}}(f_{\text{c}}) \cdot \bar{E}_{\text{inc},\mathbf{Q}_{\text{ref}}} \cdot s_{\text{ref}} \cdot e^{\frac{-j2\pi f_{\text{c}} s'_{\text{ref}}}{c}}, \tag{2.8}$$

where

$$\bar{E}_{\text{inc},\mathbf{Q}_{\text{ref}}} = [\bar{g}^{\text{E}}_{\text{ref}}(f_{\text{c}})] \cdot \bar{E}_0 \frac{e^{\frac{-j2\pi f_{\text{c}} s_{\text{ref}}}{c}}}{s_{\text{ref}}}, \tag{2.9}$$

$s = s_{\text{ref}} + s'_{\text{ref}}$ in $A(f_{\text{c}}, s)$ is the total path length, s_{ref} is the path length from the Tx to the reflection interaction point $\mathbf{Q}_{\text{ref}}$, s'_{ref} is the path length from the reflection interaction point $\mathbf{Q}_{\text{ref}}$ to the Rx, and $\overline{\overline{\mathbf{R}}}$ is the Fresnel dyadic reflection coefficient. $\overline{\overline{\mathbf{R}}}$ is a 3×3 matrix defined by the following expressions [70]

$$\overline{\overline{\mathbf{R}}} = R_{\parallel} \bar{e}_{\text{inc},\parallel} \bar{e}_{\text{ref},\parallel} + R_{\perp} \bar{e}_{\text{inc},\perp} \bar{e}_{\text{ref},\perp} \tag{2.10}$$

where $R_{\parallel}$ and $R_{\perp}$ are parallel and perpendicular polarization coefficients, which are denoted separately as

$$R_{\parallel} = \frac{\varepsilon_{r,\text{eff}} \cos\vartheta_{\text{inc}} - \sqrt{\varepsilon_{r,\text{eff}} - \sin^2\vartheta_{\text{inc}}}}{\varepsilon_{r,\text{eff}} \cos\vartheta_{\text{inc}} + \sqrt{\varepsilon_{r,\text{eff}} - \sin^2\vartheta_{\text{inc}}}}, \tag{2.11}$$

and

$$R_{\perp} = \frac{\cos\vartheta_{\text{inc}} - \sqrt{\varepsilon_{r,\text{eff}} - \sin^2\vartheta_{\text{inc}}}}{\cos\vartheta_{\text{inc}} + \sqrt{\varepsilon_{r,\text{eff}} - \sin^2\vartheta_{\text{inc}}}}, \tag{2.12}$$

where $\varepsilon_{r,\text{eff}}$ is the complex effective relative permittivity of a certain material, which is defined as

$$\varepsilon_{r,\text{eff}} = \varepsilon_r - j\frac{\sigma}{2\pi f_c \varepsilon_0}, \tag{2.13}$$

where $\varepsilon_0 = 8.854 \cdot 10^{-12}$ Farad/m is the vacuum dielectric constant, and ε_r and σ are the dielectric permittivity and conductivity for a specific material, respectively. Although (2.13) is strictly valid for a single frequency, it can actually be used for a system with bandwidth B.

If the reflecting object is a PEC, all incidence energy is reflected, since electromagnetic energy cannot pass through the PEC. Thus, the magnitude of the reflected wave must be equal to the one of the incidence wave [4].

2.2.2 Reflection Path Calculation

Actually, GO is implemented in a RT tool based on the method of images. When visible light is reflected on a mirror, it seems that the ray coming from the source appears to originate from a point behind the mirror. This point is called the image of the source. The principle is introduced in RT to find the relevant reflection interaction point. By using a line connecting the observation point and the image point, the intersection point between the line and the surface can be found. An example of the image principle is demonstrated in Fig. 2.2. When the coordinate of the Tx is known, the 3D image points I_{S_1}, I_{S_2}, and I_{S_3} corresponding to surfaces S_1, S_2, and S_3 can be calculated based on the image principle. The image points are further treated as the new sources for the next interaction, e.g., the image point $I_{\text{S}_2,\text{S}_3}$. The reflection paths are further obtained based on the image points. In Fig. 2.2, two first-order reflection paths in black solid lines and one second-order reflection path in blue solid line are shown. The implementation about how to build the image tree and how to further find reflected paths will be introduced in Section 3.1.2.

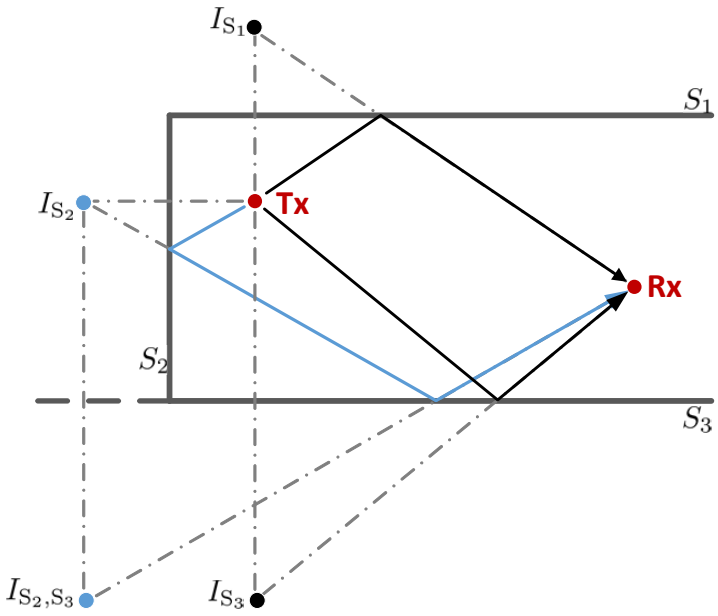

Figure 2.2: An example of the image principle.

2.3 Diffraction

Consider an impenetrable obstacle, GO in this situation only allows direct and reflected rays [10]. As a result, there is a region marked by the obstacle, that cannot be reached by any rays, and there is another region reachable with direct rays but not with reflected rays. The boundaries of these regions are defined as incident shadow boundary (ISB) and reflection shadow boundary (RSB), respectively. In Fig. 2.3, two shadow boundaries are depicted. In total, three regions can be distinguished [70]:

- region I, where both the direct and the reflected field exist,
- region II, where only the direct field exists,
- region III, where no field exits.

This results in the conclusion that the GO field is strongly discontinuous at the shadow boundaries. Moreover, the GO field is equal to zero inside the region III. A basic electromagnetic rule declares that an electromagnetic field must be smooth and continuous everywhere. In this sense, ordinary GO needs to be extended to describe the propagation in the presence of an obstacle at the shadow boundaries and in the shadow region. In addition, due to Huygens' principle, secondary waves

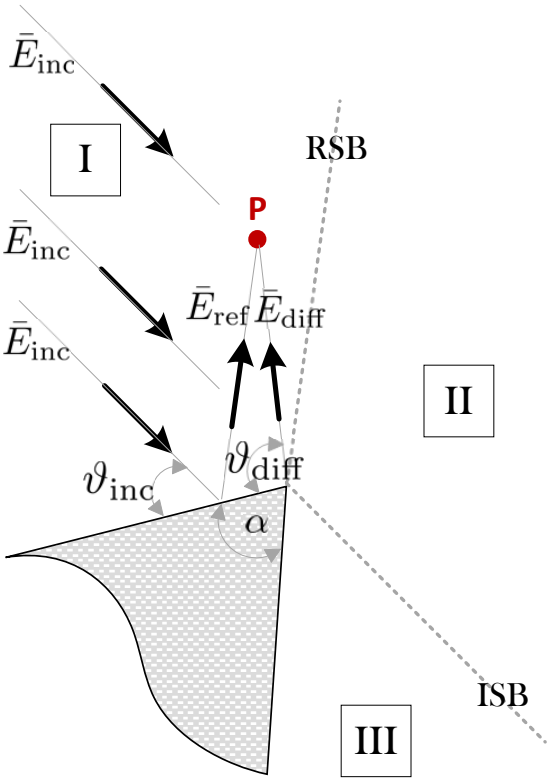

Figure 2.3: Shadow boundaries and geometry for wedge diffraction.

are formed even behind the obstructing wedge, which leads to the existence of a diffracted field in all regions. Thus, a geometrical theory of diffraction (GTD) was proposed when knowing that the diffraction is responsible for the field in the shadow region in [71]. The GTD states that the diffraction can occur on edges, vertices and curved surfaces. Following Fermat's principle, the laws of diffraction are derived.

In a RT tool, the law of edge diffraction is the basis for calculating the received complex electric field of the diffracted path. The law of edge diffraction has been formulated as in [71] - a diffracted ray and the corresponding incidence ray make equal angles with the edge at the diffraction point and they lie on opposite sides of the plane normal to the edge at the diffraction point. Although the GTD is able to predict the non-zero field in the region III, it is singular in this region [10]. A solution, named as UTD, was firstly presented to compensate for the discontinuity at the shadow boundaries [72]. A transition function was introduced to keep the field continuous at the boundaries by multiplying it with the GTD coefficients.

The UTD solution is explained as follows: firstly, the faces of the wedge are denoted as 0−face and n−face. Actually, it is arbitrary to call which face is the 0−face. However, it is conventional to consider the angles ϑ_{inc} and ϑ_{diff} between the incidence/diffrated ray and one of the faces measured from the 0−face. Thus, the 0−face is located at $\vartheta = 0$. Assume that the interior angle of the wedge is α, it can be obtained that

$$n\pi = 2\pi - \alpha, \tag{2.14}$$

where $n\pi$ represents the exterior angle of the wedge. Meanwhile, the n−face is located at an angle $\vartheta = n\pi$. In addition, it is assumed that the incidence ray is impinging on an edge with angle $\beta_{0,\text{inc}}$. Based on the law of edge diffraction, various diffracted rays form a cone with half-angle $\beta_{0,\text{diff}}$ as shown in Fig. 2.4. Moreover, it

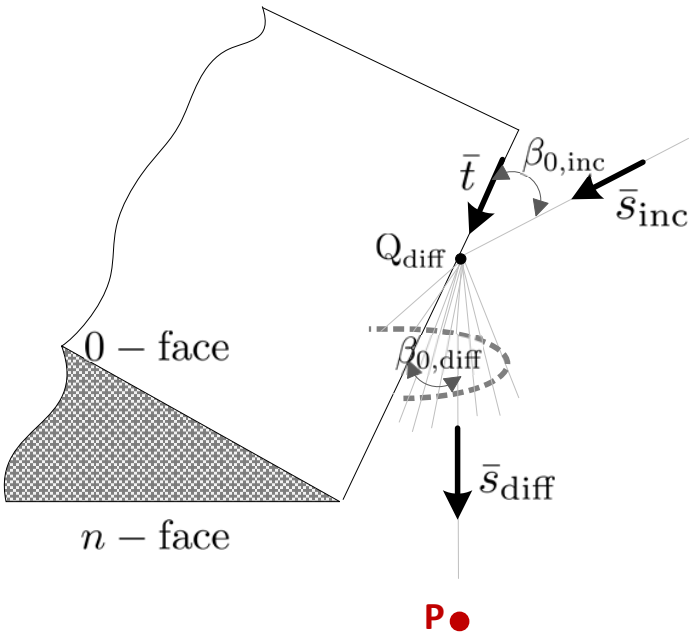

Figure 2.4: Geometry of the diffraction point and cone of diffracted rays.

can be obtained that $\beta_{0,\text{diff}} = \beta_{0,\text{inc}} \triangleq \beta_0$. The location of the diffraction point $\mathbf{Q}_{\text{diff}}$ can be subsequently determined by

$$\sin\beta_0 = |\bar{s}_{\text{inc}} \times \bar{t}| = |\bar{s}_{\text{diff}} \times \bar{t}|, \tag{2.15}$$

where $\bar{s}_{\text{inc}}$ and $\bar{s}_{\text{diff}}$ are the unit vectors in the directions of the incidence and the diffracted wave, and $\bar{t}$ is a vector tangential to the edge, respectively. The $\bar{s}_{\text{inc}}$, $\bar{t}$ and

the location of the Rx are known, so that the unknown $\bar{s}_{\text{diff}}$ can be calculated. The diffraction point $\mathbf{Q}_{\text{diff}}$ can be further obtained.

The first-order complex electric field of the edge-diffracted path E_{diff} at an observation point $\mathbf{P}$ at center frequency f_{c} in RT can be expressed as

$$E_{\text{diff},\mathbf{P}}(f_{\text{c}}) = A(f_{\text{c}}, s)\cdot[\bar{g}^{\text{R}}_{\text{diff}}(f_{\text{c}})]^{*}\cdot\overline{\overline{\mathbf{D}}}(f_{\text{c}})\cdot\bar{E}_{\text{inc},\mathbf{Q}_{\text{diff}}}\sqrt{\frac{s_{\text{diff}}(s_{\text{diff}}+s'_{\text{diff}})}{s'_{\text{diff}}}}e^{\frac{-j2\pi f_{\text{c}},i s'_{\text{diff}}}{c}}, \quad (2.16)$$

where

$$\bar{E}_{\text{inc},\mathbf{Q}_{\text{diff}}} = [\bar{g}^{\text{E}}_{\text{diff}}(f_{\text{c}})]\cdot\bar{E}_0\frac{e^{\frac{-j2\pi f_{\text{c}} s_{\text{diff}}}{c}}}{s_{\text{diff}}}, \quad (2.17)$$

$s = s_{\text{diff}} + s'_{\text{diff}}$ in $A(f_{\text{c}}, s)$ is the total path length, s_{diff} is the path length from the Tx to the diffraction interaction point $\mathbf{Q}_{\text{diff}}$, s'_{diff} is the path length from the diffraction interaction point $\mathbf{Q}_{\text{diff}}$ to the Rx, and $\overline{\overline{\mathbf{D}}}$ is the UTD dyadic diffraction coefficient. In order to simplify the equation, f_{c} is ignored in the following equations. $\overline{\overline{\mathbf{D}}}$ is a 3×3 matrix given by

$$\overline{\overline{\mathbf{D}}} = -D_{\perp}\bar{\beta}_{0,\text{inc}}\bar{\beta}_{0,\text{diff}} - D_{\parallel}\bar{\vartheta}_{\text{inc}}\bar{\vartheta}_{\text{diff}}, \quad (2.18)$$

where the edge-fixed coordinate systems $(\bar{s}_{\text{inc}}, \bar{\beta}_{0,\text{inc}}, \bar{\vartheta}_{\text{inc}})$ and $(\bar{s}_{\text{diff}}, \bar{\beta}_{0,\text{diff}}, \bar{\vartheta}_{\text{diff}})$ are defined as

$$\bar{\phi}_{\text{inc}} = \frac{\bar{s}_{\text{inc}}\times\bar{t}}{|\bar{s}_{\text{inc}}\times\bar{t}|}, \quad (2.19)$$

$$\bar{\phi}_{\text{diff}} = \frac{\bar{s}_{\text{diff}}\times\bar{t}}{|\bar{s}_{\text{diff}}\times\bar{t}|}, \quad (2.20)$$

$$\bar{\beta}_{0,\text{inc}} = \bar{\vartheta}_{\text{inc}}\times\bar{s}_{\text{inc}}, \quad (2.21)$$

$$\bar{\beta}_{0,\text{diff}} = \bar{\vartheta}_{\text{diff}}\times\bar{s}_{\text{diff}}, \quad (2.22)$$

and

$$\begin{aligned} D^{\perp}_{\parallel} &= \frac{-e^{-j\pi/4}}{2n\sqrt{2\pi k}\sin\beta_0}[D_1 + D_2 + R_{0\parallel}^{\perp}D_3 + R_{n\parallel}^{\perp}D_4] \\ &= \frac{-e^{-j\pi/4}}{4n\pi\sqrt{f_{\text{c}}/c}\sin\beta_0}[D_1 + D_2 + R_{0\parallel}^{\perp}D_3 + R_{n\parallel}^{\perp}D_4], \end{aligned} \quad (2.23)$$

where $n = 2 - \alpha/\pi$ can be obtained from (2.14), and $R_{0\parallel}^{\perp}$ and $R_{n\parallel}^{\perp}$ are the reflection coefficients for either perpendicular or parallel polarization for the $0-$face and $n-$face [69], and

$$D_1 = \cot\left(\frac{\pi + (\vartheta_{\text{diff}} - \vartheta_{\text{inc}})}{2n}\right)\cdot F\left(\frac{2\pi f_{\text{c}}}{c}La^{+}(\vartheta_{\text{diff}} - \vartheta_{\text{inc}})\right), \quad (2.24)$$

$$D_2 = \cot\left(\frac{\pi - (\vartheta_{\text{diff}} - \vartheta_{\text{inc}})}{2n}\right) \cdot F\left(\frac{2\pi f_c}{c} La^-(\vartheta_{\text{diff}} - \vartheta_{\text{inc}})\right), \tag{2.25}$$

$$D_3 = \cot\left(\frac{\pi + (\vartheta_{\text{diff}} + \vartheta_{\text{inc}})}{2n}\right) \cdot F\left(\frac{2\pi f_c}{c} La^+(\vartheta_{\text{diff}} + \vartheta_{\text{inc}})\right), \tag{2.26}$$

$$D_4 = \cot\left(\frac{\pi - (\vartheta_{\text{diff}} + \vartheta_{\text{inc}})}{2n}\right) \cdot F\left(\frac{2\pi f_c}{c} La^-(\vartheta_{\text{diff}} + \vartheta_{\text{inc}})\right), \tag{2.27}$$

where

$$F(x) = 2j\sqrt{x}e^{jx} \int_{\sqrt{x}}^{\infty} e^{-ju^2} du, \tag{2.28}$$

is the transition function, which involves a Fresnel integral and forces the GTD diffracted field to remain bounded across the shadow boundaries, and

$$L = \frac{s_{\text{diff}} s'_{\text{diff}}}{s_{\text{diff}} + s'_{\text{diff}}} \sin^2 \beta_0, \tag{2.29}$$

$$a^{\pm}(\xi) = 2\cos^2\left(\frac{2n\pi N^{\pm} - \xi}{2}\right), \tag{2.30}$$

where $N^{\pm}$ are the integers which most closely satisfy the equation $2n\pi N^{\pm} - \xi = \pm\pi$.

2.4 Penetration

As mentioned, when a plane wave is incident on a homogeneous dielectric, part of the energy is reflected back to the first medium and part of the energy is transmitted into the second medium. Penetration in RT is implemented based on the GO algorithm on refraction. Due to the transition between two media with different refraction indices n_1 and n_2, penetration changes the direction of a ray. Snell's law is used to describe the relationship between the angles of incidence and penetration with respect to the refraction indices as

$$\frac{\sin \vartheta_{\text{inc}}}{\sin \vartheta_{\text{pen}}} = \frac{n_2}{n_1}, \tag{2.31}$$

where ϑ_{pen} is the angle of penetration. The refraction index is inverse proportional to the phase velocity of the wave in the medium. If $n_1 > n_2$, $\sin \vartheta_{\text{pen}}$ may exceed unity. Therefore, a critical incidence angle is defined for $\vartheta_{\text{pen}} = \pi/2$ as

$$\vartheta_{\text{inc,cri}} = \arcsin \frac{n_2}{n_1}. \tag{2.32}$$

When $\vartheta_{\text{inc}} > \vartheta_{\text{inc,cri}}$, total internal reflection occurs, hence no propagation is penetrating into the medium characterized by n_2. The illustration of the refraction

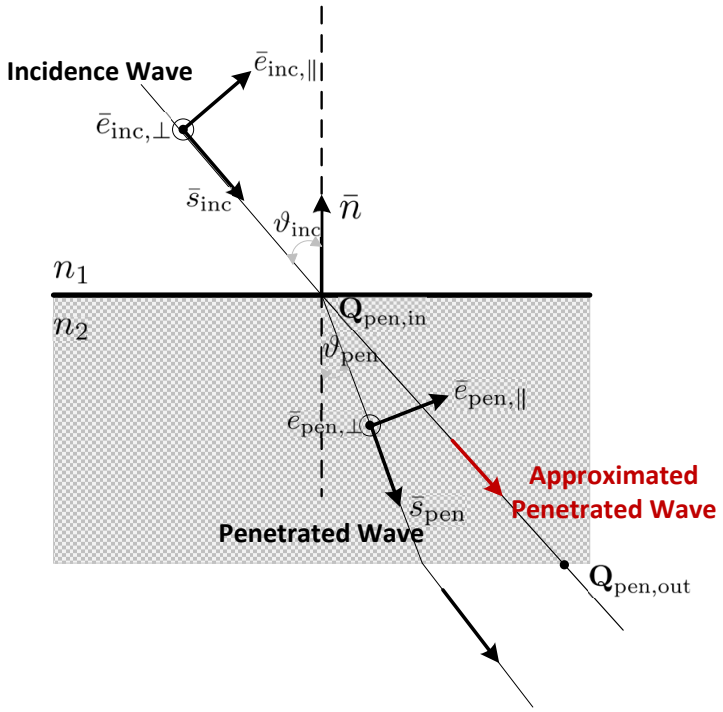

Figure 2.5: Illustration of the refraction mechanism, the planes of incidence and penetrated waves and the approximated penetrated wave.

mechanism and the planes of incidence and penetrated waves are depicted in Fig. 2.5.

In the RT tool, only the direct penetrated field is considered, while multiple reflections inside the dielectric medium are ignored. Moreover, in order not to affect the generation of the image tree, a simple approximation is made that the direction of a penetrated path is not modified by this interaction. It is shown as the red solid line in Fig. 2.5. In the further explanation, the penetrated path length is evaluated by the approximated red line, while the correct angles are calculated by the refraction mechanism to evaluate the penetration coefficients.

The first-order complex electric field of the penetrated path E_{pen} at an observation point $\mathbf{P}$ on a perfect dielectric at center frequency f_{c} in RT can be expressed as

$$\begin{aligned} E_{\mathrm{pen},\mathbf{P}}(f_{\mathrm{c}}) =& A(f_{\mathrm{c}}, s) \cdot [\bar{g}^{\mathrm{R}}_{\mathrm{pen}}(f_{\mathrm{c}})]^* \cdot \overline{\overline{\mathbf{T}}}_{\mathrm{in}}(f_{\mathrm{c}}) \cdot \overline{\overline{\mathbf{T}}}_{\mathrm{out}}(f_{\mathrm{c}}) \cdot \\ & \bar{E}_{\mathrm{inc},\mathbf{Q}_{\mathrm{pen,in}}} \cdot s_{\mathrm{pen,in}} \cdot e^{\frac{-j2\pi f_{\mathrm{c}} s_{\mathrm{pen,out}}}{c}} e^{\frac{-j2\pi f_{\mathrm{c}} s_{\mathrm{in,out}}}{v_{\mathrm{m}}}}, \end{aligned} \tag{2.33}$$

where

$$\bar{E}_{\mathrm{inc},\mathbf{Q}_{\mathrm{pen,in}}} = [\bar{g}^{\mathrm{E}}_{\mathrm{pen}}(f_{\mathrm{c}})] \cdot \bar{E}_0 \frac{e^{\frac{-j2\pi f_{\mathrm{c}} s_{\mathrm{pen,in}}}{c}}}{s_{\mathrm{pen,in}}}, \tag{2.34}$$

$s = s_{\mathrm{pen,in}} + s_{\mathrm{pen,out}} + s_{\mathrm{in,out}}$ in $A(f_{\mathrm{c}}, s)$ is the total path length, where $s_{\mathrm{pen,in}}$ is the path length from the Tx to the incoming penetration interaction point $\mathbf{Q}_{\mathrm{pen,in}}$, $s_{\mathrm{pen,out}}$ is the path length from the outgoing reflection interaction point $\mathbf{Q}_{\mathrm{pen,out}}$ to the Rx, and $s_{\mathrm{in,out}}$ is the path length from $\mathbf{Q}_{\mathrm{pen,in}}$ to $\mathbf{Q}_{\mathrm{pen,out}}$, v_{m} is the phase velocity of light in the medium, and $\overline{\overline{\mathbf{T}}}_{\mathrm{in}}$ and $\overline{\overline{\mathbf{T}}}_{\mathrm{out}}$ are the Fresnel dyadic penetration coefficients. At each interaction the dyadic is formed by the parallel and perpendicular polarization coefficients, taking $\overline{\overline{\mathbf{T}}}_{\mathrm{in}}$ as an example, as following

$$\overline{\overline{\mathbf{T}}}_{\mathrm{in}} = T_{\parallel} \bar{e}_{\mathrm{inc},\parallel} \bar{e}_{\mathrm{pen},\parallel} + T_{\perp} \bar{e}_{\mathrm{inc},\perp} \bar{e}_{\mathrm{pen},\perp}, \tag{2.35}$$

where $T_{\parallel}$ and $T_{\perp}$ are parallel and perpendicular polarization coefficients, which are denoted separately as

$$T_{\parallel} = \frac{2\sqrt{\varepsilon_{1r,\mathrm{eff}}/\varepsilon_{2r,\mathrm{eff}}}\cos\vartheta_{\mathrm{inc}}}{\cos\vartheta_{\mathrm{inc}} + \sqrt{\varepsilon_{1r,\mathrm{eff}}/\varepsilon_{2r,\mathrm{eff}}(1 - \varepsilon_{1r,\mathrm{eff}}/\varepsilon_{2r,\mathrm{eff}}\sin^2\vartheta_{\mathrm{inc}})}}, \tag{2.36}$$

and

$$T_{\perp} = \frac{2\cos\vartheta_{\mathrm{inc}}}{\cos\vartheta_{\mathrm{inc}} + \sqrt{\varepsilon_{2r,\mathrm{eff}}/\varepsilon_{1r,\mathrm{eff}} - \sin^2\vartheta_{\mathrm{inc}}}}, \tag{2.37}$$

where $\varepsilon_{1r,\mathrm{eff}}$ is the effective permittivity of the medium before the interaction and $\varepsilon_{2r,\mathrm{eff}}$ is the effective permittivity of the medium after the interaction.

2.5 Diffuse Scattering

Scattering on rough surface is very important for wireless communications [1]. A flat wave is scattered into multiple (random) directions due to interaction with a rough surface, which is opposed to specular reflection in a single direction on a smooth surface, as shown in Fig. 2.6. Actually, the same surface may be rough or smooth depending on the frequency of the impinging wave and the angle of incidence ϑ_{inc}. A surface can be assumed smooth if the generated waves have a small phase difference with each other. This leads to the well known Rayleigh criterion for a rough surface [10]

$$\Delta h > \frac{\lambda}{8\cos\vartheta_{\mathrm{inc}}}, \tag{2.38}$$

where Δh is the height of the roughness.

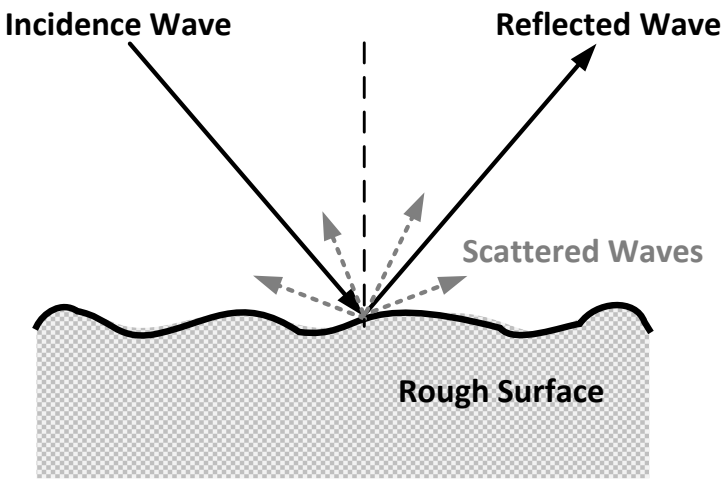

Figure 2.6: Scattering on rough surface.

In fact, it is very difficult to model the roughness of a building surface, even for statistical description. Since the surface irregularities cannot be modeled as Gaussian surface roughness, which is assumed in most theoretical models [2]. For a RT implementation, not only the roughness but also all the other deviations from an ideal smooth surface, such as irregularities, inhomogeneities and small objects, are impossible to be modeled in the input database. A simple ER model for diffuse scattering has been developed in [73], which takes into account all these characteristics. In the ER model, the field scattered by the generic surface element dS, shown in Fig. 2.7, is modeled as a non-uniform spherical wave originating from the center of each surface element and propagating in the upper half space.

Firstly, the rough surface needs to be divided into multiple tiles for the diffuse scattering components calculation. The tile size is evaluated by recursively subdividing the surface until the far-field condition is satisfied for each tile [50]. This subdivision algorithm is implemented in conventional RT. The far-field condition is expresses as

$$d_{\max} \leq \sqrt{\frac{d_s \lambda}{2}}, \qquad d_{\max} = \max(d_1, d_2), \tag{2.39}$$

where $d_{\max}$ is the maximum dimension of a surface tile, d_1 and d_2 are the two dimensions of a rectangular surface tile, and d_s is the distance between the center of the tile and the terminal from which the wave is coming from. In the beginning, the far-field condition is checked for the entire surface. If the condition is fulfilled, a further subdivision is no longer needed. Otherwise, the surface is equally divided

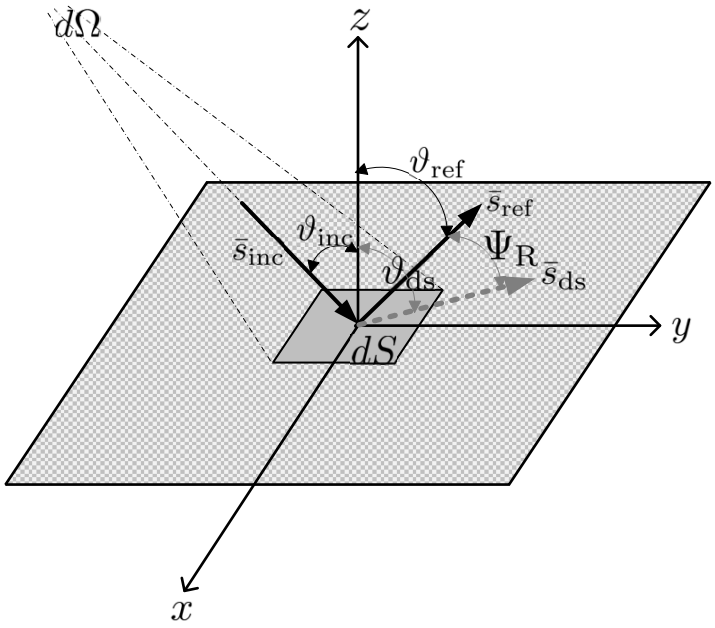

Figure 2.7: A generic surface element producing reflection and diffuse scattering as in [2].

into four rectangular tiles having in common the center of the original rectangular surface, or the surface is divided vertically or horizontally if the height of rectangular tile is more than twice of its width [10]. For each new tile, the far-field condition is further evaluated. Based on this subdivision algorithm, the distribution of tiles is related to the location of the terminal. It is possible that this subdivision algorithm leads to diffuse tiles with different sizes. The scattering coefficient S and the scattering pattern model is related to each surface. In conventional RT, the scattering coefficient is defined as

$$S = \left.\frac{|E_{\mathrm{ds}}|}{|E_{\mathrm{ref}}|}\right|_{dS}, \tag{2.40}$$

where $|E_{\mathrm{ds}}|$ and $|E_{\mathrm{ref}}|$ are the norms of the scattered and reflected fields on the surface tile dS, respectively. Then the reflection reduction factor R_{ref} is set as the amount of energy subtracted by scattering from the specular reflection, which is expressed as

$$R_{\mathrm{ref}} = \sqrt{1 - S^2}. \tag{2.41}$$

Therefore, the complex reflected field (2.33) needs to be multiplied with R_{ref} when considering diffuse scattering in RT.

The pattern models are used to calculate the amplitude of the scattered field. In

addition, a random phase is assumed to be associated with each diffuse scattering path with an uniform distribution in $[0, 2\pi]$. In the following, three pattern models associated with the ER approach presented in [2] are introduced. The three pattern models include Lambertian, directive and backscattering models.

The ***Lambertian model*** assumes that the scattering radiation lobe has its maximum in the direction perpendicular to the surface tile. The amplitude of the scattered field from a surface tile at an observation point $\mathbf{P}$ can be expressed as

$$|E_{\mathrm{ds},\mathbf{P}}| = A(f_\mathrm{c}, s) \cdot [\bar{g}^{\mathrm{R}}_{\mathrm{ds}}(f_\mathrm{c})]^* \cdot (\frac{S \cdot U}{s_{\mathrm{ds}} s'_{\mathrm{ds}}}) \cdot (\frac{dS \cos\vartheta_{\mathrm{inc}} \cos\vartheta_{\mathrm{ds}}}{\pi})^{\frac{1}{2}} \cdot [\bar{g}^{\mathrm{E}}_{\mathrm{ds}}(f_\mathrm{c})] \cdot \bar{E}_0, \quad (2.42)$$

where $s = s_{\mathrm{ds}} + s'_{\mathrm{ds}}$ in $A(f_\mathrm{c}, s)$ is the total path length, s_{ds} is the path length from Tx to the center of the tile dS and s'_{ds} is the path length from the center of the tile dS to the Rx, dS indicates the area of the tile, $U = |E_{\mathrm{ref}}|/|E_{\mathrm{inc}}|$, and ϑ_{ds} is the angle of the scattering direction, respectively.

The ***directive model*** assumes that the scattering lobe is steered towards the direction of the specular reflection. The amplitude of the scattered field from a surface tile can be calculated as

$$|E_{\mathrm{ds},\mathbf{P}}| = A(f_\mathrm{c}, s) \cdot [\bar{g}^{\mathrm{R}}_{\mathrm{ds}}(f_\mathrm{c})]^* \cdot \frac{S \cdot U}{s_{\mathrm{ds}} s'_{\mathrm{ds}}} \cdot (\frac{dS \cos\vartheta_{\mathrm{inc}}}{F_{\alpha_\mathrm{R}}})^{\frac{1}{2}} \cdot (\frac{1 + \cos\Psi_\mathrm{R}}{2})^{\frac{\alpha_\mathrm{R}}{2}} \cdot [\bar{g}^{\mathrm{E}}_{\mathrm{ds}}(f_\mathrm{c})] \cdot \bar{E}_0, \quad (2.43)$$

where Ψ_R is the angle between the specular reflection direction and the scattering direction, α_R is an integer defined as the width of the scattering lobe, and F_{α_R} is a function of α_R as

$$F_{\alpha_\mathrm{R}} = \frac{1}{2^{\alpha_\mathrm{R}}} \cdot \sum_{l=0}^{\alpha_\mathrm{R}} \binom{\alpha_\mathrm{R}}{l} \cdot I_l, \quad (2.44)$$

where I_l is defined as

$$I_l = \frac{2\pi}{l+1} \cdot \left[\cos\vartheta_{\mathrm{inc}} \cdot \sum_{w=0}^{\frac{l-1}{2}} \binom{2w}{w} \cdot \frac{\sin^{2w}\vartheta_{\mathrm{inc}}}{2^{2w}} \right]^{\frac{1-(-1)^l}{2}}. \quad (2.45)$$

The ***backscattering model*** is similar as the directive model, but considering an additional term accounting for the backscattering phenomenon. In several practical situations within the presence of large irregularities, the diffuse scattering radiation may arise even in the incidence direction. The expression of the amplitude of the scattered field is

$$\begin{aligned} |E_{\mathrm{ds},\mathbf{P}}| =& A(f_\mathrm{c}, s) \cdot [\bar{g}^{\mathrm{R}}_{\mathrm{ds}}(f_\mathrm{c})]^* \cdot \frac{S \cdot U}{s_{\mathrm{ds}} s'_{\mathrm{ds}}} \cdot (\frac{dS \cos\vartheta_{\mathrm{inc}}}{F_{\alpha_\mathrm{i},\alpha_\mathrm{R}}})^{\frac{1}{2}} \cdot \\ & \left[\Lambda \left(\frac{1 + \cos\Psi_\mathrm{R}}{2} \right)^{\alpha_\mathrm{R}} + (1 - \Lambda) \left(\frac{1 + \cos\Psi_\mathrm{i}}{2} \right)^{\alpha_\mathrm{i}} \right]^{\frac{1}{2}} \cdot [\bar{g}^{\mathrm{E}}_{\mathrm{ds}}(f_\mathrm{c})] \cdot \bar{E}_0, \end{aligned} \quad (2.46)$$

where α_{i} is an integer defined as the width of the backscattering lobe, $\Lambda \in [0,1]$ is the repartition factor between the amplitudes of two lobes, Ψ_{i} is the angle between the incidence direction and the scattering direction and

$$F_{\alpha_{\mathrm{i}},\alpha_{\mathrm{R}}} = \frac{\Lambda}{2^{\alpha_{\mathrm{R}}}} \cdot \left[\sum_{l}^{\alpha_{\mathrm{R}}} \binom{\alpha_{\mathrm{R}}}{l} \cdot I_l \right] + \frac{1-\Lambda}{2^{\alpha_{\mathrm{i}}}} \left[\sum_{l}^{\alpha_{\mathrm{i}}} \binom{\alpha_{\mathrm{i}}}{l} \cdot I_l \right], \tag{2.47}$$

where I_l is defined as in (2.45).

In order to obtain the complex scattered field, a random phase is involved as

$$E_{\mathrm{ds},\mathbf{P}} = |E_{\mathrm{ds},\mathbf{P}}| e^{-j\theta_{\mathrm{ds}}}, \tag{2.48}$$

where θ_{ds} is a random phase component with an uniform distribution over $[0, 2\pi]$.

2.6 Antenna Implementation

Channel measurements clearly need to be done with specific antennas. The inclusion of the antenna radiation pattern is a great advantage of a 3D RT tool. Taking into account that the DoD and DoA of a ray is intrinsically known by RT, any antenna with known radiation pattern can be implemented. At the Tx side, a complex 3D vector is generated according to the radiation and polarization properties of the antenna in the DoD of the ray. Similarly, at the Rx side, a complex 3D vector presenting the impinging wave is projected on the vector representing the radiation and polarization properties of the antenna in the DoA of the ray [10]. Moreover, it is flexible to consider or not consider the antenna radiation pattern by RT.

2.7 Channel Transfer Function Based on Ray Tracing

Based on the obtained complex electric field of each propagation path, the CTF of conventional RT can be calculated as

$$H(f) = \sum_{l=1}^{L} \eta_l e^{-j2\pi\tau_l f}, \tag{2.49}$$

where $f \in [-B/2, B/2]$ is the sampled frequency, $l \in [1, L]$ is the index of the propagation path, L is the total number of propagation paths, $\eta_l = E_{\{\cdot\}}$ is the complex-valued weighting coefficient of the $l-$th path, and τ_l is the delay of the $l-$th path. Please note that conventional RT is only calculated at the center frequency f_{c} for the narrowband or wideband scenario. Depending on the output parameters at f_{c}, the CTF in the entire bandwidth B can be calculated as (2.49).

3 Ray Tracing for Wideband Indoor Scenarios

It is an important fundamental concept to define a wireless communication system as narrowband or wideband system. The definition actually depends on the bandwidth of the physical channel. The term "narrowband" is used to describe a system where the system bandwidth does not exceed the coherence bandwidth of the physical channel, while a system is wideband if its bandwidth is larger than the coherence bandwidth of the physical channel. As explained in Chapter 1, narrowband systems are affected by frequency flat fading, whereas wideband systems are affected by frequency selective fading. In this thesis, wideband systems are considered.

In order to accelerate the execution of RT, the Matlab code is firstly optimized by converting time-consuming algorithms to MEX functions using MATLAB Coder. In addition, an efficient subdivision algorithm based on concentric circles is developed and evaluated. Furthermore, for simulating the radio propagation conditions for a mobile terminal, a RT algorithm based on two-dimensional DPS sequences is proposed. In this chapter, these contents are included and presented.

3.1 MEX Function

It is possible to compile C/C++ code so that it is callable from Matlab. MEX function is such an external interface function. MEX enables the high performance of C/C++ code working within the Matlab environment. By replacing the Matlab code with automatically generated MEX functions, computationally intensive simulations can be accelerated significantly.

3.1.1 Matlab Coder

MATLAB Coder enables the automatic conversion of Matlab .m code to standalone C/C++ code which is portable and readable. To generate MEX functions, the following products must be installed: Matlab, Matlab Coder and a C/C++ compiler. One can use the 'mex - setup' command to change the default compiler. The general

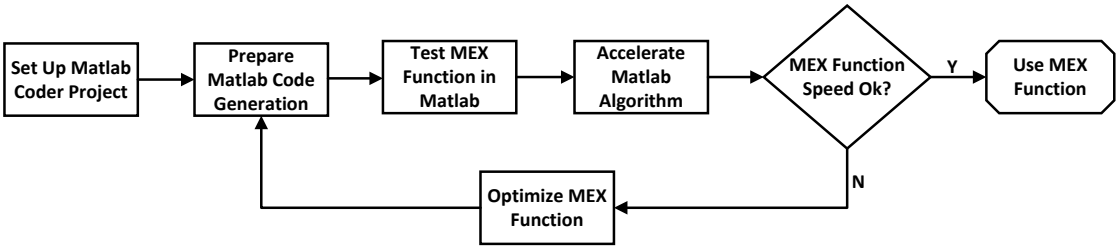

Figure 3.1: Workflow overview of Matlab Coder.

workflow using Matlab Coder is shown in Fig. 3.1 [74]. The first step is to create a Matlab Coder project for the relevant Matlab file in the current folder. MATLAB Coder must determine the properties of all variables in the MATLAB file at compile time, so it is significant to specify the properties of all function inputs. Using the project user interface, the types of input parameters involved in the Matlab function should be stated and the entry-point Matlab function file should be added. If global variables are used in the Matlab function, not only global type definition but also the initial value for such parameter should be stated before building the MEX function. Moreover, in order to use the Code Analyzer to identify warnings and errors specific to MATLAB for code generation, the %#codegen directive should be added to the MATLAB file. In MATLAB R2012b, the next step is to click the 'Build' button, then a MEX function can be generated. Meanwhile, MATLAB Coder produces a report that diagnoses errors, which must be fixed to make the MATLAB function compliant for code generation. An iterative process between fixing errors and regenerating a MEX function is needed until the MATLAB function is suitable for code generation. While in MATLAB R2015a, the next step is to click the 'Check for Run-Time Issues' button, then a tested MEX function and a report are generated. By default, the MEX function includes memory integrity checks. This step is optional, but it can help to detect and fix run-time errors. Until all the errors are fixed, we can click the 'Generate' button to generate the final MEX function.

The speed of the generated MEX function should be checked. The original MATLAB code can be replaced by the MEX function if the speed of the MEX function is faster than the original MATLAB code. For generating efficient and standalone C/C++ code, some key points are listed below for consideration [74]:

- *Data types*: Before using variables, MATLAB Coder requires a complete assignment to each variable, including type, dimension and initial values. Please note that one should not forget those variables used in child functions.

- *Array sizing*: Variable-size arrays and matrices are supported for code generation. The size of such variable can be predefined, which should be large enough to cover all its variation in size at run time.

- *Memory*: For generated code static or dynamic memory allocation can be selected. Dynamic memory allocation potentially uses less memory at the expense of time to manage the memory. With static memory, better speed can be achieved at the expense of higher memory usage.

- *Speed*: Loading large-size global variables is very time-consuming, which may lead to no efficiency improvement or even lower efficiency by comparing with the original MATLAB function. Choosing a suitable C/C++ compiler instead of using the default compiler is helpful for improving the speed of the generated code. Disabling run-time checks also can make faster simulations.

3.1.2 Acceleration of Reflection Algorithm

An efficient algorithm to find propagation paths is the key point for a successful implementation of RT. Conventional RT implemented in MATLAB contains more than thirty MATLAB function files. Utilizing MATLAB Coder to generate MEX functions of time-consuming MATLAB algorithms can speedup the simulation time of RT. By evaluating the simulation time of all Matlab functions in the conventional RT tool, ten MATLAB functions are selected and replaced by their corresponding MEX functions. It is known that the computational complexity of RT scales directly with the number of propagation paths, of which the reflection and diffuse scattering paths comprise a large proportion. In this section, the original implementation of finding reflection paths is firstly introduced. In order to make the MATLAB function compliant for code generation and to save the memory when building the image tree of the reflection algorithm, an efficient implementation is presented. The acceleration of the implementation of the diffuse scattering algorithm can be found in [75].

3.1.2.1 Original Implementation of Finding Reflection Paths

The RT algorithm uses two main steps for the calculation of reflection paths: i) the visibility procedure and ii) the backtracking procedure. The visibility procedure is used to build up the image tree and the backtracking procedure helps to determine the real reflection paths. For the visibility procedure, the image principle is the foundation. The image principle is performed from Tx to Rx. For the backtracking procedure, the valid reflection paths are found. It is performed from Rx to Tx.

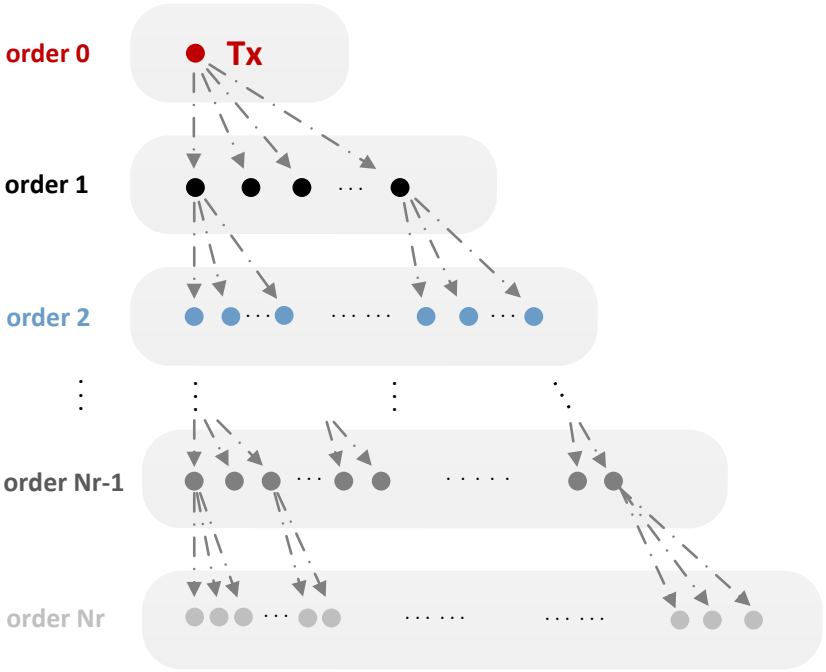

Figure 3.2: Structure of image tree in original implementation.

The implementation of the image tree construction in RT is shown in Fig. 3.2, where a tree structure containing all images is created and the images at different reflection orders are marked with distinct colors. The root node of the structure is the position of the Tx. The depth of the tree is set by the maximum reflection order N_r. The image tree is recursively built by applying the image principle, see Fig. 2.2. In the first step, the images of the Tx are generated according to each visible block surface, where the visibility is confirmed by the normal unit vector facing towards the Tx. These nodes, marked as black solid circles, indicate the images at the first order. At order $n_\mathrm{r} > 1$, the images at the $n_\mathrm{r} - 1$ order are generated in the similar way. Moreover, three pointers are used for building the image tree. The first pointer is used to connect each node at any order $n_\mathrm{r} > 1$ with the mother node at the order $n_\mathrm{r} - 1$. The second pointer is used to connect each node at any order $n_\mathrm{r} > 1$ with the following node at the same order. The third pointer connects the node at any order n_r excluding the maximum order with the relevant nodes at the order $n_\mathrm{r} + 1$. Each node stores the coordinate of the image point, the relevant surface for calculating this image point, and the relevant pointers for the previous and next levels. The visibility procedure is repeated until the maximum reflection order N_r is reached.

Once the tree is completely built, for each reflection order $1 \leq n_\mathrm{r} \leq N_\mathrm{r}$, the rays

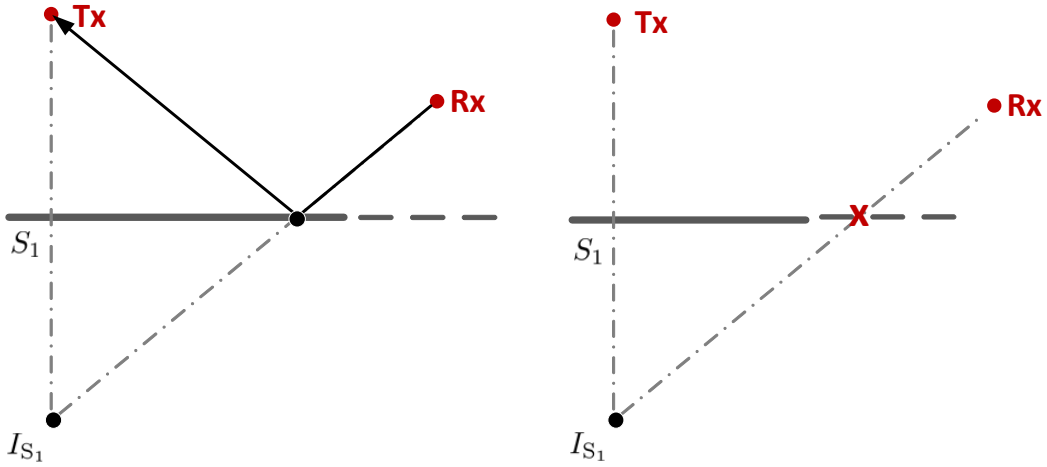

(a) An effective Image (b) A noneffective Image

Figure 3.3: An example of the definitions: (a) an effective image and (b) a noneffective image.

are traced backwards starting from the Rx along each node at reflection order n_r of the tree and stops when the root node Tx is reached. Then these traced paths are seen as valid reflection paths. An effective or a noneffective image is defined as whether there is a crossover point on the surface when drawing a line between the Rx and the image. An example based on a first order image point is shown in Fig. 3.3. The backtracking procedure strongly depends on the structure of the image tree. It can be seen from the image tree structure that the node number at each layer increases exponentially with the reflection order. It is also evident that not all the data saved in the image tree can provide a valid contribution as shown in Fig. 3.3 (b). However, the construction of the image tree may require a great amount of central processing unit (CPU) time and saving all the information for every node in the image tree requires a large amount of memory. This leads to the efforts presented in next section.

3.1.2.2 Efficient Implementation of Reflection Paths Identification

The key point of the reflection algorithm is to build the image tree and to use the backtracking procedure to find all valid reflection paths. It has been mentioned that three pointers are used for building the image tree. The involved pointers are saved in a cell array in conventional RT. This is because a cell array is an indexed list of data with symbolic names, which makes it more readable and much easier for a user to understand the structure of image tree. However, a cell array is not

supported by MATLAB Coder in MATLAB R2012b. Therefore, in order to generate MEX functions to accelerate the simulation, the data format needs to be updated. Combined with the memory issue, an efficient and improved implementation of the image tree construction and reflection path calculation is required.

Similarly, the image tree is also built from the Tx in the efficient implementation. However, the image tree is no longer recursively built. The effective implementation of building the image tree in RT is shown in Fig. 3.4. Firstly, the images of the Tx are generated according to each visible block surface. Secondly, for reflection order $n_\mathrm{r} > 1$, the image points of the first node at each reflection order n_r are calculated and stored in the next reflection order, until the maximum reflection order N_r is achieved. This initial image tree is marked with orange solid circles in Fig. 3.4. Meanwhile, effective images are selected based on the definition mentioned in Section 3.1.2.1. It works from the reflection order $n_\mathrm{r} = 1$ to N_r, where the nodes at previous reflection orders along with the first nodes at the current reflection order are ready for being checked. During this process, the noneffective images are discarded. The next step is that the processed nodes at the reflection order N_r and the first nodes at the reflection order $N_\mathrm{r} - 1$ are deleted from the image tree. Then the second node at the reflection order $N_\mathrm{r} - 1$ is seen as first node, and its relevant image points are calculated and stored as the first nodes at the reflection order N_r. Then the effective images are selected again based on this updated initial image tree. Until the process of the last node at the reflection order $N_\mathrm{r} - 1$ has been done, it returns to the second node at the reflection order $N_\mathrm{r} - 2$. This initial image tree is continuously updated during the whole process until the last node at the first reflection order is checked. The obvious feature of this efficient implementation is that i) we do not need to build the completed image tree, only the initial image tree is enough for finding the reflection paths, and ii) it combines the visibility with the backtracking procedures. Based on the proposed efficient implementation, the storage issue is completely solved.

In this efficient implementation, two pointer are needed for building the initial image tree. One pointer is used to connect each node at any order $n_\mathrm{r} > 1$ with the mother node at order $n_\mathrm{r} - 1$. The other pointer is used to connect each node at any order $n_\mathrm{r} > 1$ with the following node at the same order. Coming back to the data format issue in generating the MEX function, the cell array format is changed to a 3D matrix. According to the maximum reflection order N_r and the number of blocks N_b in the considered scenario, its size is defined as $N_\mathrm{r} \times N_\mathrm{b} \times 5$. The new implementation needs less information for each node. For the dimension '5', it contains

- $1 \sim 2$: indexes of the block and its surface,

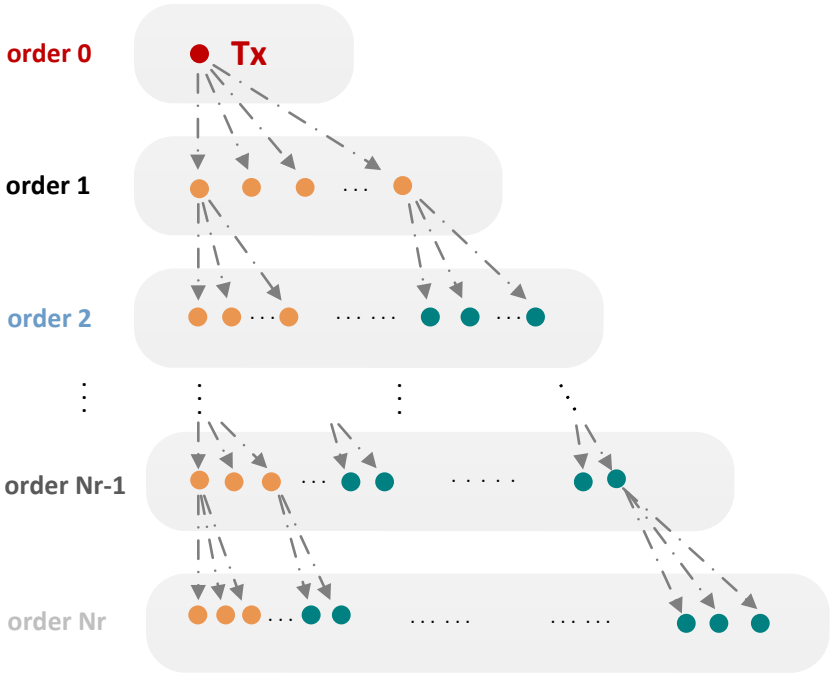

Figure 3.4: Structure of image tree in effective implementation.

- $3 \sim 5$: coordinates of the image point.

It is noteworthy that the proposed efficient implementation aims at improving the simulation efficiency of conventional RT, which does not change the accuracy of the final prediction result compared with the original implementation.

3.1.3 Simulation Time Comparison

A simulated indoor scenario is given in Fig. 3.5 to compare the simulation time of the original MATLAB implementation with the one based on the updated MEX functions. The dimension of the room is about 29 m $\times$ 13.25 m $\times$ 4.6 m. There are 10 blocks including the ceiling and the floor in the scenario. The materials sketched with grey, yellow and red represent concrete, brick and wood walls, respectively. In Fig. 3.5, some visualized propagation paths are also presented.

We take into account LOS, up to fourth-order reflection, single-order diffraction, single-bounce scattering, reflection-scattering and scattering-reflection cases in RT. Note that the penetration case is embedded into these contributions. To show the efficiency improvement intuitively, the simulation time based on the original and the updated code is shown in Fig. 3.6. The blue bar represents the simulation time

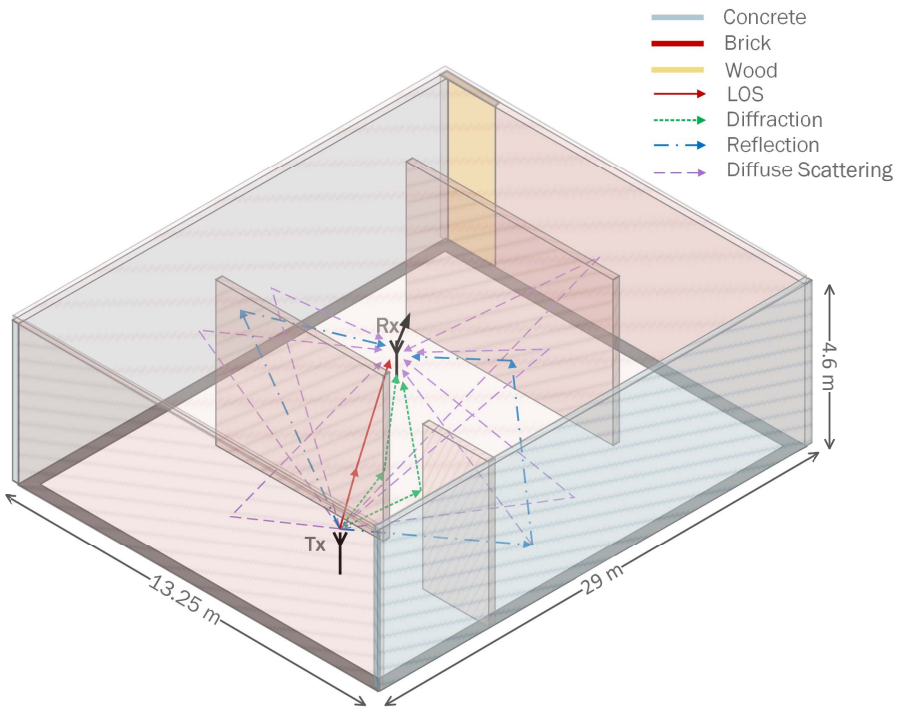

Figure 3.5: An indoor scenario for testing the simulation time.

needed for the original MATLAB code, while the orange bar indicates the time consumption of the update code. According to the efficient implementation of the reflection algorithm mentioned in Section 3.1.2.2, the simulation time is extremely reduced from 154 s to 3 s. Considering all generated MEX functions, about 90% total simulation time of the original code is saved.

3.2 Effective Subdivision Algorithm

It is known that the accuracy of RT comes at the cost of a high computational complexity, which directly scales with the number of propagation paths considered. The diffuse scattering components constitute a high proportion of all the propagation paths, which is closely related to the diffuse scattering tile size. There exist different subdivision algorithms. The surfaces are divided into 2272 diffuse scattering tiles within the size 0.5×0.5 m^2 in [76], while there are 400 scattering tiles within the same size placed around each specular reflection interaction point in [49]. In [50], the size of each diffuse scattering tile is evaluated by recursively dividing the surface until the far-field condition is fulfilled. It is obvious that the obtained diffuse scattering tiles

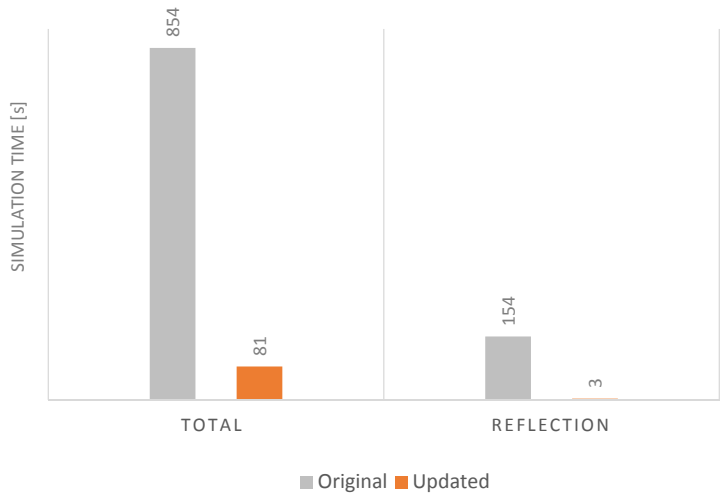

Figure 3.6: Simulation time comparison based on the original and the updated code.

of all these mentioned subdivision methods are related to the specific scenarios. For conventional RT in this thesis, the latter subdivision algorithm is applied. However, in case the terminal is very close to the surface of an object, the subdivision algorithm of [50] would lead to a large amount of tiles with small sizes, which in turn results in an extremely high computational complexity.

In this section, a novel and efficient subdivision algorithm based on concentric circles for diffuse scattering is proposed. This algorithm can be used as a general procedure to subdivide rough surfaces. It consists of two main parts: i) the generation of diffuse scattering tiles, which fully demonstrates the random characteristic of diffuse scattering, and ii) the proper tile size calculation, which is related to the system bandwidth and is scenario independent. Moreover, the accuracy of the proposed algorithm is tested by comparing with the proven subdivision algorithm of diffuse scattering [50]. The numeric simulations include the PDP, RMS delay and angular spreads. Furthermore, the computational complexity of diffuse scattering in RT is tested.

3.2.1 New Subdivision Algorithm

A new subdivision algorithm, based on concentric circles, is developed in the present work. It is assumed that the diffuse scattering tiles are equally sized circular segments within the same radius Δd on a certain surface and the diffuse scattering path originates from the center of each tile. The algorithm includes two main parts: i) the generation of diffuse scattering tiles and ii) the proper tile size calculation.

3.2.1.1 Generation of Diffuse Scattering Tiles

The principle of the generation algorithm is shown in Fig. 3.7, whose procedure is as following: Firstly, a random point c_s is placed on the rough surface as the

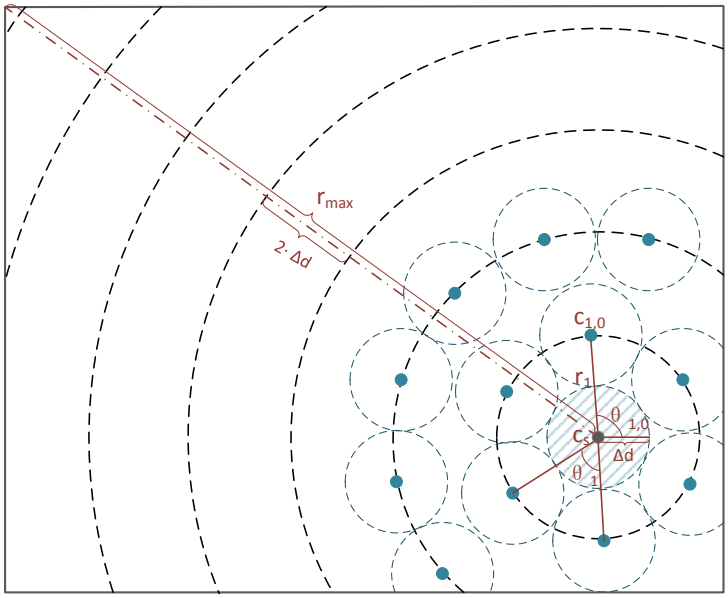

Figure 3.7: The principle of the generation of diffuse scattering tiles.

center point of the concentric circles, whose coordinate is indicated as $(x_\mathrm{c}, y_\mathrm{c}, z_\mathrm{c})$. The radius r_n of these concentric circles is defined as

$$r_n = \begin{cases} \Delta d & \text{if } n = 0, \\ 2n \cdot \Delta d & \text{if } n = 1, \ldots, N, \end{cases} \tag{3.1}$$

where n is the index of the concentric circle and N is the number of concentric circles. The distance r_max between the center c_s and the furthest vertex of the rectangular surface can be obtained, which helps to determine

$$N = \lfloor \frac{r_\mathrm{max}}{2 \cdot \Delta d} \rfloor, \tag{3.2}$$

where $\lfloor \cdot \rfloor$ takes the next smallest integer toward minus infinity.

Secondly, starting from $n = 1$, circular scattering tiles are generated on each concentric circle separately. The first diffuse scattering tile at each concentric circle, whose center is denoted as $c_{\mathrm{n},0}$, is located at a random angle $\theta_{n,0}$ within the region $[0, 2\pi)$. Based on the triangular relationship, the angle resolution θ_n, which is the

angle difference between two adjacent tile centers on the same concentric circle, can be calculated as

$$\theta_n = 2\arcsin(\frac{1}{2\cdot n}),\ n = 1, \ldots, N. \tag{3.3}$$

Furthermore, the corresponding coordinate of the tile center $(x_{n,\mathrm{s}}, y_{n,\mathrm{s}}, z_{n,\mathrm{s}})$ can be obtained. For example, if the surface is horizontal, the coordinate is calculated as

$$\begin{cases} x_{n,\mathrm{s}} = x_{\mathrm{c}} + r_n \cdot \cos\theta, \\ y_{n,\mathrm{s}} = y_{\mathrm{c}} + r_n \cdot \sin\theta, \\ z_{n,\mathrm{s}} = z_{\mathrm{c}}, \end{cases} \tag{3.4}$$

where $\theta = \theta_{n,0} + l_{\mathrm{c},n} \cdot \theta_n$ and $l_{\mathrm{c},n} \in [1, N_{\mathrm{c},n}]$ is the index of the circular tile on each concentric circle, where $N_{\mathrm{c},n}$ is the number of circular tiles, defined as

$$N_{\mathrm{c},n} = \lfloor \frac{2\pi}{\theta_n} \rfloor. \tag{3.5}$$

The procedure described above is repeated until reaching the last concentric circle. The random angle $\theta_{n,0}$ is chosen independently for each concentric circle. It should be noticed that some circular tiles are too close to the edge and the portions outside the surface are cut off. However, we still assume the size of those incomplete circular tiles as dS. The unused areas among all obtained circular tiles can make this compensation, which guarantees that the surface is not over occupied.

3.2.1.2 Proper Tile Size Calculation

The remaining problem is how to determine a proper tile size dS. We propose an approach, which depends on the system bandwidth B. Strictly speaking, it should be the bandwidth used in the RT simulation [1]. The tile size is expressed as

$$dS = \pi \cdot \Delta d^2 = \pi \cdot \left(\frac{c}{2\cdot B}\right)^2. \tag{3.6}$$

It is known that the delay resolution is defined as $1/B$. Therefore, this calculation means that the distance between any two circular tile centers on one surface is not shorter than the distance which is corresponding to the delay resolution. This condition serves to ensure that any diffuse scattering paths on one surface would not be overlapped in the same delay bin.

[1] The bandwidth of the sub-band B_{i} is applied in the sub-band divided RT for an UWB case [62].

Table 3.1: Simulation Parameters

Parameter	Value
Carrier frequency f_c	2.45 GHz
Bandwidth B	480 MHz
Rx velocity $\|\boldsymbol{v}_{\mathrm{Rx}}\|$	3 km/h
Sampling rate in distance $\|\boldsymbol{x}_{\mathrm{S}}\|$	0.02 m
Number of Rx positions N_{Rx}	10
Number of frequency samples N_{f}	480

3.2.2 Simulation Configuration

In order to show the performance of the proposed subdivision algorithm, an indoor scenario is generated. The indoor scenario used in this work is the same as in Fig. 3.5. The dielectric properties of the materials are included in the input database. The values of the relative permittivity and conductivity of the materials are: $\varepsilon_r = 6$ and $\sigma = 0.08$ S/m for concrete blocks, $\varepsilon_r = 4$ and $\sigma = 0.005$ S/m for brick blocks, and $\varepsilon_r = 2.1$ and $\sigma = 0.05$ S/m for wood blocks, respectively [60]. The Tx and the Rx antennas used in the present work are dipole antennas. The Rx antenna is linearly moving with a constant speed along a constant direction for a short distance. Simulation parameters are summarized in Table 3.1.

We take into account single-bounce scattering, reflection-scattering and scattering-reflection cases in all simulations here. Each diffuse scattering process is associated with a uniformly distributed random phase. In order to overcome the randomness, the channel simulation at each time sample is averaged over five realizations [53]. Therefore, there are 50 channel realizations obtained in total at the simulated Rx positions $N_{\mathrm{Rx}} = 10$. According to the simulation parameters, $dS = 0.3068$ m^2 for the proposed subdivision algorithm based on (3.6).

3.2.3 Numerical Results

The CIR $h(\tau)$ at one Rx location in conventional RT can be obtained by using the inverse Fourier transform of the CTF described in (2.49). The time-variant CIR is expressed as $h(\tau, n_{\mathrm{Rx}})$, where n_{Rx} is the index of the Rx position. The comparison between the proposed and the original subdivision algorithms is presented in this section. Meanwhile, we also consider using different tile sizes dS to check the relevant results.

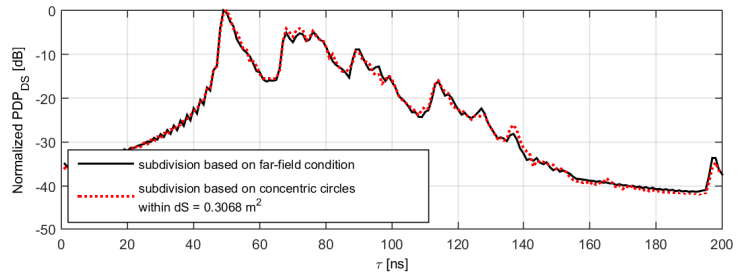

(a) Normalized $\mathrm{PDP_{DS}}$ comparison

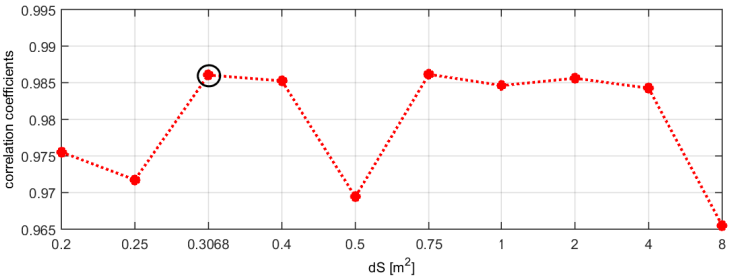

(b) Correlation coefficients of the different PDPs

Figure 3.8: (a) Normalized $\mathrm{PDP_{DS}}$ comparison between the subdivision based on the far-field condition and concentric circles within $dS = 0.3068\mathrm{m}^2$, respectively; (b) Correlation coefficients between the subdivision based on the far-field condition and concentric circles within different dS.

3.2.3.1 PDP Comparison

Based on our numerical implementation, we compare the normalized PDP of diffuse scattering paths $\mathrm{PDP_{DS}}$ with different subdivision algorithms. The normalized $\mathrm{PDP_{DS}}$ is obtained by averaging absolute square values of the CIRs over Rx positions as (1.4), where RT simulations consider diffuse scattering components only. The results are shown in Fig. 3.8 (a), from which it can be observed that the $\mathrm{PDP_{DS}}$ based on concentric circles with $dS = 0.3068\ \mathrm{m}^2$ is similar to the one based on the far-field condition. The similarity between the PDPs of RT models with different subdivision algorithms is further investigated by calculating the correlation coefficients. The results are shown in Fig. 3.8 (b). The correlation coefficient of the proposed and the original $\mathrm{PDP_{DS}}$ is 0.986, while all correlation coefficients between the subdivision based on the far-field condition and concentric circles within $dS \in [0.2, 8]\mathrm{m}^2$ are larger than 0.965 .

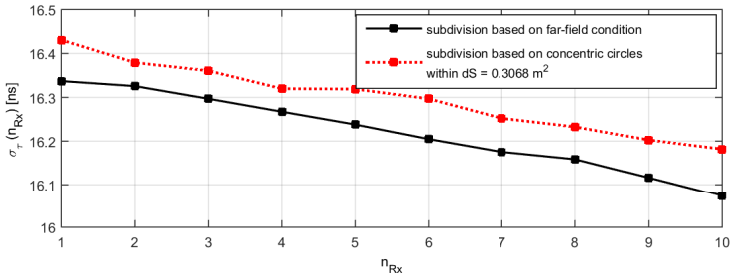

(a) Delay spread σ_τ comparison

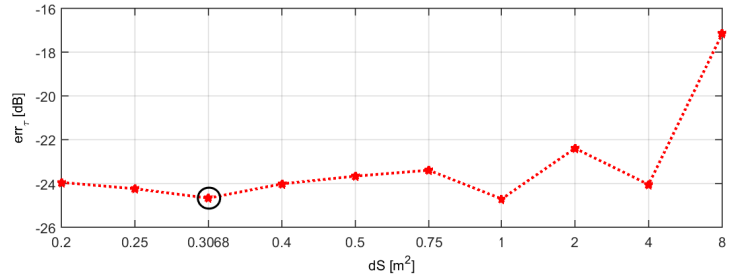

(b) MREs err_τ comparison

Figure 3.9: (a) Delay spread σ_τ comparison according to different Rx positions n_{Rx} between the subdivision based on the far-field condition and concentric circles within $dS = 0.3068\text{m}^2$, respectively; (b) MREs err_τ between the subdivision based on the far-field condition and concentric circles within different dS.

3.2.3.2 Delay Spread Comparison

Delay spread σ_τ at one Rx position, a measure for the time dispersion of the channel, is defined as in (1.7). The difference between the subdivision based on the far-field condition and the concentric circles is presented by the mean relative error (MRE) as

$$\text{err}_\tau = \frac{1}{N_{\text{Rx}}} \sum_{n_{\text{Rx}}=1}^{N_{\text{Rx}}} \frac{|\sigma_{\tau,\text{far}}(n_{\text{Rx}}) - \sigma_{\tau,\text{cir}}(n_{\text{Rx}})|}{\sigma_{\tau,\text{far}}(n_{\text{Rx}})}, \tag{3.7}$$

where $\sigma_{\tau,\text{far}}$ and $\sigma_{\tau,\text{cir}}$ are the delay spreads corresponding to the subdivision algorithm based on the far-filed condition and concentric circles, respectively.

The delay spread σ_τ comparison according to different Rx positions n_{Rx} between the subdivision based on the far-field condition and concentric circles within $dS = 0.3068\text{m}^2$ is shown in Fig. 3.9 (a). It can be seen that the delay spread difference between these two algorithms is always smaller than 0.1ns. Moreover, the MREs err_τ between the subdivision based on the far-field condition and concentric circles for different dS are shown in Fig. 3.9 (b). The MRE err_τ is about -25dB between the proposed and the original subdivision algorithms. All the MREs change in the

region $(-25, -17)$ dB within $dS \in [0.2, 8]\text{m}^2$. There is about 3 dB deviation from 0.2m^2 to 4m^2.

3.2.3.3 Angular Spread Comparison

For the angular spread comparison, the method is defined similarly as the delay spread comparison. The angular spread at one Rx position is defined as [77]

$$\sigma_\phi = \sqrt{\frac{\sum_{l=1}^{L} P_l \phi_i^2}{\sum_{l=1}^{L} P_l} - \left(\frac{\sum_{l=1}^{L} P_l \phi_l}{\sum_{l=1}^{L} P_l} \right)^2}, \tag{3.8}$$

where ϕ_l is either the azimuth or the elevation of arrival of the $l-$th diffuse scattering path, which are defined as azimuth of arrival (AoA) and elevation of arrival (EoA) in the analysis. The MRE of two different subdivision algorithms is defined as

$$\text{err}_\phi = \frac{1}{N_{\text{Rx}}} \sum_{n_{\text{Rx}}=1}^{N_{\text{Rx}}} \frac{|\sigma_{\phi,\text{far}}(n_{\text{Rx}}) - \sigma_{\phi,\text{cir}}(n_{\text{Rx}})|}{\sigma_{\phi,\text{far}}(n_{\text{Rx}})}. \tag{3.9}$$

where $\sigma_{\phi,\text{far}}$ is the angular spread corresponding to the subdivision algorithm based on the far-field condition and $\sigma_{\phi,\text{cir}}$ is the angular spread corresponding to the subdivision algorithm based on concentric circles.

Fig. 3.10 (a) gives the AoA spread $\sigma_{\text{AoA},\phi}$ comparison results according to different Rx positions n_{Rx} between the subdivision algorithm based on the far-field condition and concentric circles within $dS = 0.3068\text{m}^2$. The AoA spread variance based on two subdivision algorithms is always smaller than $0.2°$. Fig. 3.10 (b) shows the variation of $\text{err}_{\text{AoA},\phi}$ with dS. It can be observed that the MREs are changed in the region $(-35, -17)$ dB within $dS \in [0.2, 8]\text{m}^2$. Moreover, the minimum MRE is achieved when $dS = 0.3068\text{m}^2$ is obtained.

The relevant EoA spread comparison results is shown in Fig. 3.11. The $\sigma_{\text{EoA},\phi}$ difference according to n_{Rx} between the subdivision based on the far-field condition and the concentric circles within $dS = 0.3068\text{m}^2$ is always smaller than $0.05°$. Moreover, $\text{err}_{\text{EoA},\phi}$ values are changed in the region $(-30, -15)$ dB within $dS \in [0.2, 8]\text{m}^2$, in which $\text{err}_{\text{EoA},\phi} = -27.5$ dB when $dS = 0.3068\text{m}^2$. Both $\text{err}_{\text{AoA},\phi}$ and $\text{err}_{\text{EoA},\phi}$ are about 10 dB deviation from 0.2m^2 to 4m^2. Compared to the PDP and the delay spread comparison, the tile size dS influences the angular spread significantly.

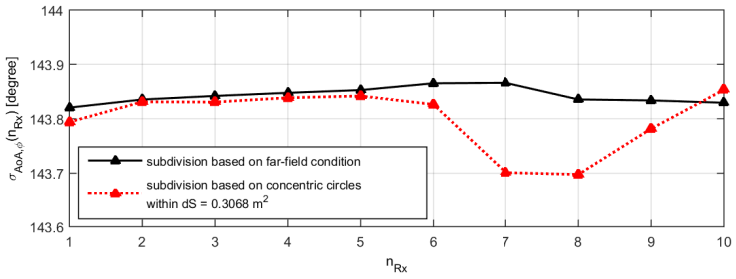

(a) AoA spread $\sigma_{\mathrm{AoA},\phi}$ comparison

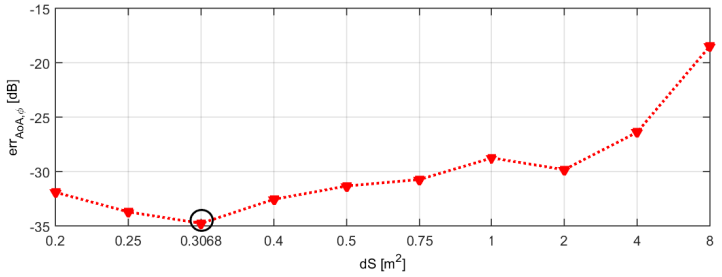

(b) MREs $\mathrm{err}_{\mathrm{AoA},\phi}$ comparison

Figure 3.10: (a) AoA spread $\sigma_{\mathrm{AoA},\phi}$ comparison according to different Rx positions n_{Rx}; (b) MREs $\mathrm{err}_{\mathrm{AoA},\phi}$ of the AoAs between the subdivision based on the far-field condition and concentric circles within different dS.

3.2.3.4 Computational Complexity

The numerical complexity is significantly reduced for the proposed subdivision algorithm. Considering one Rx position, there are 37889 and 21026 diffuse scattering paths obtained by the subdivision algorithms based on the far-field condition and concentric circles within $dS = 0.3068\mathrm{m}^2$, respectively. The corresponding simulation time is 81 s and 41 s (2.4GHz Intel Core i5 CPU with 4GB RAM). Compared with the subdivision algorithm based on the far-field condition, it can be analyzed that about 45% simulation time is saved based on the proposed subdivision algorithm.

3.3 RT Algorithm Using the DPS Subspace

We are also interested in simulating the radio propagation conditions for a mobile terminal, communicating in a frame based communication system indoors with several fixed nodes. This communication shall be used to obtain the position of the mobile terminal in indoor scenario. It is known that diffuse scattering components can be assumed spatially uncorrelated in indoor environments for different Tx and Rx coordinates separated by many multiple wavelength [50,52,53]. However, the cor-

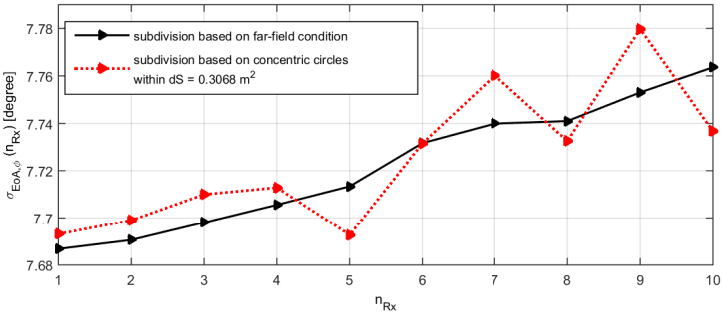

(a) EoA spread $\sigma_{\mathrm{EoA},\phi}$ comparison

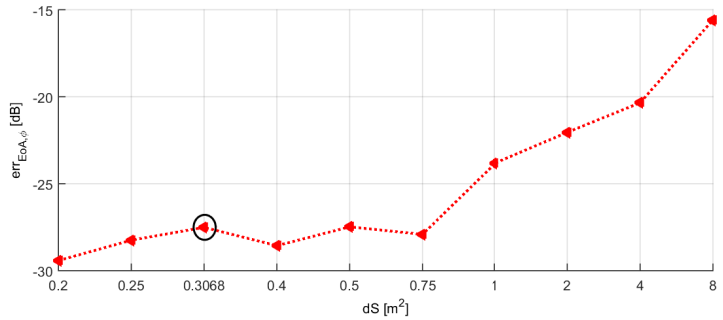

(b) MREs $\mathrm{err}_{\mathrm{EoA},\phi}$ comparison

Figure 3.11: (a) EoA spread $\sigma_{\mathrm{EoA},\phi}$ comparison according to different Rx positions n_{Rx}; (b) MREs $\mathrm{err}_{\mathrm{EoA},\phi}$ of the EoAs between the subdivision based on the far-field condition and concentric circles within different dS.

relation of diffuse scattering components needs to be considered in the time-variant case where the Rx is moving only a short distance. As it is known for frame based communication systems, the moving distance of the Rx during the transmission of a single frame is typically smaller than one wavelength. Therefore, the correlated temporal and spatial evolution of the channel impulse response is of utmost concern.

Moreover, for the test and development of indoor localization algorithms accurate indoor channel modeling is extremely important. It is well known that non-line-of-sight (NLOS) propagation paths introduce large errors for determining the mobile position. The reason is that localization algorithms often heavily rely on the information extracted from the LOS path such as the received signal strength, time of arrival, or time difference of arrival [78]. The diffuse scattering components take up a fairly large number of NLOS propagation paths in an indoor scenario. Therefore, diffuse scattering components are significant for indoor mobile localization and tracking algorithms. Recently, new localization methods have been proposed that can even take advantage of multipath propagation [79, 80].

Therefore, we propose a method in such time-variant indoor scenario to significantly reduce the computational complexity of RT by using a projection of all propagation paths on a subspace spanned by two-dimensional DPS sequences. In this scenario, we consider that (i) all objects and the Tx are static, and (ii) the Rx is moving with a constant speed along a linear trajectory. With our method the computational complexity can be reduced by more than one order of magnitude for indoor scenarios. The accuracy of the low-complexity DPS subspace based RT algorithm is verified by numeric simulations.

In this section, we firstly review general knowledge about multidimensional DPS sequences. Secondly, the implemented time-variant RT channel model is described. Then the low-complexity approximation algorithm to significantly reduce the computational complexity is introduced. Furthermore, we numerically evaluate the accuracy of the proposed RT algorithm.

3.3.1 Multidimensional DPS Sequences

In [81], Slepian raised the question which sequences are bandlimited to the frequency range $[-v_{\mathrm{Dmax}}, v_{\mathrm{Dmax}}]$ and simultaneously most concentrated in a certain time interval of length M. For both continuous and discrete time cases, Slepian found that the desired set of orthogonal sequences is the eigenfunctions of an integral operator and simultaneously of a commuting differential operator [82]. The discrete sequences v_m, we are looking for, shall have their maximum energy concentration on the index set $I \subset \mathbb{Z}$, where $\mathbb{Z}$ is the Euclidean space, i.e.

$$\lambda = \frac{\sum_{m \in I} |v_m|^2}{\sum_{m \in \mathbb{Z}} |v_m|^2}. \tag{3.10}$$

When v_m is bandlimited to W,

$$v_m = \int_W V(f) e^{2\pi j f m} df, \quad m \in \mathbb{Z}, \tag{3.11}$$

where

$$V(f) = \sum_{m \in \mathbb{Z}} v_m e^{-2\pi j f m}, \quad f \in \mathbb{R}. \tag{3.12}$$

Solutions of this constrained maximization problem are given by DPS sequences, which are a fundamental tool for understanding the extent to which sequences and their spectra can be simultaneously concentrated [81]. One-dimensional DPS sequences are introduced in [81], whose application includes spectrum estimation, approximation, and prediction of band-limited signals as well as channel estimation in wireless communication systems [83].

The one-dimensional DPS sequences $\nu_m^{(d)}(W, I)$ with band-limit region $W = [-v_{\mathrm{Dmax}}, v_{\mathrm{Dmax}}]$, where $v_{\mathrm{Dmax}} \ll 1/2$, and concentration region $I = \{M_0, \ldots, M_0 + M - 1\}$ are defined as the real solutions of [84]

$$\sum_{n=M_0}^{M_0+M-1} \frac{\sin(2\pi v_{\mathrm{Dmax}}(m-n))}{\pi(m-n)} v_n^{(d)}(W, I) = \lambda_d(W, I) v_m^{(d)}(W, I). \tag{3.13}$$

They are sorted such that their eigenvalues $\lambda_d(W, I)$ are in descending order as

$$\lambda_0(W, I) > \lambda_1(W, I) > \cdots > \lambda_{M-1}(W, I). \tag{3.14}$$

The DPS vector $\boldsymbol{v}^d(W, I) \in \mathbb{C}^M$ is defined as the DPS sequence $v_m^{(d)}(W, I)$ index-limited to I. Moreover, the DPS vectors $\boldsymbol{v}^d(W, I)$ are also eigenvectors of the $M \times M$ matrix $\boldsymbol{K}$ with the element $K_{m,n} = \sin(2\pi v_{\mathrm{Dmax}}(m-n))/\pi(m-n)$. Some properties of DPS sequences are listed as follows [84]

- The sequences $v_m^{(d)}(W, I)$ are band-limited to $W = [-v_{\mathrm{Dmax}}, v_{\mathrm{Dmax}}]$.
- The eigenvalues $\lambda_d(W, I)$ of the DPS sequence $v_m^{(d)}(W, I)$ denotes the energy concentration of the sequence within I,

$$\lambda_d(W, I) = \frac{\sum_{m \in I} |v_m^{(d)}(W, I)|^2}{\sum_{m \in \mathbb{Z}} |v_m^{(d)}(W, I)|^2}. \tag{3.15}$$

- The eigenvalues $\lambda_d(W, I)$ satisfy $0 < \lambda_d(W, I) < 1$. They are clustered around 1 for $d \leq D' - 1$, and decay exponentially for $d \geq D'$, where $D' = \lceil |W||I| \rceil + 1 = \lceil 2v_{\mathrm{Dmax}} M \rceil + 1$.
- The DPS sequences $v_m^{(d)}(W, I)$ are orthogonal not only on the Euclidean space $\mathbb{Z}$, but also on the index set I.
- Every band-limited sequence g_m can be decomposed uniquely as $g_m = g'_m + g''_m$, where g'_m is a linear combination of DPS sequences $v_m^{(d)}(W, I)$ for some I and $g''_m = 0$ for all $m \in I$.

Multidimensional DPS sequences are a generalization of the original one-dimensional DPS sequences to many dimensions [85]. This generalization is straightforward. The discrete sequences $v_{\boldsymbol{m}}$, defined on the Euclidean space $\mathbb{Z}^N$ of N dimensions, we are looking for, shall have their maximum energy concentration on the index set $I \subset \mathbb{Z}^N$, i.e.,

$$\lambda = \frac{\sum_{\boldsymbol{m} \in I} |v_{\boldsymbol{m}}|^2}{\sum_{\boldsymbol{m} \in \mathbb{Z}^N} |v_{\boldsymbol{m}}|^2}. \tag{3.16}$$

When $v_{\boldsymbol{m}}$ is bandlimited to W, where $W \subset \mathbb{R}^N$, so that

$$v_{\boldsymbol{m}} = \int_W V(\boldsymbol{f}) e^{2\pi j \langle \boldsymbol{f}, \boldsymbol{m} \rangle} d\boldsymbol{f}, \quad \boldsymbol{m} \in \mathbb{Z}^N, \tag{3.17}$$

where

$$V(\boldsymbol{f}) = \sum_{\boldsymbol{m} \in \mathbb{Z}^N} v_{\boldsymbol{m}} e^{-2\pi j \langle \boldsymbol{f}, \boldsymbol{m} \rangle}, \quad \boldsymbol{f} \in \mathbb{R}^N. \tag{3.18}$$

Define $I \subset \mathbb{Z}^N$ as a $N-$dimensional finite index set with $L = |I|$ elements, and $W \subset (-1/2, 1/2)^N$ as a $N-$dimensional band-limit region. The multidimensional DPS sequences $v_{\boldsymbol{m}}^{(d)}(W, I)$ are defined as the solutions of the eigenvalue problem [84]

$$\sum_{\boldsymbol{m'} \in I} v_{\boldsymbol{m'}}^{(d)}(W, I) K^{(W)}(\boldsymbol{m'} - \boldsymbol{m}) = \lambda_d(W, I) v_{\boldsymbol{m}}^{(d)}(W, I), \tag{3.19}$$

where

$$K^{(W)}(\boldsymbol{m'} - \boldsymbol{m}) = \int_W e^{2\pi j \langle \boldsymbol{f''}, \boldsymbol{m'} - \boldsymbol{m} \rangle} d\boldsymbol{f''}. \tag{3.20}$$

They are sorted such that their eigenvalues $\lambda_d(W, I)$ are in descending order as

$$\lambda_0(W, I) > \lambda_1(W, I) > \cdots > \lambda_{L-1}(W, I). \tag{3.21}$$

The DPS vector $\boldsymbol{v}^d(W, I) \in \mathbb{C}^L$ is defined as the multidimensional DPS sequence $v_m^{(d)}(W, I)$ index-limited to I. Let index every element $\boldsymbol{m} \in I$ lexicographically as $I = \{\boldsymbol{m}_l, l = 0, 1, \ldots, L-1\}$, then

$$\boldsymbol{v}^{(d)}(W, I) = [v_{\boldsymbol{m}_0}^{(d)}(W, I), v_{\boldsymbol{m}_1}^{(d)}(W, I), \ldots, v_{\boldsymbol{m}_{L-1}}^{(d)}(W, I)]^{\mathrm{T}}, \tag{3.22}$$

where $[\cdot]^{\mathrm{T}}$ denotes the transpose function. We define a matrix $\boldsymbol{K}^{(W)}$ with elements

$$K_{k,l}^{(W)} = K^{(W)}(\boldsymbol{m}_k - \boldsymbol{m}_l), \quad k, l = 0, 1, \ldots, L-1, \tag{3.23}$$

where the kernel $K^{(W)}$ is given by (3.20). The multidimensional DPS vectors $\boldsymbol{v}^{(d)}(W, I)$ and their corresponding eigenvalues $\lambda_d(W, I)$ can be denoted as the eigenvectors and eigenvalues of $\boldsymbol{K}^{(W)}$, so that [84]

$$\boldsymbol{K}^{(W)} \boldsymbol{v}^{(d)}(W, I) = \lambda_d(W, I) \boldsymbol{v}^{(d)}(W, I). \tag{3.24}$$

Lets write W and I as a Cartesian product of one-dimensional intervals as [84]

$$W = W_0 \times \cdots \times W_{N-1}, \tag{3.25}$$

and

$$I = I_0 \times \cdots \times I_{N-1}, \tag{3.26}$$

where $W_i = [W_{0,i} - W_{\max,i}, W_{0,i} + W_{\max,i}]$ and $I_i = \{M_{0,i}, \ldots, M_{0,i} + M_i - 1\}$, respectively. Then the kernel $K^{(W)}$ can be written as [84]

$$K^{(W)}(\boldsymbol{u}) = \prod_{i=0}^{N-1} K^{(W_i)}(u_i), \tag{3.27}$$

where $\boldsymbol{u} = [u_0, \ldots, u_{N-1}]^{\mathrm{T}} \in I$. Due to (3.25) and (3.26), K^W is separable and the covariance matrix can be expressed as Kronecker product

$$\boldsymbol{K}^{(W)} = \boldsymbol{K}^{(W_0)} \otimes \cdots \otimes \boldsymbol{K}^{(W_{N-1})}, \tag{3.28}$$

where $\boldsymbol{K}^{(W_i)}$ is the kernel matrix corresponding to the one-dimensional DPS vector and $\otimes$ denotes the Kronecker product. The eigenvalues and eigenvectors of $\boldsymbol{K}^{(W_i)}$ are denoted by $\lambda_{d_i}(W_i, I_i)$ and $\boldsymbol{v}^{(d_i)}$, respectively, where $d_i = 0, \ldots, M_i - 1$ and $i = 0, \ldots, N-1$. The eigenvalues of $\boldsymbol{K}^{(W)}$ are given by [84]

$$\lambda_{\boldsymbol{d}}(W, I) = \lambda_{d_0}(W_0, I_0) \cdots \lambda_{d_{N-1}}(W_{N-1}, I_{N-1}). \tag{3.29}$$

and the corresponding eigenvectors are given by

$$\boldsymbol{v}^{(\boldsymbol{d})}(W, I) = \boldsymbol{v}^{(d_0)}(W_0, I_0) \otimes \cdots \otimes \boldsymbol{v}^{(d_{N-1})}(W_{N-1}, I_{N-1}), \tag{3.30}$$

where $\boldsymbol{d} = [d_0, \ldots, d_{N-1}]^{\mathrm{T}} \in I$. The multidimensional DPS vectors $\boldsymbol{v}^{(d)}(W, I)$ are obtained by reordering eigenvectors $\boldsymbol{v}^{(\boldsymbol{d})}(W, I)$ according to the descending order of the eigenvalues $\lambda_{(\boldsymbol{d})}(W, I)$.

All the properties for one-dimensional DPS sequences are also applicable to multidimensional DPS sequences [84]. The only difference is that $m \in \mathbb{Z}$ should be replaced by $\boldsymbol{m} \in \mathbb{Z}^N$.

3.3.2 Channel Frequency Response of RT

For a static Tx and a mobile Rx, the CIR becomes time-variant. More precisely, the channel is dependent on the Rx position $\boldsymbol{x}$, whose relation with time t can be given as $\boldsymbol{x}(t) = \boldsymbol{x}_0 + \boldsymbol{v}_{\mathrm{Rx}} t$, where $\boldsymbol{x}_0$ is the initial position of the Rx when it starts moving, and $\boldsymbol{v}_{\mathrm{Rx}}$ is the velocity vector of the Rx. Therefore, we use $H(f, \boldsymbol{x}(t))$ to express the time-variant channel frequency response. In wireless communications, the signal arriving at the Rx usually consists of several multipath components, each of which is arising from the interaction of the transmitted signal with the surrounding environment. Thus, the time-variant frequency response of RT $H_{\mathrm{RT}}(f, \boldsymbol{x}(t))$ can be seen as a superposition of all propagation paths contributions, which can be calculated as

$$H_{\mathrm{RT}}(f, \boldsymbol{x}(t)) = \sum_{l=1}^{L} \eta_l(\boldsymbol{x}(t)) e^{-j2\pi f \tau_l(\boldsymbol{x}(t))}, \tag{3.31}$$

where l is the propagation path index, $\eta_l(\boldsymbol{x}(t))$ is the complex-valued weighting coefficient of the $l-$th path, $\tau_l(\boldsymbol{x}(t))$ is the delay, and L is the total number of paths. Both $\eta_l(\boldsymbol{x}(t))$ and $\tau_l(\boldsymbol{x}(t))$ depend on the Rx position $\boldsymbol{x}(t)$. Based on the sampling rate in time $1/T_\mathrm{S}$, the sampled position vector of the Rx can be expressed as $\boldsymbol{x}[m] = \boldsymbol{x}_0 + \boldsymbol{v}_\mathrm{Rx} T_\mathrm{S} m$, where $m \in \{0, \ldots, M-1\}$ denotes the discrete time index and M is the number of samples in the time domain, respectively. With the sampling rate in distance $\boldsymbol{x}_\mathrm{S} = \boldsymbol{v}_\mathrm{Rx} T_\mathrm{S}$ we can express the sampled time-variant frequency response as

$$H_\mathrm{RT}[q, m] = H_\mathrm{RT}(q f_\mathrm{S}, \boldsymbol{x}_0 + m\boldsymbol{x}_\mathrm{S}) = \sum_{l=1}^{L} \eta_l[m] e^{-j2\pi q \theta_l[m]}, \tag{3.32}$$

where $q \in \{-\lfloor \frac{Q}{2} \rfloor, \ldots, \lfloor \frac{Q}{2} \rfloor - 1\}$ is the discrete frequency index, $f_\mathrm{S} = B/Q$ denotes the width of a frequency bin, B denotes bandwidth, Q is the number of samples in the frequency domain, and $\theta_l[m] = \tau_l[m] f_\mathrm{S}$ is the normalized delay of the $l-$th path at time m.

3.3.2.1 Specular Components

The specular components refer to reflection, penetration and diffraction contributions. The geometrical relationships between the incidence and the reflected/penetrated/diffracted rays are based on optical principle described in Chapter 2. Therefore, the complex-valued weighting coefficient $\eta_l[m]$ of the $l-$th single specular contribution at time m can be calculated.

3.3.2.2 Diffuse Scattering with Correlation in Space

We are extending the presented diffuse scattering algorithm to allow for correlated diffuse scattering which is relevant to simulate the movement of the Rx during the transmission of a single data frame $|\boldsymbol{x}[M-1] - \boldsymbol{x}_0| \leq \kappa\lambda$, where $\kappa \leq 1$, and λ is the wavelength. The diffuse scattering components can be assumed correlated in time/space for this short distance [16]. It should be mentioned that we set $\kappa = 1$ at first and the value of κ will be finally defined by the mean square error (MSE) threshold described in Section 3.3.4.

We define the Rx moving distance $\kappa\lambda$ as one simulation set, then RT should redraw the diffuse scattering components independently for another set. In the following we present the extended diffuse scattering algorithm for RT that enables the calculation of correlated realizations in one simulation set:

- The original subdivision algorithm based on the far-field condition is applied to obtain multiple diffuse tiles. A diffuse scattering path is supposed to arise

from the center of each tile. The size of each tile is evaluated by recursively dividing the surface until the far-field condition

$$d_{\max,\ell} < \sqrt{\frac{d_{\mathrm{s},\ell}[0]\lambda}{2}}, \tag{3.33}$$

is fulfilled, where ℓ is the surface tile index, $d_{\max,\ell}$ is the maximum size of the $\ell-$th surface tile and $d_{\mathrm{s},\ell[0]}$ is the distance between the center of the $\ell-$th surface tile and the Tx for the single bounce scattering case. Since the Tx is static, the tiling of the surface for the duration $m \in \{0, \ldots, M-1\}$ is fixed.

- The directive pattern model is used to evaluate the amplitude of each diffuse scattering path, which assumes that the scattering lobe is steered towards the direction of the specular reflection, as described in Section 2.5. According to (2.43), the amplitude of a diffuse scattering path $|\eta_\ell[m]|$ at time m can be computed as

$$|\eta_\ell[m]|^2 = |\eta_{\ell_0}[m]|^2 \cdot \Big(\frac{1+\cos(\Psi_{\mathrm{R},\ell}[m])}{2}\Big)^{\alpha_\mathrm{R}}, \tag{3.34}$$

where $|\eta_{\ell_0}[m]|$ is the maximum amplitude related to the $\ell-$th scattering lobe, and $\Psi_{\mathrm{R},\ell}[m]$ is the angle between the $\ell-$th scattering wave and the reflection wave directions.

- The complex-valued scattered weighting coefficient can be written as

$$\eta_\ell[m] = |\eta_\ell[m]|e^{-j\theta_{\mathrm{ds},\ell}}, \tag{3.35}$$

where $\theta_{\mathrm{ds},\ell}$ is the random phase associated with the $\ell-$th diffuse scattering path with an uniform distribution in $[0, 2\pi]$. The random phase $\theta_{\mathrm{ds},\ell}$ is chosen at $m = 0$ and kept fixed for the duration $m \in \{0, \ldots, M-1\}$.

3.3.3 Complexity Reduction

Indoor environments with diffuse scattering require the calculation of a high number of propagation paths for RT. Hence there is a strong need to reduce the complexity of RT in order to enable its application to time and frequency selective channels. A two step approach is used to achieve this goal in my thesis.

3.3.3.1 First Step: Sum of Complex Exponentials Channel Model

The geometrical calculation of all propagation paths have a significant impact on the complexity of RT in a time-variant indoor environment for a moving Rx. In the case

of $\kappa \leq 1$, it is sufficient to perform RT at the starting position $\boldsymbol{x}_0$ of the Rx. For the remaining linear movement distance $\boldsymbol{x}[m] = \boldsymbol{x}_0 + m\boldsymbol{x}_\mathrm{S}$, during the transmission in the simulated time $m \in \{0, \ldots, M-1\}$ and frequency range $f \in [f_\mathrm{c} - B/2, f_\mathrm{c} + B/2]$, the channel is assumed to be wide sense stationary. Therefore, we can utilize the sum of complex exponentials (SoCE) channel model [86] to reduce the numerical complexity. The sampled time-variant frequency response can be expressed as

$$H_\mathrm{SoCE}[q, m] = \sum_{l=1}^{L} \eta_l[0] e^{-j2\pi q \theta_l[0]} e^{j2\pi m \nu_l[0]}, \tag{3.36}$$

where $\eta_l[0]$, $\theta_l[0]$ and $\nu_l[0] = \omega_l[0] T_\mathrm{S}$ are the complex-valued weighting coefficient, normalized delay and normalized Doppler shift of the $l-$th path at the Rx position $\boldsymbol{x}_0$. The Doppler shift ω_l at the center frequency f_c is given as $\omega_l[0] = f_\mathrm{c}(|\boldsymbol{v}_\mathrm{Rx}| \cos(\phi_l[0]))/c$, where c is the speed of light and $\phi_l[0]$ is the angle of arrival of the $l-$th path.

3.3.3.2 Second Step: DPS Subspace Channel Model

We exploit the band-limited property of the channel frequency response projecting each path $l \in \{1, \ldots, L\}$ on a subspace spanned by two-dimensional DPS sequences [81]. To design the DPS subspace we need two key parameters:

- the maximum normalized Doppler shift $\nu_\mathrm{Dmax} = \omega_\mathrm{max} T_\mathrm{S}$, where ω_max is the maximum Doppler shift, and
- the maximum normalized delay $\theta_\mathrm{Dmax} = \tau_\mathrm{max} f_\mathrm{S}$, where τ_max is the maximum delay.

The band-limit region is defined by the Cartesian product $W = W_t \times W_f = [-\nu_\mathrm{Dmax}, \nu_\mathrm{Dmax}] \times [0, \theta_\mathrm{Dmax}]$. It is our interest to compute the channel response for a certain number of time stamps and frequency bins. We denote this index set as $I = I_t \times I_f = \{0, \ldots, M-1\} \times \{-\lfloor \frac{Q}{2} \rfloor, \ldots, \lfloor \frac{Q}{2} \rfloor - 1\}$.

The two-dimensional DPS subspace representation $\boldsymbol{H}_\mathrm{DPS}^{(D)}$ with the essential subspace dimension D, can be expressed as [84]

$$\boldsymbol{H}_\mathrm{DPS}^{(D)} = \boldsymbol{V}\boldsymbol{\alpha}, \tag{3.37}$$

where the matrix

$$\boldsymbol{V} = [\boldsymbol{v}^{(0)}(W, I), \ldots, \boldsymbol{v}^{(D-1)}(W, I)], \tag{3.38}$$

in which $\boldsymbol{v}^{(d)}(W, I)$ are the multidimensional DPS vectors for the multidimensional band-limit region W and the multidimensional index set I. And basis coefficients vector $\boldsymbol{\alpha}$ is the projection of the vector $\boldsymbol{H}_{\mathrm{DPS}}$ onto the column of $\boldsymbol{V}$ as

$$\boldsymbol{\alpha} = \boldsymbol{V}^{\mathrm{H}} \boldsymbol{H}_{\mathrm{DPS}}, \tag{3.39}$$

where $[\cdot]^{\mathrm{H}}$ denotes the conjugate transpose function.

The square bias of the multidimensional DPS subspace representation is defined as

$$\mathrm{bias}^2_{\boldsymbol{H}^{(D)}_{\mathrm{DPS}}} = \frac{1}{|I||W|} \sum_{d=D}^{|I|-1} \lambda_d(W, I). \tag{3.40}$$

According to the requirement that the bias of the subspace representation is small compared to the machine precision $E_{\max}$ of the underlying simulation hardware, the subspace dimension D should be chosen as

$$D = \arg\min_{D} \mathrm{bias}^2_{\boldsymbol{H}^{(D)}_{\mathrm{DPS}}} \leq E^2_{\max}. \tag{3.41}$$

An estimate D can be obtained by estimating the subspace dimension D_i of the corresponding one-dimensional DPS subspace representation. Please note that $D \leq D_0 \ldots D_{N-1}$, where $N = 2$ for our case.

In order to reduce the complexity of calculating (3.39), approximated basis coefficients $\tilde{\boldsymbol{\alpha}}$ are used. The approximate two-dimensional DPS subspace representation $\tilde{\boldsymbol{H}}^{(D)}_{\mathrm{DPS}}$ with the subspace dimension D, whose element can be expressed as [84]

$$\tilde{H}^{(D)}_{\mathrm{DPS}}[q, m] \approx \boldsymbol{V}\tilde{\boldsymbol{\alpha}}, \tag{3.42}$$

where the two-dimensional DPS basis vectors are

$$\boldsymbol{V} = \boldsymbol{V}(W, I) = \boldsymbol{V}(W_t, I_t) \diamond \boldsymbol{V}(W_f, I_f). \tag{3.43}$$

The matrices $\boldsymbol{V}(W_t, I_t)$ and $\boldsymbol{V}(W_f, I_f)$ contain the one-dimensional DPS vectors $\boldsymbol{v}^{(d_0)}(W_t, I_t)$ and $\boldsymbol{v}^{(d_1)}(W_f, I_f)$ in their columns, respectively. The operator $\diamond$ is the Tracy-Singh product of column-wise partitioned matrices [87]. $\boldsymbol{V}(W_t, I_t)$ and $\boldsymbol{V}(W_f, I_f)$ have the essential subspace dimensions D_0 and D_1 in space/time and frequency, respectively. The approximated basis coefficients are represented as

$$\tilde{\boldsymbol{\alpha}} = \sum_{l=0}^{L-1} \eta_l[0](\underbrace{(\boldsymbol{V}(W_t, I_t)\boldsymbol{\chi}_t(\nu_l))}_{\boldsymbol{\gamma}^t_{d_0,l} : \approx \tilde{\boldsymbol{\gamma}}^t_{d_0,l}(\nu_l; W_t, I_t)} \otimes \underbrace{(\boldsymbol{V}(W_f, I_f)\boldsymbol{\chi}_f(\theta_l))}_{\boldsymbol{\gamma}^f_{d_1,l} : \approx \tilde{\boldsymbol{\gamma}}^f_{d_1,l}(\theta_l; W_f, I_f)}), \tag{3.44}$$

where the complex exponential functions $\boldsymbol{\chi}_t(\nu_l)$ and $\boldsymbol{\chi}_f(\theta_l)$ are given as

$$\boldsymbol{\chi}_t(\nu_l) = [\vartheta_t^0, \vartheta_t^1, \ldots, \vartheta_t^{(M-1)}]^{\mathrm{T}}, \tag{3.45}$$

and

$$\boldsymbol{\chi}_f(\theta_l) = [\vartheta_f^{(-\lfloor \frac{Q}{2} \rfloor)}, \vartheta_f^{(-\lfloor \frac{Q}{2} \rfloor+1)}, \ldots, \vartheta_f^{(\lfloor \frac{Q}{2} \rfloor-1)}]^{\mathrm{T}}, \tag{3.46}$$

where $\vartheta_t = e^{j2\pi\nu_l[0]}$ and $\vartheta_f = e^{-j2\pi\theta_l[0]}$. $\tilde{\boldsymbol{\gamma}}^t_{d_0,l}(\nu_l; W_t, I_t)$ and $\tilde{\boldsymbol{\gamma}}^f_{d_1,l}(\theta_l; W_f, I_f)$ are the one-dimensional approximated projections of the complex exponential functions on the DPS basis vectors in time and frequency dimensions, which can be calculated by the scaled and shifted approximated DPS wave functions $\tilde{U}_{d_0}(\nu_l; W_t, I_t)$ and $\tilde{U}_{d_1}(\theta_l; W_f, I_f)$, respectively [84]. Take $\tilde{\boldsymbol{\gamma}}^t_{d_0,l}(\nu_l; W_t, I_t)$ as an example

$$\tilde{\boldsymbol{\gamma}}^t_{d_0,l}(\nu_l; W_t, I_t) := \frac{1}{\epsilon_{d_0}} e^{j\pi(2M_0+M-1)\nu_l} \tilde{U}_{d_0}(\nu_l; W_t, I_t), \tag{3.47}$$

where $\epsilon_{d_0} = 1$ if d_0 is even, $\epsilon_{d_0} = j$ if d_0 is odd, and

$$\tilde{U}_{d_0}(\nu_l; W_t, I_t) := \pm e^{2\pi j(M_0+M-1+m_l)W_0} \sqrt{\frac{\lambda_{d_0} M}{2W_{\max}} v_{m_l}^{(d_0)}(W_t, I_t)}. \tag{3.48}$$

Define $v_m^{(d_0)}$ as DPS sequences with band-limit region W_t and index set I_t, and λ_{d_0} is the corresponding eigenvalues, then the index m_l is defined as

$$m_l = \lfloor (1 + \frac{\nu_l - W_0}{W_{\max}}) \frac{M}{2} \rfloor. \tag{3.49}$$

The sign in (3.48) is taken such that the following normalization holds:

$$\tilde{U}_{d_0}(W_0; W_t, I_t) \geq 0, \quad \frac{d\tilde{U}_{d_0}(\nu_l; W_t, I_t)}{d\nu_l}|_{\nu_l = W_0} \geq 0, \tag{3.50}$$

where $d_0 = 0, \ldots, D_0 - 1$. In our case, $M_0 = 0$, $W_0 = 0$ and $W_{\max} = \nu_{\mathrm{Dmax}}$ here. Using a similar method, $\tilde{U}_{d_1}(\theta_l; W_f, I_f)$ can be also obtained.

The computation time of the DPS subspace channel model needs to consider the simulation time T_{RT} of an initial RT result. The runtime of RT at each $m \in \{1, \ldots, M-1\}$ is almost the same as the runtime at $m = 0$, the approximated computation effort of the DPS subspace channel model can be given as

$$\frac{MT_{\mathrm{RT}}}{T_{\mathrm{RT}} + T_{\mathrm{DPS}}} < M, \tag{3.51}$$

where T_{DPS} is the runtime of the DPS algorithm without the computation of an initial RT result. The details about T_{DPS} are described in [84]. The computational complexity reduction factor of the DPS method is bounded by the number of time samples M.

3.3.4 Simulation Procedure

RT depends on a full description of the scenario to be simulated. In order to show the performance of the proposed RT channel model, a time-variant indoor scenario is generated. The simulated indoor scenario is shown in Fig. 3.12. Compared with the scenario shown in Fig. 3.5, the only difference is that one block at the far left side is missing. The values of relative permittivity and the conductivity of the materials involved in the simulated scenario are the same as in Section 3.2.2. The Tx and the Rx antennas used for the simulation are dipole antennas with length $\lambda/2$. The Rx antenna is linearly moving with a constant speed and along a constant direction.

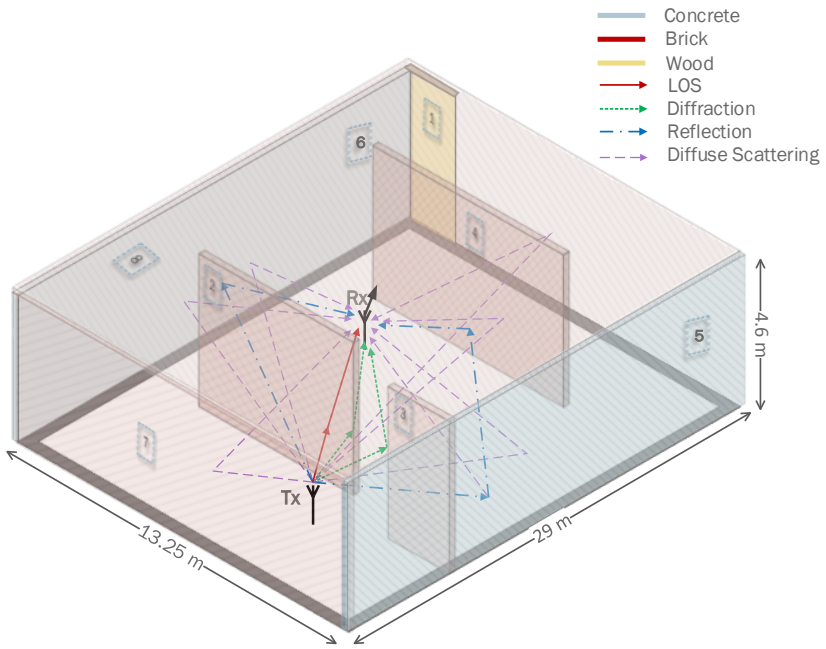

Figure 3.12: Indoor time-variant scenario with a static Tx and a mobile Rx. Each block is indexed by a number here.

We take into account LOS, reflection up to the third-order, single-order diffraction and single bounce scattering. Note that the penetration case is embedded into all other contributions. The visualization of some propagation paths is also shown in Fig. 3.12. There are more than $L = 3.4 \times 10^3$ paths to be calculated at one time m. Firstly, we set $\kappa = 1$, hence the Rx moves one wavelength. Initial simulation parameters are summarized in Table 3.2.

Table 3.2: Initial Simulation Parameters

Parameter	Value
Carrier frequency f_c	2.45 GHz
Bandwidth B	240 MHz
Rx velocity $\lvert\boldsymbol{v}_{\mathrm{Rx}}\rvert$	3 km/h
Sampling rate in distance $\lvert\boldsymbol{x}_{\mathrm{S}}\rvert$	0.0012 m
Number of time samples M	100
Width of frequency bin f_{S}	500 KHz
Number of frequency bin Q	480

The MSE between RT and the SoCE channel model can be calculated as (3.52) [88]

$$err(\boldsymbol{x}(t)) = \frac{\int |H_{\mathrm{RT}}(f, \boldsymbol{x}(t)) - H_{\mathrm{SoCE}}(f, \boldsymbol{x}(t))|^2 df}{\int |H_{\mathrm{RT}}(f, \boldsymbol{x}(t))|^2 df}. \tag{3.52}$$

The associated result is shown in Fig. 3.13. By setting the error threshold $err_{\mathrm{thr}} = -20\,\mathrm{dB}$, the corresponding moving distance of the Rx is $|\boldsymbol{x}_{\mathrm{thr}}| = 0.25\lambda$, which is equivalent to 0.03 m. Therefore, we finally define $\kappa = 0.25$. Furthermore, keeping $|\boldsymbol{x}_{\mathrm{S}}|$ fixed, the number of time samples $M = 25$ for the remaining of this section.

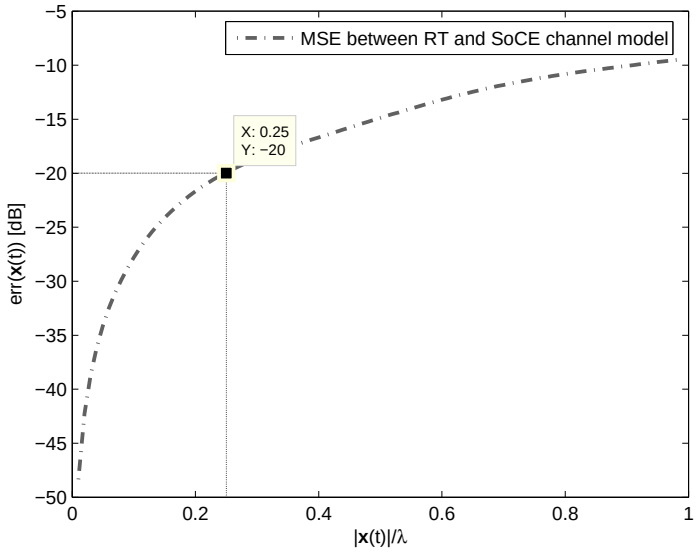

Figure 3.13: MSE between RT and SoCE channel model. The moving distance of Rx is one wavelength. The error threshold is set as −20 dB.

Within the threshold region, the Rx moving distance is finally clarified as one-quarter wavelength. The approximation errors among RT, SoCE and DPS subspace

channel models, which can be calculated similarly to (3.52), are shown in Fig. 3.14. It can be noticed that the maximum MSE of the low-complexity DPS subspace channel model is more than 40 dB below the power of the SoCE channel response. Meanwhile the MSE between RT and DPS subspace channel model is smaller than the error threshold err_{thr}.

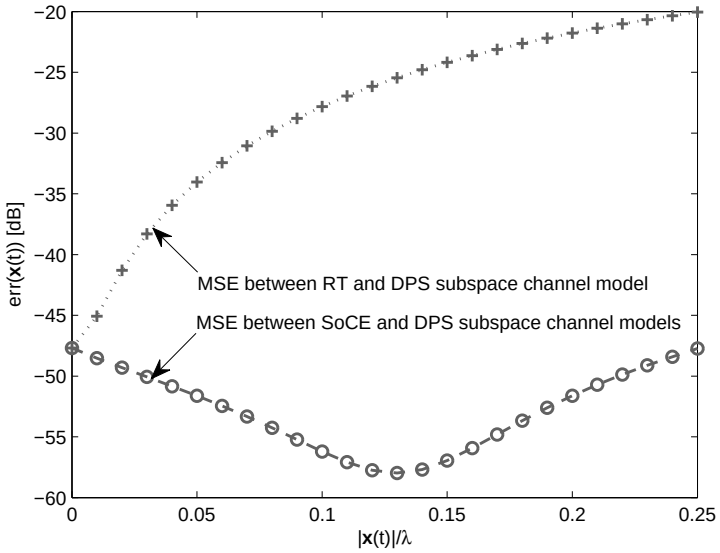

Figure 3.14: MSE among RT, SoCE and DPS subspace channel models. The moving distance of Rx is one-quarter wavelength.

The numerical complexity for the simulated channels is significantly reduced with a negligible approximation error. Considering the same time-variant indoor scenario, where the Rx moves about one-quarter wavelength within $M = 25$ time samples, the RT runs about 555.10 s, while the DPS subspace channel model requires roughly 9.30 s plus the simulation time of the initial RT result of 24.46 s. Fig. 3.15 presents the simulation time comparison between the RT and DPS subspace channel model within different number of blocks N_{b} in the indoor scenario. It is obvious that a scenario with more objects, modeled as rectangular blocks, leads to an increase in the number of propagation paths and the simulation time of RT. According to (3.51), the computational complexity reduction factor of the DPS method is bound by the number of time samples $M = 25$. When there are 4 and 8 blocks in the scenario, the complexity reduction factors achieved by the DPS subspace channel model are 2 and 16, respectively. The computational complexity reduction achieved by the DPS method increases with the number of propagation paths when the number of time samples M is fixed. It can be seen that the simulation time of the DPS method

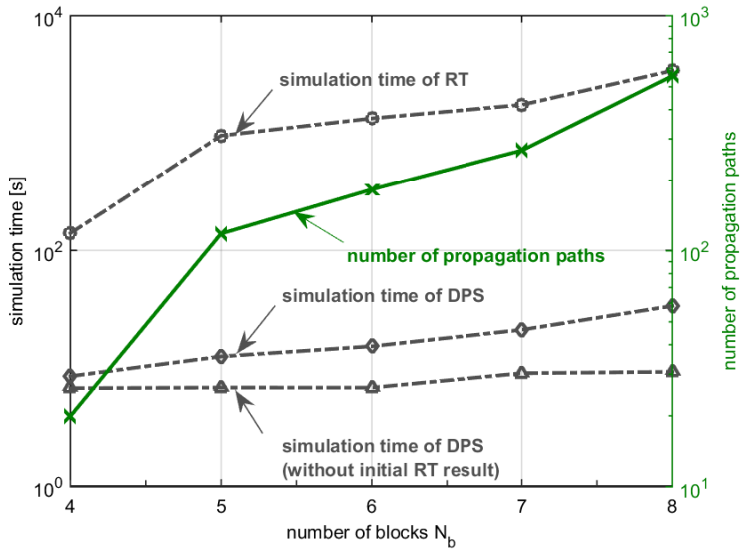

Figure 3.15: Simulation time comparison according to different number of blocks in the scenario: RT and DPS. N_b is corresponding to the first indexed N_b blocks in Fig. 3.12. Rx moves about one-quarter wavelength within $M = 25$ time samples.

Table 3.3: DPS Parameters

DPS Parameter	Value
Maximum norm. Doppler ν_{Dmax}	0.01
Subspace dimension D_0	4
Maximum norm. delay θ_{Dmax}	0.13
Subspace dimension D_1	131

without the computation of an initial RT result does not change much with the increasing number of propagation paths. The runtime comparison shown in Fig. 3.15 also correlates nicely with exact result presented in [84]. The parameters of the DPS sequences with $N_\mathrm{b} = 8$ blocks in the scenario are summarized in Table 3.3. It is evident that the subspace dimensions are much smaller than the number of propagation paths.

4 Ray Tracing for UWB Indoor Scenarios

UWB technology has attracted a lot of interest in recent years as an candidate for short-range and broadband indoor wireless communication systems. It offers major enhancement specially for the localization and tracking in indoor environments. UWB systems enable a fine delay resolution of the multipath components of the received signal [89,90]. The achieved accuracy of localization methods based on the radio signal is strongly affected by the propagation channel. Therefore, it is crucial to understand the UWB channel properties. Two main categories of channel modeling techniques for UWB channels exist [91]: one is the statistical modeling based on frequency or time domain measurements, the other is deterministic modeling based on a scenario map. So far, SDRT has been frequently employed as the typical deterministic channel modeling tool for UWB indoor channels by the superposition of RT results implemented at the individual center frequency of each sub-band [92,93].

However, the computational complexity is directly proportional to the number of sub-bands. In order to significantly reduce the computational complexity of SDRT, a low-complexity SDRT is firstly proposed in this chapter. Our proposed RT is independent of the number of sub-bands. Based on the low-complexity SDRT implementation, a multiobjective calibration approach is introduced to estimate the optimal material parameters. The approach can improve the accuracy of SDRT in terms of the PDP and RMS delay spread. In addition, for simulating the radio propagation conditions for a mobile terminal in UWB indoor scenarios, a SDRT algorithm based on two-dimensional DPS sequences is proposed.

4.1 Conventional Sub-band Divided RT

A 3D RT tool to calculate all propagation paths connecting the Tx and the Rx is based on geometric and electromagnetic computations. The geometric computations determine the propagation paths interacting with the environment. The electromagnetic computations provide the electric field of the propagation paths in amplitude, phase and polarization according to the considered propagation mechanisms. For

an UWB system, the channel characteristics may vary significantly over the entire bandwidth. To cope with this, the SDRT algorithm applied to UWB radio channels has been introduced in [92, 93]. The basic steps of the method can be summarized as follow:

- The entire UWB bandwidth B is divided into multiple sub-bands $B_i \leq B_{\max}\,\mathrm{MHz}$, where i is the index of the sub-band with $i \in \{1, \cdots, \mathcal{I}\}$, $\mathcal{I}$ is the total number of the sub-bands, and $B_{\max}$ is the maximum sub-band bandwidth. $B_{\max}$ is defined as 500 MHz in our work due to the definition of the UWB system.

- Conventional RT is implemented to obtain the corresponding CIR $h_i(\tau)$ at the center frequency $f_{\mathrm{c},i}$ of each sub-band i, where τ is the propagation path delay.

- The CTF at each sub-band i is obtained by the Fourier transform. Then CTFs of all sub-bands are combined together for the entire bandwidth.

- An inverse Fourier transform yields the overall CIR $h(\tau)$ for the entire bandwidth.

To make this description more clear, we give an example in Fig. 4.1. It is obvious that conventional RT needs to be performed 3 times at the center frequencies of 3 sub-bands, respectively. Thus, the computational complexity of conventional SDRT is directly proportional to the number of sub-bands. It is evident that the computational complexity of RT depends on the number of considered propagation paths. Moreover, it has been experimentally shown that diffuse scattering components are an important factor in determining time and angle dispersion of radio signals in indoor environments [2]. The inclusion of the diffuse scattering mechanism in RT introduces a large number of propagation paths in an indoor environment, which makes the calculation of electromagnetic characteristics extremely time-consuming.

Conventional SDRT simulation obviously makes the computation procedure more complicated. Its computation time is directly proportional to the number of frequency points. Although some simplifications have been made for SDRT by determining the relevant propagation paths once at the beginning of the procedure, the electromagnetic calculation of the received signal still needs to be performed repeatedly at different individual frequency points [88]. Furthermore, extracting the statistics of the channel requires that SDRT simulations must be performed for a large number of positions, which would result in unacceptable long simulation time.

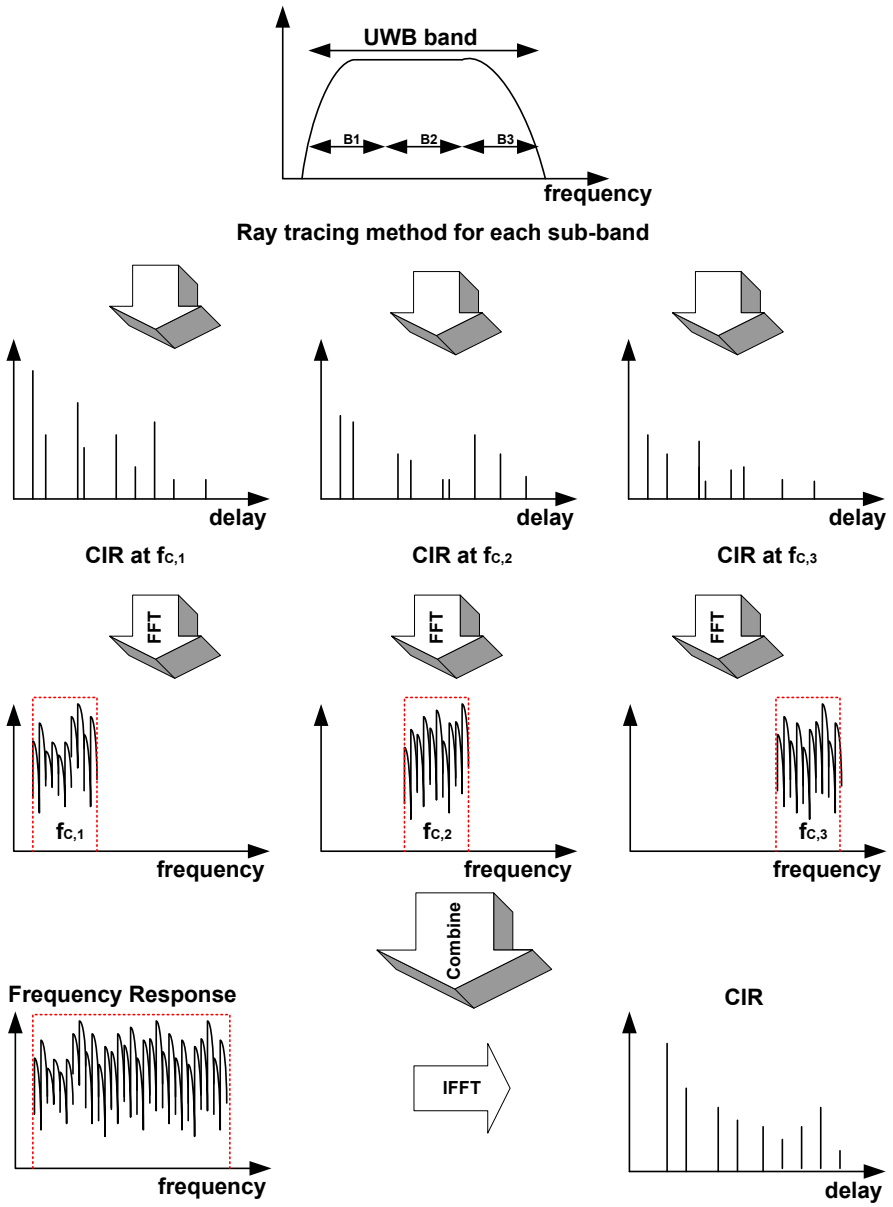

Figure 4.1: Flowchart of the SDRT algorithm, where $\mathcal{I} = 3$.

4.2 Low-Complexity Sub-band Divided RT

In order to significantly improve the computational efficiency of conventional SDRT for UWB indoor systems, we propose a low-complexity SDRT algorithm. The low-complexity SDRT algorithm is derived based on the electromagnetic propagation mechanisms. As a major enhancement, not only the geometric calculation, but also

the electromagnetic calculation needs to be performed only once for all sub-bands. For the diffuse scattering case, we show numerical simulation results to verify that the subdivision of rough surfaces at the center frequency of the entire bandwidth is valid for all sub-bands. Moreover, the accuracy of the proposed low-complexity algorithm is justified by comparing with conventional SDRT. In addition, it can be seen that increasing the number of sub-bands can obtain a slightly higher correlation with the measurement but without noticeable simulation time increase.

To describe the concept more intuitively, the flowchart of the low-complexity SDRT algorithm is given in Fig. 4.2. As in Fig. 4.1, we also select 3 sub-bands here. However, low-complexity RT only needs to be performed once at one sub-band. Then the results at other sub-bands can be derived directly based on the derived mathematical formulas. It is important to note that, based on our approach, both the geometric computation and the electromagnetic calculation need to be performed only once.

4.2.1 Derivation of Low-Complexity SDRT

The CIR at each sub-band i is directly determined by the propagation mechanisms. The LOS component is only affected by the free-space loss, while the specular components are calculated referring to relevant complex dyadic coefficients and the total length of the path. The reflection and penetration coefficients are calculated by the Fresnel formulas [68], whereas the diffraction coefficient is obtained using the UTD [69]. It is assumed that the path direction is not modified by the penetration mechanism in the RT tool. Moreover, it is known that a flat wave is scattered into multiple random directions when it is interacting with a rough surface. A directive scattering pattern model is used in RT to evaluate the amplitude of each diffuse scattering path, which assumes the scattering lobe is steered towards the direction of the specular reflection [2, 50]. The detailed formulas of the propagation mechanisms have been introduced in Chapter 2, from which it is apparent to see which parameters are varying with frequency. Therefore, the electromagnetic calculations $E_{\{\cdot\}}(f_{\mathrm{c},i'})$ at other sub-bands $f_{\mathrm{c},i'}$, where $i' \in \{1, \cdots, \mathcal{I}\}$, for one Rx position can be derived from the electromagnetic results $E_{\{\cdot\}}(f_{\mathrm{c},i})$ of one sub-band $f_{\mathrm{c},i}$. In order to make the formula brief, we ignore the index $\mathbf{P}$ in the expression $E_{\{\cdot\}}$ comparing with the formulas in Chapter 2.

- For the LOS component, the electric field at a different sub-band i' can be

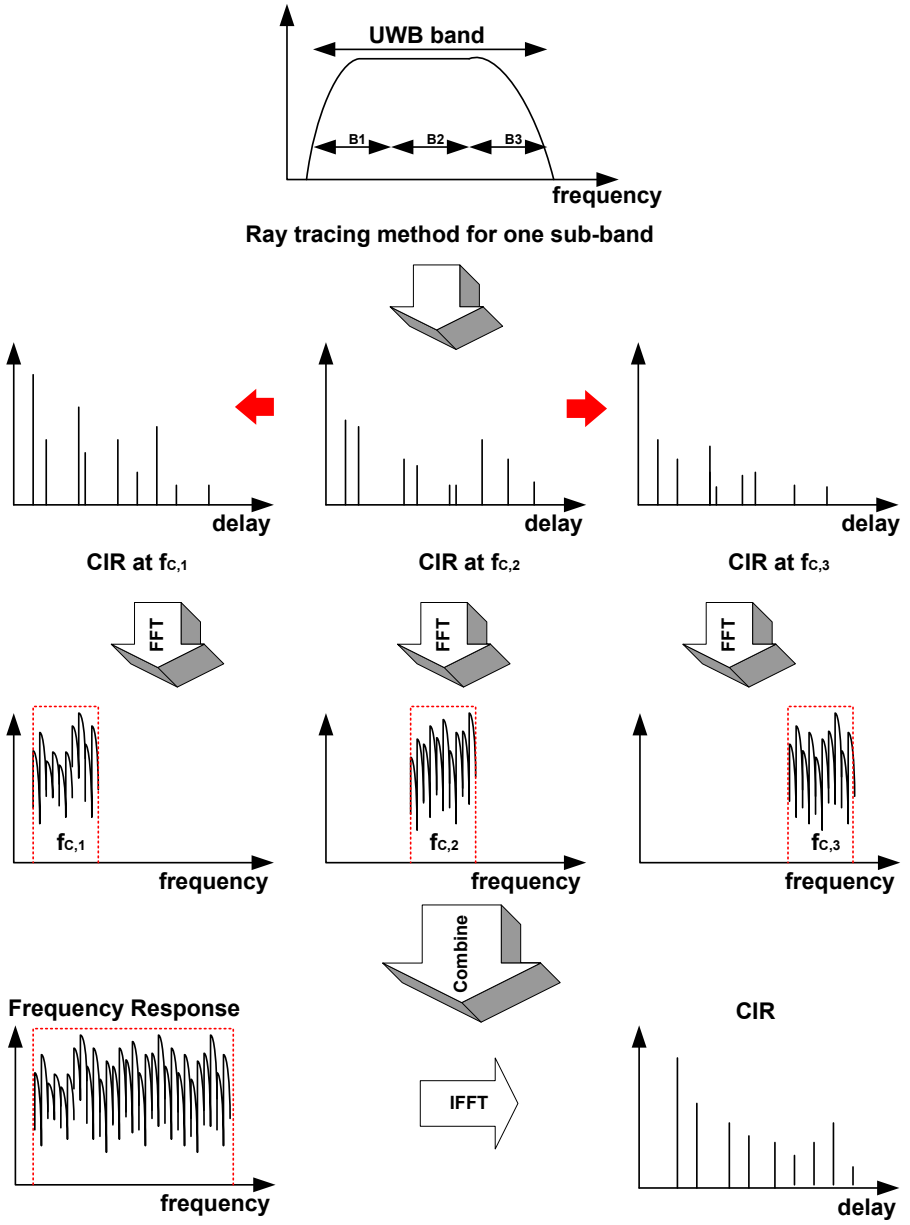

Figure 4.2: Flowchart of the low-complexity SDRT algorithm, where $\mathcal{I} = 3$.

obtained directly

$$E_{\mathrm{LOS}}(f_{\mathrm{c},i'}) = E_{\mathrm{LOS}}(f_{\mathrm{c},i}) \cdot \left[\frac{\bar{g}^{\mathrm{R}}_{\mathrm{LOS}}(f_{\mathrm{c},i'})}{\bar{g}^{\mathrm{R}}_{\mathrm{LOS}}(f_{\mathrm{c},i})}\right]^{*} \cdot \frac{f_{\mathrm{c},i}}{f_{\mathrm{c},i'}} \cdot \left[\frac{\bar{g}^{\mathrm{E}}_{\mathrm{LOS}}(f_{\mathrm{c},i'})}{\bar{g}^{\mathrm{E}}_{\mathrm{LOS}}(f_{\mathrm{c},i})}\right] e^{\frac{-j2\pi(f_{\mathrm{c},i'} - f_{\mathrm{c},i})s_{\mathrm{LOS}}}{c}}, \tag{4.1}$$

where $\bar{g}^{\mathrm{E}}_{\{\cdot\}}(f_{\mathrm{c},\{\cdot\}}) = \bar{g}^{\mathrm{E}}_{\{\cdot\}}(f_{\mathrm{c},\{\cdot\}}, \theta_{\mathrm{E}}, \phi_{\mathrm{E}})$ and $\bar{g}^{\mathrm{R}}_{\{\cdot\}}(f_{\mathrm{c},\{\cdot\}}) = \bar{g}^{\mathrm{R}}_{\{\cdot\}}(f_{\mathrm{c},\{\cdot\}}, \theta_{\mathrm{R}}, \phi_{\mathrm{R}})$ are

complex vectors accounting for the Tx/Rx antenna polarization and amplitude gains within one sub-band in the direction of the propagation wave, and $\theta_{\{.\}}$ and $\phi_{\{.\}}$ indicate the azimuth and the elevation directions of the transmitted/received wave. It is worth mentioning that the geometrical calculation of each propagation path is identical at different sub-bands, so that the corresponding $\theta_{\{.\}}$ and $\phi_{\{.\}}$ of the wave is constant for all sub-bands. In order to simplify the expressions, we omit the arguments $\theta_{\{.\}}$ and $\phi_{\{.\}}$ in the related formulas.

- In [61, 88], it is assumed that the dielectric permittivity ε_r and conductivity σ for one material are independent of the frequencies within the entire bandwidth of interest, because it is difficult to estimate how these values vary with the frequency. However, the effective permittivity of the material

$$\varepsilon_{r,\text{eff}}(f_{\text{c},i}) = \varepsilon_r - j\frac{\sigma}{2\pi f_{\text{c},i}\varepsilon_0}, \tag{4.2}$$

where $\varepsilon_{r,\text{eff}}$ is still varying with frequency. Here we fix the effective permittivity $\varepsilon_{r,\text{eff}}$ for the entire UWB bandwidth. Therefore, the Fresnel reflection/penetration coefficients are independent of frequency, which is justified in the numerical results. As a consequence, the electric field of the reflection/penetration contribution at a different sub-band i' can be computed as

$$\begin{aligned} E_{\text{ref/pen}}(f_{\text{c},i'}) =& E_{\text{ref/pen}}(f_{\text{c},i}) \cdot \left[\frac{\bar{g}^{\text{R}}_{\text{ref/pen}}(f_{\text{c},i'})}{\bar{g}^{\text{R}}_{\text{ref/pen}}(f_{\text{c},i})}\right]^* \cdot \frac{f_{\text{c},i}}{f_{\text{c},i'}} \cdot \\ & \left[\frac{\bar{g}^{\text{E}}_{\text{ref/pen}}(f_{\text{c},i'})}{\bar{g}^{\text{E}}_{\text{ref/pen}}(f_{\text{c},i})}\right] e^{\frac{-j2\pi(f_{\text{c},i'}-f_{\text{c},i})(s_{\text{ref/pen}}+s'_{\text{ref/pen}})}{c}}, \end{aligned} \tag{4.3}$$

where $s_{\text{ref/pen}}$ is the path length from Tx to the reflection/penetration point and $s'_{\text{ref/pen}}$ is the path length from the reflection/penetration point to the Rx.

- For the diffracted contribution, it can be seen in Chapter 2 that the dyadic diffraction coefficients $D^{\perp}_{\parallel}$ are influenced by the frequency. Actually, the dyadic diffraction coefficients can be simplified by ignoring the involved transition functions effect. The reason is that only one of the arguments in the four transition functions is smaller than 10 for one diffraction point, so that only one of the transition values is different from unity [72]. According to (2.24,2.25,2.26,2.27) in Chapter 2, it is acceptable to assume that the value of each transition function in D_1, D_2, D_3 or D_4 is the same for one diffraction

point at different sub-bands. Therefore, the electric field of the diffraction path at a different sub-band i' can be obtained as

$$E_{\mathrm{diff}}(f_{\mathrm{c},i'}) = E_{\mathrm{diff}}(f_{\mathrm{c},i}) \cdot \left[\frac{\bar{g}^{\mathrm{R}}_{\mathrm{diff}}(f_{\mathrm{c},i'})}{\bar{g}^{\mathrm{R}}_{\mathrm{diff}}(f_{\mathrm{c},i})}\right]^{*} \cdot \left(\frac{f_{\mathrm{c},i}}{f_{\mathrm{c},i'}}\right)^{\frac{3}{2}} \cdot \left[\frac{\bar{g}^{\mathrm{E}}_{\mathrm{diff}}(f_{\mathrm{c},i'})}{\bar{g}^{\mathrm{E}}_{\mathrm{diff}}(f_{\mathrm{c},i})}\right] e^{\frac{-j2\pi(f_{\mathrm{c},i'}-f_{\mathrm{c},i})(s_{\mathrm{diff}}+s'_{\mathrm{diff}})}{c}}. \tag{4.4}$$

- A surface appears rougher with increasing frequency, which should result in a denser subdivision of the surface for sub-bands with higher center frequencies. However, this significantly increases the computational effort. In [61], the subdivision of each surface for a specific Rx position at the center frequency of the entire bandwidth is assumed to be valid for all sub-bands. Here it is shown that this assumption is reasonable according to the comparison given in Fig. 4.4 in Section 4.2.2. Thus, the electric field for the scattering path at a different sub-band i' can be calculated as

$$E_{\mathrm{ds}}(f_{\mathrm{c},i'}) = E_{\mathrm{ds}}(f_{\mathrm{c},i}) \cdot \left[\frac{\bar{g}^{\mathrm{R}}_{\mathrm{ds}}(f_{\mathrm{c},i'})}{\bar{g}^{\mathrm{R}}_{\mathrm{ds}}(f_{\mathrm{c},i})}\right]^{*} \cdot \frac{f_{\mathrm{c},i}}{f_{\mathrm{c},i'}} \cdot \left[\frac{\bar{g}^{\mathrm{E}}_{\mathrm{ds}}(f_{\mathrm{c},i'})}{\bar{g}^{\mathrm{E}}_{\mathrm{ds}}(f_{\mathrm{c},i})}\right] e^{-j\theta'_{\mathrm{s}}}, \tag{4.5}$$

  where θ'_{s} is the random phase with an uniform distribution in $[0, 2\pi]$.

It should be noted that the above formulas can also be extended for the multi-order propagation path case by combining the results of corresponding propagation mechanisms.

4.2.2 Measurement Campaign and RT Setup

The accuracy of the proposed low-complexity algorithm is justified by comparing with conventional SDRT and measurements. The scenario used for both SDRT and the measurement campaign is illustrated in Fig. 4.3, which includes both a 3D and a 2D view.

4.2.2.1 Measurement Campaign

Frequency-domain UWB channel measurements were carried out by the Signal Processing and Speech Communication laboratory at Graz University of Technology [94]. The size of the scenario is about 29 m × 7.1 m × 10.5 m. It consists primarily of concrete walls, glass windows and metal pillars. The locations of the Tx antenna was fixed, while the Rx antenna positions formed a grid with 22 × 22 points with 5 cm spacing resulting in a total area of 1m × 1m. A Rhode & Schwarz ZVA-24 vector network analyzer (VNA) was used to measure the CTF at 7501 frequency points over a frequency range from 3.1 to 10.6 GHz.

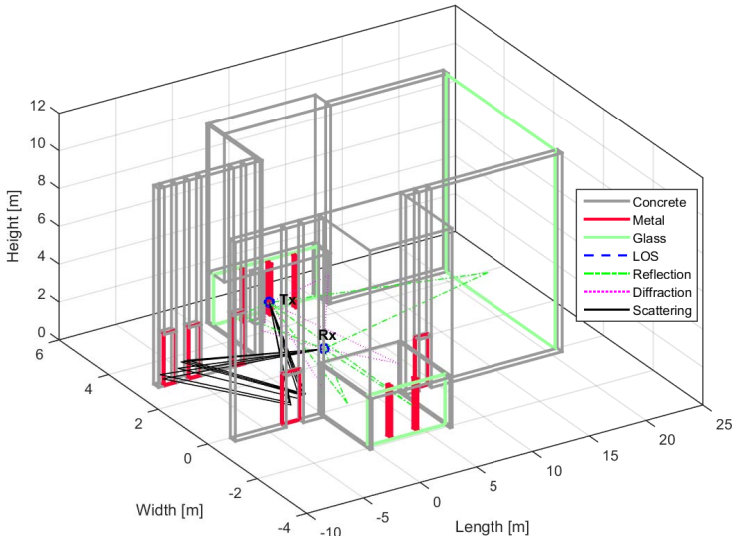

(a) 3D view

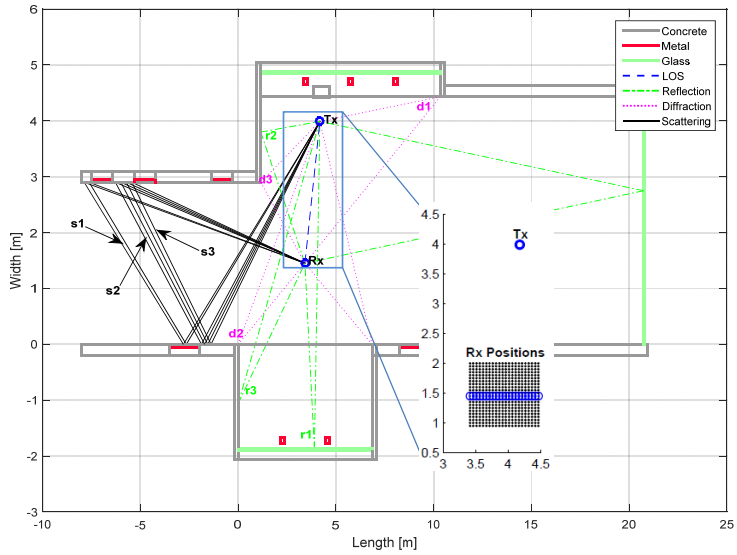

(b) 2D view

Figure 4.3: Pictorial view of the RT scenario considering one Rx position from the grid. (a) 3D view. (b) 2D view, including a close-up view of the grid Rx positions together with the positions marked by the blue line where RT simulations are implemented.

4.2.2.2 RT Setup

The different materials are sketched with different colors in Fig. 4.3. The dielectric properties are also included in the input database of RT, where a metallic block is

considered as a PEC. The values for other materials are: $\varepsilon_r = 6$ and $\sigma = 0.08\,\mathrm{S/m}$ for concrete blocks, and $\varepsilon_r = 5.5$ and $\sigma = 0\,\mathrm{S/m}$ for glass blocks, respectively. The Tx and the Rx antennas used for the RT simulation are dipole antennas corresponding to the antennas used in measurements. RT simulations are implemented at the middle horizontal line of the grid marked in blue in Fig. 4.3 (b). Moreover, the entire bandwidth B of 7.5 GHz is divided into $\mathcal{I} = 15$ sub-bands with $B_i = 500\,\mathrm{MHz}$ each in our simulation.

The involved propagation mechanisms are LOS, reflection up to the third order, penetration, single order diffraction, diffuse scattering, while the penetration contribution has been embedded into all other mechanisms. The diffuse scattering components include single bounce scattering, scattering-reflection and reflection-scattering cases. Some propagation paths are visualized in Fig. 4.3, some of which are indexed by the corresponding number, where **r** indicates the reflection component, **d** means the diffraction component and **s** implies the diffuse scattering component.

Based on our numerical implementation, we compare the PDP of diffuse scattering paths $\mathrm{PDP}_{\mathrm{DS}}$, with different and fixed subdivision of tiles at different sub-bands relying on conventional SDRT. The $\mathrm{PDP}_{\mathrm{DS}}$ is obtained by averaging the normalized CIRs at the selected 22 Rx locations, taking only the diffuse scattering components into account. Note that i) the conventional subdivision algorithm is used here, and ii) $\mathrm{PDP}_{\mathrm{DS}}$ is defined over the excess delay τ_{ex}. The result is shown in Fig. 4.4, from which it can be seen that the $\mathrm{PDP}_{\mathrm{DS}}$ based on the fixed subdivision at 6.85 GHz over the whole bandwidth is similar as the one where the subdivision is changed according to the center frequency of each sub-band. Therefore, (4.5) is a valid approximation for the diffuse scattering case of low-complexity SDRT.

4.2.3 Numerical Results

4.2.3.1 Amplitude and Phase Comparison

The comparison of amplitude and phase of propagation paths based on the conventional SDRT and low-complexity SDRT is shown in Fig. 4.5, where the corresponding results at the center point of the simulated Rx positions is taken as an example. The selected paths correspond to the indexed paths indicated in Fig. 4.3. It can be seen that the amplitude of each path is decreasing with the increasing sub-band center frequency $f_{\mathrm{c},i}$. For LOS and specular components, the amplitude and phase of each path based on conventional RT match well with the results calculated by the low-complexity SDRT algorithm. For diffuse scattering components, the amplitude matches well while the phase does not match as a result of the random phases of the rough surfaces.

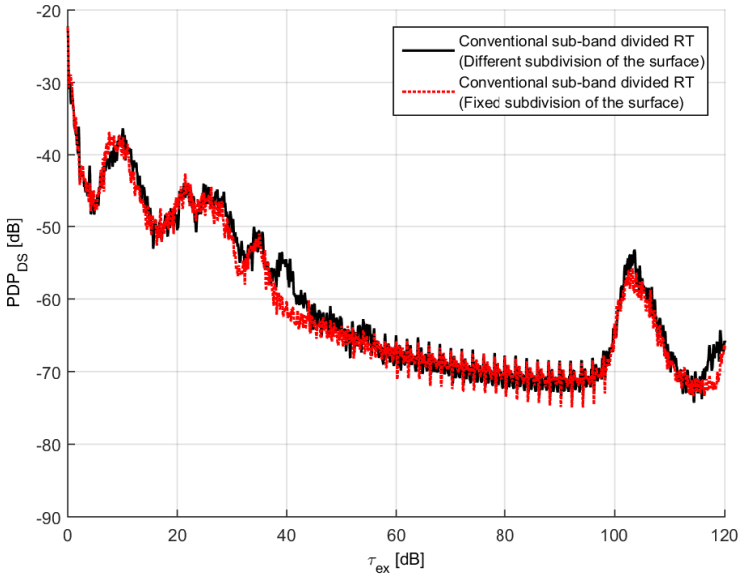

Figure 4.4: PDP of the diffuse scattering paths $\mathrm{PDP}_{\mathrm{DS}}$ with different and the subdivisions at different sub-bands relying on conventional SDRT.

4.2.3.2 Normalized CIR Comparison

For comparison, the normalized CIRs $h(\tau)$ at the selected 22 Rx locations, indicated by $\mathrm{Rx}_{\mathrm{idx}}$, are shown in Fig. 4.6 based on conventional SDRT and low-complexity SDRT, respectively. It can be seen that the specular components are mainly located between 0 ns and 45 ns, and 102 ns and 112 ns for our scenario. In general, the obtained CIRs based on conventional SDRT and low-complexity SDRT are comparable to each other even though small deviations exist, some of which are highlighted in Fig. 4.6. The main reason that causes the small deviations is evaluated as follow: for the reflection/penertration case, the error is introduced by the assumption that the effective permittivity $\varepsilon_{r,\mathrm{eff}}$ is assumed to be independent of the frequency; for the diffraction case, the reason is the presumable same value of each transition function in D_1, D_2, D_3 or D_4 for one diffraction point at different sub-bands. For the diffuse scattering case, the error results from the parameter U in (4.5), which further shows that the error is also related to the effective permittivity $\varepsilon_{r,\mathrm{eff}}$. It is worth mentioning that the random phase components are set identical in these two SDRT simulations for the same Rx position. Therefore, the deviation caused by the random phases has been removed.

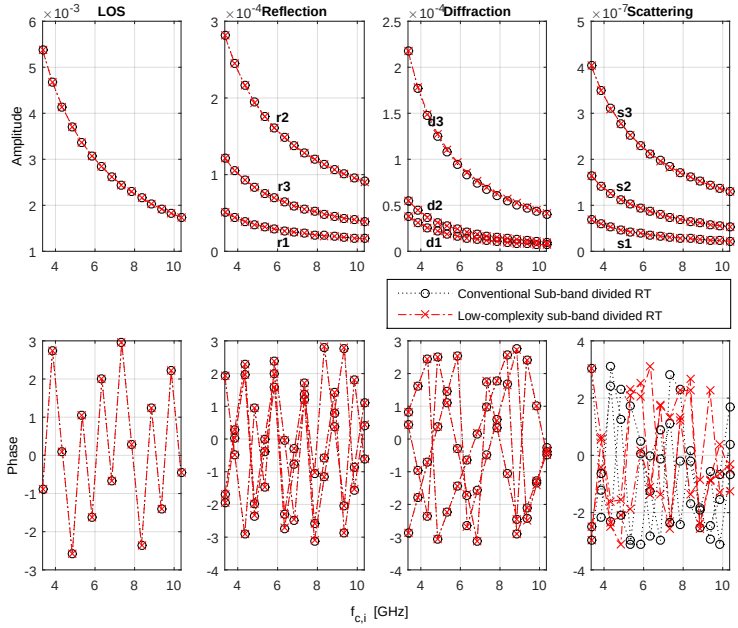

Figure 4.5: Amplitude and phase comparison results of propagation paths based on conventional SDRT and low-complexity SDRT. The results shown here correspond to the indexed propagation paths indicated in Fig. 4.3.

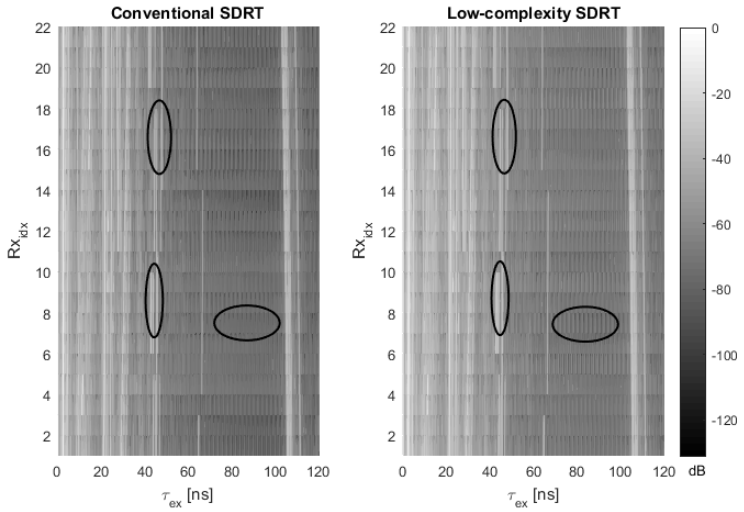

Figure 4.6: Comparison of normalized CIRs at the selected 22 Rx locations based on conventional SDRT and low-complexity SDRT. Some small deviations are highlighted by ellipses.

4.2.3.3 Simulation Time and PDP Comparison

The simulation time of low-complexity SDRT for one Rx location is about 222 s (2.4 GHz Intel Core i7 CPU with 8 GB RAM), while conventional SDRT takes about 3284 s, which means that the simulation time can be reduced by a factor of 15. In [95], it is mentioned that the more sub-bands the better is the accuracy of RT for the mmW indoor communication channels, but at the cost of computation time. Based on our proposed low-complexity algorithm for UWB indoor scenarios, the effect of computation time can be ignored when choosing the number of sub-bands. In Fig. 4.7, the normalized PDPs are compared by averaging the absolute square values of the normalized CIRs over the positions where RT simulations are available. The reason for the gap between the measurements and RT simulations is that (i) priori approximation of the input material parameters got from literature are used, (ii) some small objects are not considered in this large environment, and (iii) higher-order propagation mechanisms are not considered by the RT algorithm. The correlation coefficients of different PDPs are also calculated: it is 0.9830 between the low-complexity SDRT within 15 sub-bands and the measurements, while it is 0.9833 between the low-complexity SDRT within 50 sub-bands and the measurements. Therefore, we conclude that the PDPs calculated though conventional SDRT and low-complexity SDRT within 15 sub-bands are almost the same, while further increasing the number of sub-bands does not increase the simulation time much.

4.3 Calibration of RT Parameters

It is known that the accuracy of RT is related to the exact knowledge of all material parameters describing the environment. Although the reflection and transmission properties of building materials can be measured at UWB frequencies, the measured dielectric values can be inhomogeneous even in the same environment because of changing temperature and humidity conditions. Therefore, it is impossible to accurately define these dielectric parameters for each building. The situation is further exacerbated when the materials are made of a mixture of unknown components. Moreover, our RT tool involves not only the specular paths but also the diffuse scattering paths. The parameters used for the scattering mechanism cannot be directly measured. Hence, the parameters involved in the diffuse scattering model must be fitted by comparing to empirical measurement data for different materials [2].

For all these reasons the approximation of input material parameters lead to a mismatch between the simulation results of RT and empiric measurements, espe-

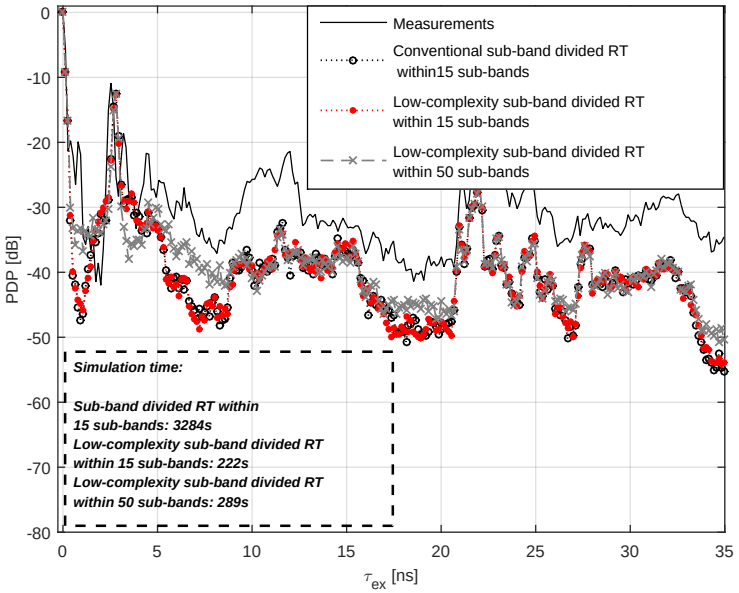

Figure 4.7: Normalized PDP comparison based on measurements, conventional SDRT, low-complexity SDRT with 15 sub-bands, low-complexity SDRT with 50 sub-bands.

cially for an excess delay greater than 35 ns in [61]. Therefore, it is necessary to implement a calibration algorithm for these RT parameters to improve the prediction accuracy of RT. To date, the calibration of RT based on the single objective optimization has been presented, but diffuse scattering components are not considered in [95, 96]. Due to the nonlinear combinatorial relationship between the power taps and material dielectric parameters, a simulated annealing approach is used in these works. This method provides a general optimal solution by simultaneously tuning the permittivity and conductivity of all materials to optimize the defined objective function.

In order to significantly improve the accuracy of SDRT for UWB indoor channels, the proposed low-complexity SDRT algorithm is used here. Then the MOSA algorithm and channel measurements at one Rx location need to be used to optimize the input material parameters within a given range, which refers to the dielectric and scattering parameters. The weighted sum approach is used for the proposed MOSA by projecting the multidimensional objective space into a single space. This calibration can improve the accuracy of SDRT in terms of the PDP and the RMS delay spread for all test Rx locations including those not considered by the calibration.

4.3.1 Channel Model for Calibration

Simulated annealing for single objective optimization has already been employed for RT calibration without taking diffuse scattering components into account [93, 96]. Based on our RT tool, we propose to optimize not only ε_r and σ but also S and α for each material, which play an important role for the propagation mechanisms. It has been mentioned that the reflection component and the scattering component intimately interact with each other as in (2.41), so that multiobjective optimization has to be considered. Therefore, we need to distinguish deterministic and diffuse scattering components in measurement firstly.

The search and subtract approach is a maximum likelihood method for separating the deterministic and diffuse scattering paths of CIR measurements [97]. The measurement data is available in the frequency domain, so the CTF at N_f frequency points for one Rx location is expressed as

$$\mathbf{H}_\mathrm{Meas} = [H_{\mathrm{Meas},0} \cdots H_{\mathrm{Meas},N_\mathrm{f}-1}]^\mathrm{T}, \tag{4.6}$$

where $[\cdot]^\mathrm{T}$ is the transpose operator. Then the corresponding CIR is obtained as

$$h_\mathrm{Meas}(\tau) = \mathbf{p}^\mathrm{T}(\tau)\mathbf{H}_\mathrm{Meas}, \tag{4.7}$$

where $\mathbf{p}(\tau)$ is the inverse Fourier transform coefficients as

$$\mathbf{p}(\tau) = [e^{j2\pi f_\mathrm{L}\tau} \cdots e^{j2\pi(f_\mathrm{L}+(N_\mathrm{f}-1)\Delta f)\tau}]^\mathrm{T}, \tag{4.8}$$

where f_L denotes the lowest measured frequency and Δf is the measured frequency step.

In order to improve the calibration accuracy greatly, the temporal deviation in the delay domain should be removed. As a reference to the deterministic part of the channel, only the deterministic propagation paths, including reflection, penetration, diffraction components, are taken into account in RT. The propagation path delay $\tau_{\mathrm{RT}_\mathrm{det},k}$ and the complex amplitude $\eta_{\mathrm{RT}_\mathrm{det},k}$ of the $k-$th deterministic path can be calculated directly by RT. Then the CIR $h_{\mathrm{RT}_\mathrm{det}}(\tau)$ at one Rx location is represented as

$$h_{\mathrm{RT}_\mathrm{det}}(\tau) = \sum_{k=1}^{K} \eta_{\mathrm{RT}_\mathrm{det},k}\delta(\tau - \tau_{\mathrm{RT}_\mathrm{det},k}), \tag{4.9}$$

where K is the total number of deterministic paths. According to the $k-$th propagation path delay $\tau_{\mathrm{RT}_\mathrm{det},k}$, the corresponding CIRs interval for the $k-$th path of RT and the measurement is set as $\tau'_{\mathrm{RT}_\mathrm{det},k} \in [\tau_{\mathrm{RT}_\mathrm{det},k} - 5\cdot\Delta\tau, \tau_{\mathrm{RT}_\mathrm{det},k} + 5\cdot\Delta\tau]$, where $\Delta\tau$ is the delay resolution. Furthermore, the cross-correlation is obtained by

$$\mathrm{R}_k(\tau') = \int |h^*_{\mathrm{RT}_\mathrm{det}}(\tau'_{\mathrm{RT}_\mathrm{det},k})||h_\mathrm{Meas}(\tau'_{\mathrm{RT}_\mathrm{det},k} + \tau')|d\tau'_{\mathrm{RT}_\mathrm{det},k}, \tag{4.10}$$

where $|\cdot|$ denotes the absolute value. Then the $k-$th propagation path delay of the measurement $\tau_{\mathrm{Meas}_{\mathrm{det}},k}$ is obtained by

$$\tau_{\mathrm{Meas}_{\mathrm{det}},k} \triangleq \arg\max_{\tau'}\{\mathrm{R}_k(\tau')\}. \tag{4.11}$$

In addition, the complex amplitude $\eta_{\mathrm{Meas}_{\mathrm{det}},k}$ of the $k-$th propagation path in the measurement can be obtained as

$$\eta_{\mathrm{Meas}_{\mathrm{det}},k} = \frac{\mathbf{p}^{\mathrm{T}}(\tau_{\mathrm{Meas}_{\mathrm{det}},k})\mathbf{H}_{\mathrm{Meas}_{\mathrm{ds}},k}}{\mathbf{p}^{\mathrm{T}}\mathbf{p}}, \tag{4.12}$$

where $\mathbf{H}_{\mathrm{Meas}_{\mathrm{ds}},k}$ is the remaining CTF after subtracting the effect of the $(k-1)$th deterministic peak as [97]

$$\mathbf{H}_{\mathrm{Meas}_{\mathrm{ds}},k} = \begin{cases} \mathbf{H}_{\mathrm{Meas}} & k = 1, \\ \mathbf{H}_{\mathrm{Meas}_{\mathrm{ds}},k-1} - \eta_{\mathrm{Meas}_{\mathrm{det}},k-1}\mathbf{p}^{*}(\tau_{\mathrm{Meas}_{\mathrm{det}},k-1}) & k > 1. \end{cases} \tag{4.13}$$

Then the CIRs $h_{\mathrm{Meas}_{\mathrm{det}}}(\tau)$ and $h_{\mathrm{Meas}_{\mathrm{ds}}}(\tau)$ of the deterministic and diffuse scattering components can be obtained. In addition, the CIR of diffuse scattering components based on RT $h_{\mathrm{RT}_{\mathrm{ds}}}(\tau)$ can be calculated directly by considering only the diffuse scattering components in RT.

4.3.2 MOSA Algorithm

Simulated annealing is derived from the physical heating of a material, where the material is critically heated and then gradually cooled until reaching a steady state [96]. It is an iterative optimization algorithm which is able to provide a sub-optimal solution for arbitrary degrees of nonlinearity [95]. In the following, T_0 is a control parameter that corresponds to the initial temperature in analogy with the physical annealing process and $\mathbf{x}$ is the parameter vector which needs to be optimized. The MOSA algorithm in this work uses the weighted sum approach to project the multidimensional parameter space into a one-dimensional space [98]. Only prior measurements at one Rx location is selected in the current calibration work. The sum-weighted objective function for our case is described as

$$\mathrm{f}(\mathbf{x}, \lambda_{\mathrm{det}}, \lambda_{\mathrm{ds}}) = \lambda_{\mathrm{det}}\mathrm{f}_{\mathrm{det}}(\mathbf{x}) + \lambda_{\mathrm{ds}}\mathrm{f}_{\mathrm{ds}}(\mathbf{x}), \tag{4.14}$$

where the weighting factors should satisfy $\lambda_{\{.\}} \in (0,1)$ and $\lambda_{\mathrm{det}} + \lambda_{\mathrm{ds}} = 1$, and the objective function $\mathrm{f}_{\mathrm{det}}(\mathbf{x})$, defined as the RMS error between the measured and RT simulated tap powers of the deterministic paths, is calculated as

$$\mathrm{f}_{\mathrm{det}}(\mathbf{x}) = \sqrt{\frac{1}{K}\sum_{k=1}^{K}\left(\frac{|\eta_{\mathrm{Meas}_{\mathrm{det}},k}|^2 - |\eta_{\mathrm{RT}_{\mathrm{det}},k}|^2}{|\eta_{\mathrm{Meas}_{\mathrm{det}},k}|^2}\right)^2}, \tag{4.15}$$

where $|\eta_{\mathrm{Meas}_{\mathrm{det}},k}|$ and $|\eta_{\mathrm{RT}_{\mathrm{det}},k}|$ are the amplitudes of the propagation paths normalized by the LOS component, while the objective function $\mathrm{f}_{\mathrm{ds}}(\mathbf{x})$, defined as the MRE between the measured and RT simulated instantaneous powers of the diffuse scattering components, is computed as

$$\mathrm{f}_{\mathrm{ds}}(\mathbf{x}) = \frac{1}{N_\tau} \int |\frac{|h_{\mathrm{Meas}_{\mathrm{ds}},k}(\tau_{\mathrm{ex}})|^2 - |h_{\mathrm{RT}_{\mathrm{ds}},k}(\tau_{\mathrm{ex}})|^2}{|h_{\mathrm{Meas}_{\mathrm{ds}},k}(\tau_{\mathrm{ex}})|^2}| d\tau_{\mathrm{ex}}, \tag{4.16}$$

where N_τ is the number of delay points, $|h_{\mathrm{Meas}_{\mathrm{ds}},k}(\tau_{\mathrm{ex}})|$ and $|h_{\mathrm{RT}_{\mathrm{ds}},k}(\tau_{\mathrm{ex}})|$ are normalized CIRs defined over the excess delay τ_{ex}. In order to get the optimal parameter vector $\mathbf{x}$, both objection functions need to be minimized.

The basic steps involved in the MOSA algorithm for RT calibration are illustrated as following:

1. We use the normalized objective functions (4.15) and (4.16) that are in the same numerical range, which allow us to fix $\lambda_{\mathrm{det}} = 0.5$ and $\lambda_{\mathrm{ds}} = 0.5$ and avoid another time-consuming optimization step for these two parameters.

2. Starting with an initial parameter vector $\mathbf{x}'$, which is selected from the literature, at an initial temperature T_0, the solutions of objective functions $\mathrm{f}_{\mathrm{det}}(\mathbf{x}')$ and $\mathrm{f}_{\mathrm{ds}}(\mathbf{x}')$ are evaluated. The corresponding results are put into a Pareto set of solutions. The Pareto set, which is a subset of feasible points of solutions, contains all points in which at least one objective function is minimized.

3. In order to get the realistic results, the ranges of each elements are defined. A new random parameter vector $\mathbf{x}''$ is taken from the neighborhood of $\mathbf{x}'$ within the given ranges, and the solutions of related objective functions are re-valuated.

4. Comparing the new solutions with all other solutions in the Pareto set, $\mathbf{x}''$ is made as the current parameter vector and the Pareto set is updated if both objective functions are minimized as $\mathrm{f}_{\mathrm{det}}(\mathbf{x}'') \leq \mathrm{f}_{\mathrm{det}}(\mathbf{x}')$ and $\mathrm{f}_{\mathrm{ds}}(\mathbf{x}'') \leq \mathrm{f}_{\mathrm{ds}}(\mathbf{x}')$. Then the process restarts from step 6. If $\mathbf{x}''$ is not the optimal parameter vector for both objection functions, then

   $$\Delta \mathrm{f} = \mathrm{f}(\mathbf{x}'', \lambda_{\mathrm{det}}, \lambda_{\mathrm{ds}}) - \mathrm{f}(\mathbf{x}', \lambda_{\mathrm{det}}, \lambda_{\mathrm{ds}}) \tag{4.17}$$

   is evaluated.

5. In order to avoid being trapped into a local minimum, the parameter vector $\mathbf{x}''$ is accepted as the current parameter vector with the probability

   $$p = \begin{cases} e^{\frac{\Delta \mathrm{f}}{T}} & \text{if } \Delta \mathrm{f} > 0, \\ 1 & \text{if } \Delta \mathrm{f} \leq 0. \end{cases} \tag{4.18}$$

If $\mathbf{x}''$ is accepted, $\mathbf{x}''$ is made the current parameter vector. If $\mathbf{x}''$ is not accepted, $\mathbf{x}'$ is retained as the current parameter vector.

6. The algorithm restarts running by selecting the referenced solutions of the objective functions corresponding to the minimum $\mathrm{f}(\mathbf{x}, \lambda_{\mathrm{det}}, \lambda_{\mathrm{ds}})$ in the Pareto set.

7. The mentioned steps repeatedly run L times at the same temperature T_0. Then the algorithm restarts with an updated temperature, which is obtained by reducing the current temperature by a temperature factor N_{T}, where $N_{\mathrm{T}} < 1$.

8. The aforementioned steps run iteratively until the predefined number of iterations M is achieved.

To make this description more clear, the flowchart of the MOSA algorithm is given in Fig. 4.8. It is mainly divided into three steps: initialization, judging conditions and search for Pareto Front. These three steps are indicated by three different colors in Fig. 4.8.

4.3.3 Numerical Results

The indoor scenario used for both the measurement campaign and SDRT is the same as the illustration in Fig. 4.3 in Section 4.2.2. Low-complexity SDRT simulations are computed for the middle horizontal line of the grid highlighted in blue in Fig. 4.3 (b). The measurements at the middle point of the horizontal line is used for the calibration. The entire UWB bandwidth $B = 7.5\,\mathrm{GHz}$, which is divided into $\mathcal{I} = 15$ sub-bands with $B_i = 500\,\mathrm{MHz}$ each. The optimized material parameters are the elements of the parameter vector $\mathbf{x}$

$$\mathbf{x} = [\varepsilon_{\mathbf{c},r}, \sigma_{\mathbf{c}}, S_{\mathbf{c}}, \alpha_{\mathbf{c}}, \varepsilon_{\mathbf{g},r}, S_{\mathbf{g}}, \alpha_{\mathbf{g}}], \tag{4.19}$$

where $\mathbf{c}$ indicates concrete and $\mathbf{g}$ glass. The metallic block is considered as a PEC. The conductivity of glass is $\sigma_{\mathbf{c}} = 0\,\mathrm{S/m}$. The involved propagation mechanisms for the calibration are LOS, reflection up to the third order, penetration, single-order diffraction, single bounce scattering, and scattering-reflection cases.

4.3.3.1 Paths Separation from Measurements

Firstly, we need to separate the deterministic and the diffuse scattering paths from channel measurements at the selected Rx position. Based on (4.10), the deterministic paths in the measurements are identified such that slight time of arrival deviations

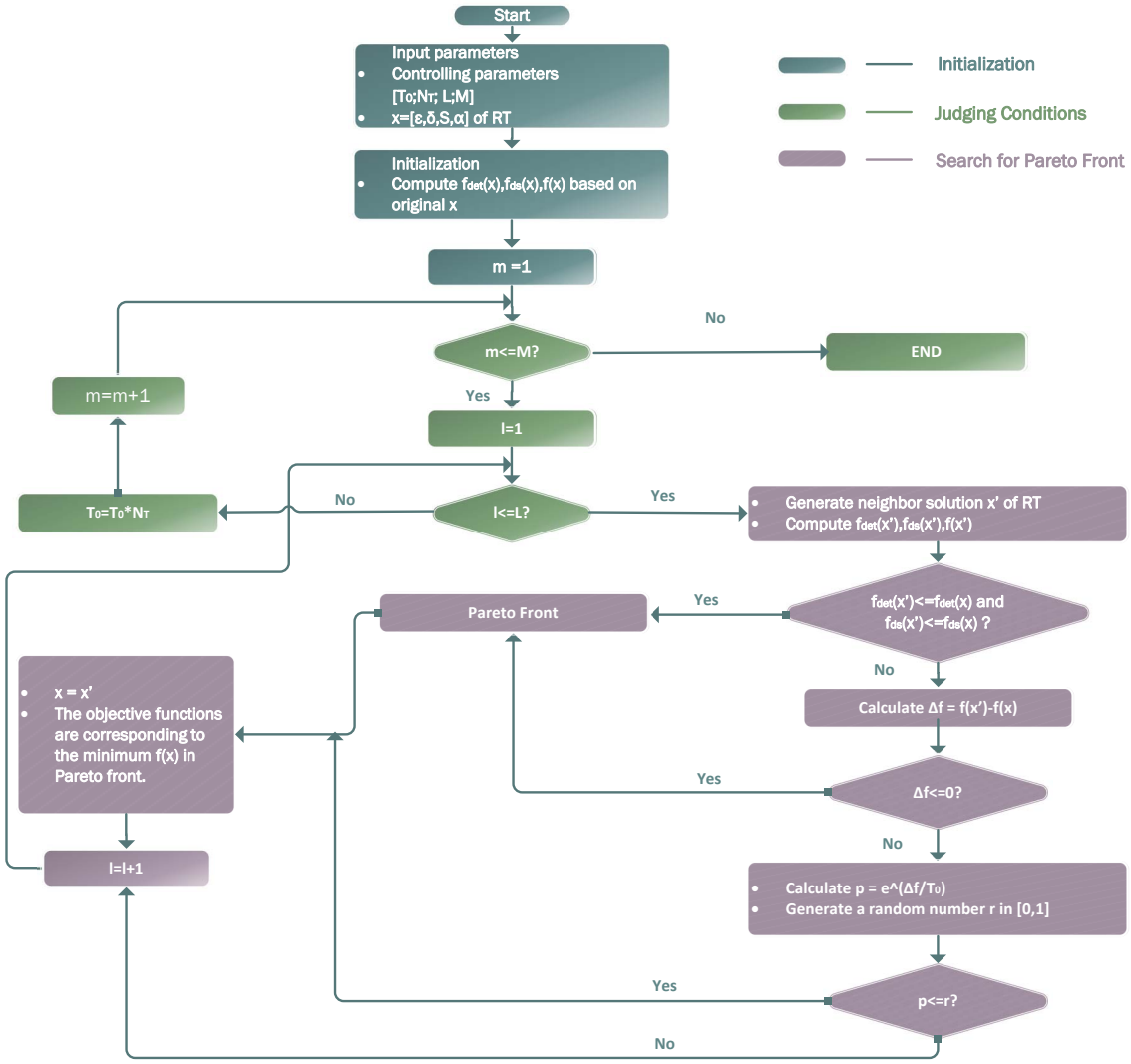

Figure 4.8: Flowchart of the MOSA algorithm, which is mainly divided into three steps: initialization, judging conditions and search for Pareto Front.

of the deterministic paths can be tolerated. In Fig. 4.9(b), slight time of arrival deviations of the deterministic paths around 2.7 ns and 4.4 ns can be clearly observed. The precise mapping of the measured and RT simulated propagation paths can help to improve the calibration accuracy. Fig. 4.9 shows the normalized amplitude $|\eta_{\mathrm{det}}|$ of the deterministic paths in measurements and low-complexity SDRT before the calibration. In order to avoid a large deviation of the power of detected paths, a threshold of the difference between $|\eta_{\mathrm{Meas}_{\mathrm{det}},k}|$ and $|\eta_{\mathrm{RT}_{\mathrm{det}},k}|$ of the $k-$th deterministic propagation path is set to 20 dB. If the difference exceeds 20dB, the $k-$th

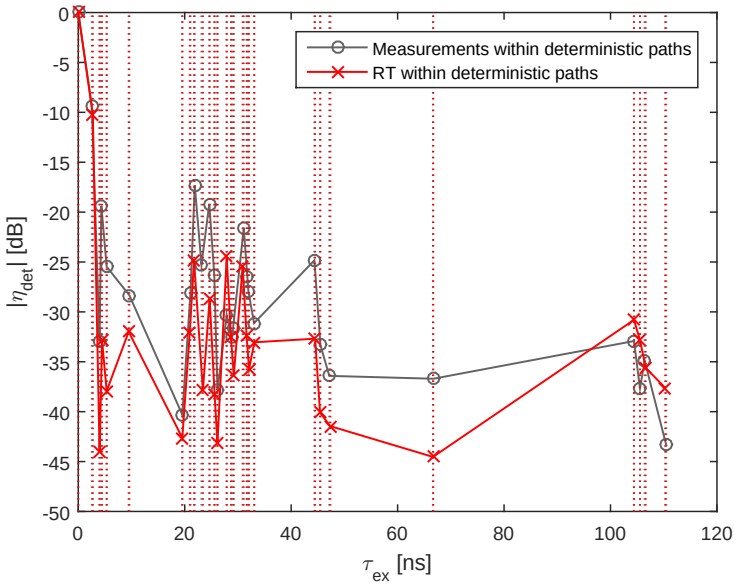

(a) Normal view

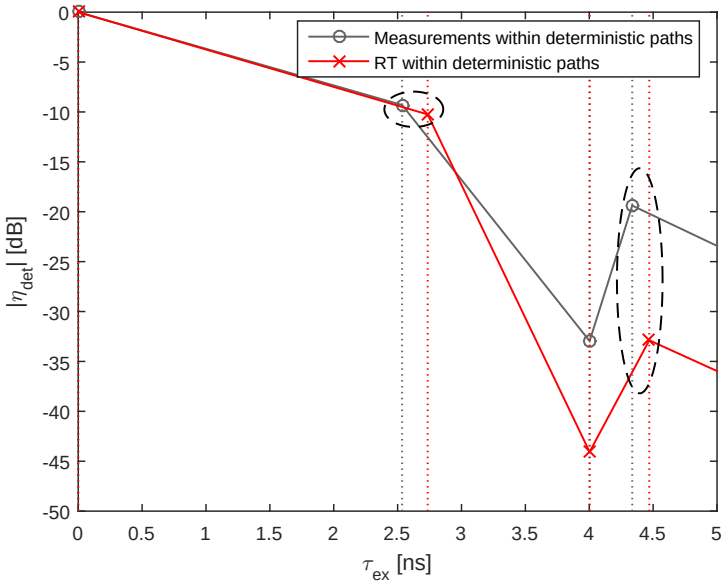

(b) Zoomed view

Figure 4.9: Normalized amplitude $|\eta_{\text{det}}|$ of the deterministic paths in measurements and low-complexity SDRT before the calibration.

deterministic path is deleted.

Removing the deterministic components from the measurements based on the search and subtract approach, the remaining diffuse scattering components are calculated as the inverse Fourier transform of $\mathbf{H}_{\text{Meas}_{\text{ds}},k}$. The CIRs $|h_{\text{Meas}_{\text{ds}}}(\tau_{\text{ex}})|$ and

$|h_{\mathrm{RT_{ds}}}(\tau_{\mathrm{ex}})|$ are shown in Fig. 4.10.

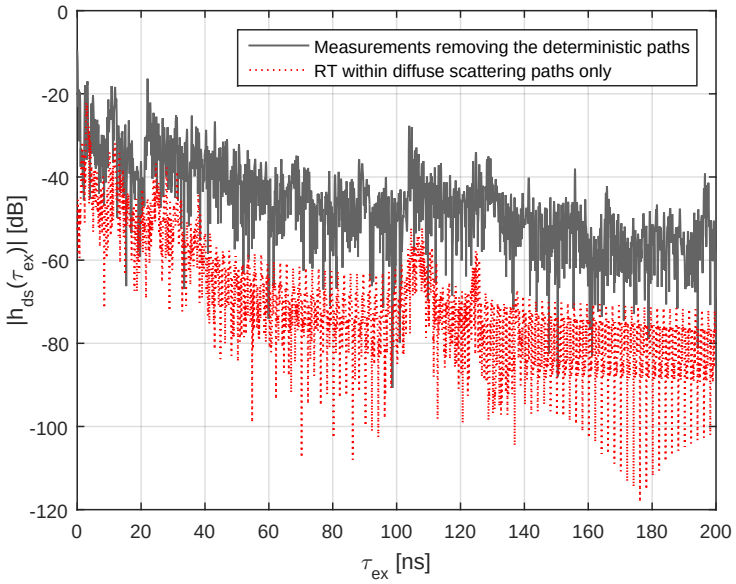

Figure 4.10: Normalized CIRs $|h_{\mathrm{ds}}(\tau_{\mathrm{ex}})|$ of the measurements and low-complexity SDRT before the calibration considering the diffuse scattering paths only.

4.3.3.2 Calibration Results

In order to avoid the random phases of the scattering components in RT influencing $\mathrm{f_{ds}}(\mathbf{x})$, a matrix with $\mathcal{I} \times N_{\mathrm{s}}$ random elements is given at the beginning of the optimization process, where the number of scattering paths calculated from RT is $N_{\mathrm{s}} = 26614$. Balancing the number of parameter vectors and the simulation time, the control factors in the calibration algorithm are set as $[T_0, N_{\mathrm{T}}, L, M] = [2, 0.95, 20, 5000]$.

The initial parameter vector is picked up from [61] as

$$\mathbf{x}' = [6, 0.08, 0.4, 4, 5.5, 0.4, 4]. \tag{4.20}$$

Each element of $\mathbf{x}$ has its individual range, which are summarized from [2], [99–102],

as

$$\begin{cases} 4 \leq \varepsilon_{\mathbf{c},r} \leq 9, \\ 0.023 \leq \sigma_{\mathbf{c}} \leq 0.5, \\ 0 \leq S_{\mathbf{c}} \leq 1, \\ 1 \leq \alpha_{\mathbf{c}} \leq 4, \\ 2 \leq \varepsilon_{\mathbf{g},r} \leq 8, \\ 0 \leq S_{\mathbf{g}} \leq 1, \\ 1 \leq \alpha_{\mathbf{g}} \leq 4. \end{cases} \tag{4.21}$$

In Fig. 4.11, the solutions of the objective functions related to the feasible parameter vectors are shown, and the Pareto front is given. In order to make the optimized

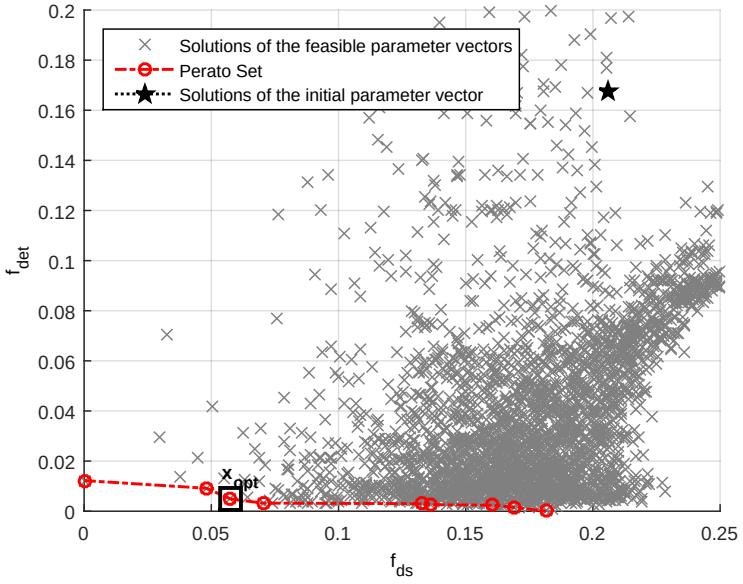

Figure 4.11: Solutions of objective functions related to the feasible parameter vectors within the Pareto front.

results clear, the obtained $\mathrm{f}_{\mathrm{det}}(\mathbf{x})$ and $\mathrm{f}_{\mathrm{ds}}(\mathbf{x})$ are normalized by the respective minimum values. Taking the solutions in the Pareto set into consideration, one parameter vector $\mathbf{x}_{\mathrm{opt}}$ is selected

$$\mathbf{x}_{\mathrm{opt}} = [8.92, 0.046, 0.74, 3, 3.7, 0.32, 3]. \tag{4.22}$$

It can be seen that $S_{\mathbf{c}}$ becomes larger, while $S_{\mathbf{g}}$ becomes smaller, which is confirmed by reality that the surface of the concrete is relatively rougher and of the glass is relatively smoother. Moreover, the smaller $\alpha_{\mathbf{c}}$ and $\alpha_{\mathbf{g}}$ indicate a widening of the scattering lobe.

4.3.3.3 PDP and RMS Delay Spread Comparison

Using the parameter vector $\mathbf{x}_{\text{opt}}$ in low-complexity SDRT for all Rx locations including those not considered by the calibration, the normalized PDP and the RMS delay spread τ_{rms} are compared by averaging the normalized CIRs over the 22 horizontal positions, Rx_{idx}. The results are shown in Fig. 4.12. It is worth mentioning that the reflection-scattering case is also considered by RT. Based on the optimized material

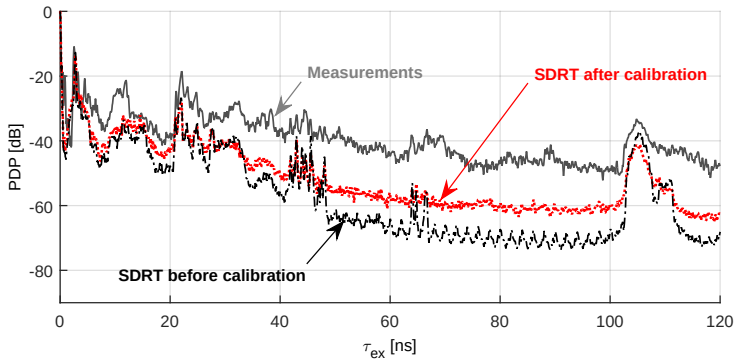

(a) PDP comparison

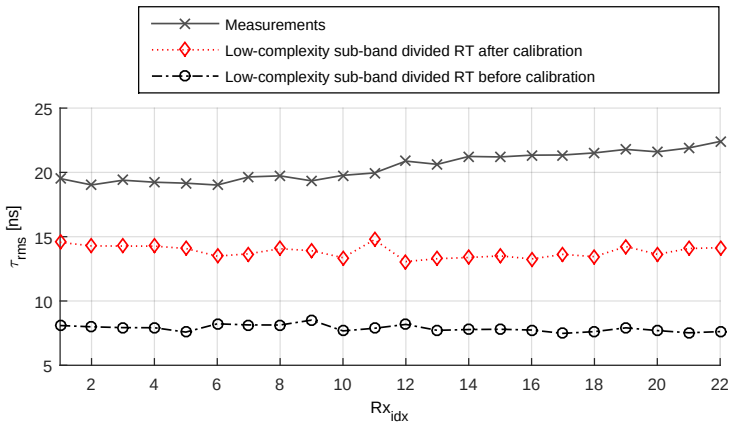

(b) RMS delay spread comparison

Figure 4.12: Normalized PDP and RMS delay spread comparison based on the measurements, low-complexity SDRT before calibration, and low-complexity SDRT after calibration.

parameters, the differences of the normalized PDP and the RMS delay spread between measurements and low-complexity SDRT simulation results are minimized. The difference of normalized PDPs between measurements and RT simulation is reduced by 10 dB and the RMS delay spread is improved about 5 ns despite only one prior measurement is used for the calibration. Moreover, it can be seen that the

power of the diffuse components is increased, while the power of the deterministic components are not influenced. The reasons for the remaining gap are the large dimensions of the environment which cannot be modeled absolutely accurate and the higher-order propagation mechanisms that are not considered by our RT algorithm.

4.4 Sub-band Divided RT Algorithm Using DPS Sequences

As in Section 3.3, we are also interested in modeling the channel characteristics at multiple mobile terminal positions in UWB indoor scenarios. Although we have proposed a low-complexity SDRT algorithm for one terminal position, the computational complexity is still extremely high when involving multiple mobile terminal positions. Moreover, some indoor positioning techniques require for high positioning accuracy data from measurements/simulations with a very fine spatial resolution. To cope with this, a parallel ray approximation (PRA) algorithm is proposed in [88] to reduce the computation time in this situation. However, the computation time is still proportional to the number of terminal positions. For band-limited fading processes, it is known that a projection on a subspace spanned by two-dimensional DPS sequences [81] allows for a substantial complexity reduction of GSCMs [84, 86]. In Section 3.3, this insight has been applied to obtain a low-complexity DPS subspace based RT algorithm for a wideband communication system in an indoor scenario. We extend the wideband RT in Section 3.3 to the UWB case by expanding the DPS sequences to each sub-band. Due to the same geometrical information of the propagation paths for all sub-bands, the subspace dimension and basis coefficients in the frequency domain do not need to be recalculated at different sub-bands. The accuracy of the proposed algorithm is evaluated by comparing it to low-complexity SDRT without the DPS subspace projection. Moreover, the effect of antenna characteristics on the proposed algorithm is analyzed.

4.4.1 CTF of Low-complexity SDRT Algorithm

RT calculates all propagation paths connecting the Tx and the Rx based on geometric and electromagnetic computations. In [88], a first simplification has been proposed by performing the geometric computation once at the beginning of the procedure, while the electromagnetic calculation are performed at each individual frequency $f_{c,i}$. In the low-complexity SDRT algorithm, see Section 4.2, both the geometric computation and the electromagnetic computation need to be performed

only once for all sub-bands. The corresponding calculation of propagation paths at other sub-bands can be derived based on the results at one sub-band.

For a static Tx and multiple Rx positions, the CTF depends on the Rx positions $\mathbf{u}_n$. We are interested in the case that $\mathbf{u}_n = \mathbf{u}_0 + \mathbf{d}_\mathrm{S} n$, where $n \in \{0, \ldots, N-1\}$ is the discrete Rx position index and N is the number of samples in the space domain, $\mathbf{u}_0$ is the initial Rx position, and $\mathbf{d}_\mathrm{S}$ is the spatial resolution vector. The CTF based on low-complexity SDRT at one sub-band can be obtained as

$$H^i_\mathrm{SDRT}[q_i, \mathbf{u}_n] = H^i_\mathrm{SDRT}(q_i f_\mathrm{S}, \mathbf{u}_0 + \mathbf{d}_\mathrm{S} n) = \sum_{l=1}^{L} \eta_l[f_{\mathrm{c},i}, \mathbf{u}_n] e^{-j2\pi q_i \theta_l[\mathbf{u}_n]}, \tag{4.23}$$

where f_S denotes the width of a frequency bin, $l \in \{1, \ldots, L\}$ is the index of the propagation path, L is the total number of propagation paths, $\theta_l[\mathbf{u}_n] = \tau_l[\mathbf{u}_n] f_\mathrm{S}$ is the normalized delay of the $l-$th path with τ_l denoting the excess delay of the l-th path, where the delay of the first arriving path is defined as $\tau_1 = 0\,\mathrm{s}$, $\eta_l[f_{\mathrm{c},i}, \mathbf{u}_n]$ is the complex electric field of the l-th path at the center frequency $f_{\mathrm{c},i}$ of the i-th sub-band, $q_i \in \{-\lfloor \frac{Q_i}{2} \rfloor, \ldots, \lfloor \frac{Q_i}{2} \rfloor - 1\}$ is the discrete frequency index vector at the i-th sub-band, Q_i is the number of samples in the frequency domain at the i-th sub-band, and $\lfloor \cdot \rfloor$ indicates the floor function. Both η_l and τ_l depend on the Rx position $\mathbf{u}_n$. Finally, the relevant H_SDRT in the entire frequency range can be obtained by combining all CTFs H^i_SDRT at different sub-bands as

$$H_\mathrm{SDRT}[q, \mathbf{u}_n] = \left[H^1_\mathrm{SDRT}[q_1, \mathbf{u}_n]^\mathrm{T} \; H^2_\mathrm{SDRT}[q_2, \mathbf{u}_n]^\mathrm{T} \cdots \; H^I_\mathrm{SDRT}[q_\mathcal{I}, \mathbf{u}_n]^\mathrm{T} \right]^\mathrm{T}, \tag{4.24}$$

where $[\cdot]^\mathrm{T}$ denotes the transpose function.

4.4.2 Computational Complexity Reduction

In the following we present our method for reducing the computational complexity by means of a projection on a subspace spanned by DPS sequences. To reduce the computational complexity of low-complexity SDRT for multiple Rx positions, we propose a low-complexity DPS subspace based RT algorithm. The prerequisite of the proposed algorithm is to fulfill the same conditions as the PRA algorithm. Therefore, we introduce first the PRA algorithm and thereafter the extensions with the DPS sequences. Note that RT needs to be performed only once at one sub-band at the initial Rx position $\mathbf{u}_0$ for these two algorithms.

4.4.2.1 PRA Algorithm Based on Low-Complexity SDRT

PRA is an efficient RT algorithm for modeling UWB indoor propagation channels at multiple terminal positions [88]. The basic concept is that the gain coefficients

of propagation paths reaching the nearby targets are assumed to have the same magnitude but different phases. This approximation is valid when the following far-field conditions are fulfilled [88]:

$$|\mathbf{u}_{\mathrm{Tx}} - \mathbf{u}_0| \gg \lambda_{\mathrm{l}}, \tag{4.25}$$

$$|\mathbf{u}_{\mathrm{Tx}} - \mathbf{u}_0| \gg |\mathbf{u}_n - \mathbf{u}_0| = |\mathbf{d}_{0,n}|, \tag{4.26}$$

where λ_{l} is the wavelength at the lowest center frequency, $\mathbf{u}_{\mathrm{Tx}}$ is the Tx position coordinate, and $\mathbf{d}_{0,n}$ is the vector pointing to the Rx position $\mathbf{u}_n$ from the initial Rx position $\mathbf{u}_0$. The CTF at the Rx position $\mathbf{u}_n$, relying on the results of the initial Rx position $\mathbf{u}_0$, at the i-th sub-band is approximated as

$$H^i_{\mathrm{PRA}}[q_i, \mathbf{u}_n] \approx \sum_{l=1}^{L} \eta_l[f_{\mathrm{c},i}, \mathbf{u}_0] e^{-j2\pi q_i \theta_l[\mathbf{u}_0]} e^{j\frac{2\pi \mathbf{d}_{0,n}\cdot \mathbf{v}_l}{\lambda_{\mathrm{c},i}}}, \tag{4.27}$$

$\lambda_{\mathrm{c},i}$ is the wavelength corresponding to $f_{\mathrm{c},i}$, and $\mathbf{v}_l$ is the unit vector of the l-th path reaching $\mathbf{u}_0$. Furthermore, the relevant H_{PRA} in the entire frequency range can be obtained in the same manner as in (4.24).

4.4.2.2 DPS Subspace Algorithm Based on Low-Complexity SDRT

We exploit the band-limited property of the CTF by projecting each path $l \in \{1, \ldots, L\}$ to a subspace spanned by two-dimensional DPS sequences. The detailed information of DPS sequences has been presented in Section 3.3. The two-dimensions refer to the frequency and space dimension here. The two key parameters for the setup of the i-th sub-band are

- the maximum normalized excess delay $\theta_{\mathrm{Dmax},i} = \tau_{\mathrm{max},i} f_{\mathrm{S}}$, where $\tau_{\mathrm{max},i}$ is the maximum excess delay among all paths at the initial Rx position $\mathbf{u}_0$ for the i-th sub-band, and
- the normalized minimum and maximum DoA $\xi_{\mathrm{Dmin},i} = \cos(\psi_{\mathrm{min},i})\frac{\|\mathbf{d}_{\mathrm{S}}\|}{\lambda_{\mathrm{c},i}}$ and $\xi_{\mathrm{Dmax},i} = \cos(\psi_{\mathrm{max},i})\frac{\|\mathbf{d}_{\mathrm{S}}\|}{\lambda_{\mathrm{c},i}}$, where $\|\mathbf{d}_{\mathrm{S}}\|$ is the distance between antenna positions, $\|\cdot\|$ denotes Euclidean norm, the DoA ψ is defined as the angle between $\mathbf{d}_{0,n}$ and $\mathbf{v}_l$, $\psi_{\mathrm{min},i}$ and $\psi_{\mathrm{max},i}$ are the minimum and maximum DoAs among all paths at the initial Rx position $\mathbf{u}_0$ for the i-th sub-band.

As mentioned previously the geometric computation of propagation paths is the same for all sub-bands, so $\tau_{\mathrm{max},i}$, $\psi_{\mathrm{min},i}$ and $\psi_{\mathrm{max},i}$ are independent of the sub-band. Thus, $\theta_{\mathrm{Dmax},i}$ is also independent of the sub-band. We drop the index i from $\theta_{\mathrm{Dmax},i}$

and write θ_{Dmax} in the rest of the paper. However, $\xi_{\mathrm{Dmin},i}$ and $\xi_{\mathrm{Dmax},i}$ are related to the sub-band because of their dependency on $\lambda_{\mathrm{c},i}$. The band-limited region at the i-th sub-band is defined by the Cartesian product as [84]

$$W_i = W_{\mathrm{f}} \times W_{\mathrm{d}i} = [0, \theta_{\mathrm{Dmax}}] \times [\frac{\xi_{\mathrm{Dmin},i} + \xi_{\mathrm{Dmax},i}}{2}, \frac{\xi_{\mathrm{Dmax},i} - \xi_{\mathrm{Dmin},i}}{2}]. \tag{4.28}$$

The relevant index set is denoted by

$$I_i = I_{\mathrm{f}i} \times I_{\mathrm{d}} = \{-\lfloor \frac{Q_i}{2} \rfloor, \ldots, \lfloor \frac{Q_i}{2} \rfloor - 1\} \times \{0, \ldots, N-1\}. \tag{4.29}$$

The approximate DPS subspace representation $\boldsymbol{H}_{\mathrm{DPS}}^{(D_i)}$ with the subspace dimension D_i for the i-th sub-band can be expressed as

$$H_{\mathrm{DPS}}^{(D_i)}[q_i, \mathbf{u}_n] \approx \boldsymbol{V_i}\tilde{\boldsymbol{\alpha}}_i, \tag{4.30}$$

where the two-dimensional DPS basis vector at the i-th sub-band is

$$\boldsymbol{V_i} = \boldsymbol{V_i}(W_i, I_i) = \boldsymbol{V_i}(W_{\mathrm{f}}, I_{\mathrm{f}i}) \diamond \boldsymbol{V_i}(W_{\mathrm{d}i}, I_{\mathrm{d}}). \tag{4.31}$$

$\tilde{\boldsymbol{\alpha}}_i$ are the approximate basis coefficients at the i-th sub-band. It can be observed that the basis vectors $\boldsymbol{V_i}(W_{\mathrm{f}}, I_{\mathrm{f}i})$ and $\boldsymbol{V_i}(W_{\mathrm{d}i}, I_{\mathrm{d}})$ change along different sub-bands. The approximate basis coefficients at the i-th sub-band can be expressed by a Kronecker product

$$\tilde{\boldsymbol{\alpha}}_i = \sum_{l=1}^{L} \eta_l[f_{\mathrm{c},i}, \mathbf{u}_0] \underbrace{(\boldsymbol{V_i}(W_{\mathrm{f}}, I_{\mathrm{f}i})\boldsymbol{\chi}_{\mathrm{f}i}(\theta_l))}_{\boldsymbol{\gamma}_{l,i}^{\mathrm{f}} : \approx \tilde{\boldsymbol{\gamma}}_{l,i}^{\mathrm{f}}(\tau_l; W_{\mathrm{f}}, I_{\mathrm{f}i})} \otimes \underbrace{(\boldsymbol{V_i}(W_{\mathrm{d}i}, I_{\mathrm{d}})\boldsymbol{\chi}_{\mathrm{d}i}(\xi_{l,i}))}_{\boldsymbol{\gamma}_{l,i}^{\mathrm{d}} : \approx \tilde{\boldsymbol{\gamma}}_{l,i}^{\mathrm{d}}(\psi_l; W_{\mathrm{d}i}, I_{\mathrm{d}})}, \tag{4.32}$$

where ψ_l is the DoA of the l-th path, while $\xi_{l,i}$ is the normalized DoA at the i-th sub-band, and

$$\boldsymbol{\chi}_{\mathrm{f}i}(\theta_l) = [\vartheta_{\mathrm{f}}^{(-\lfloor \frac{Q_i}{2} \rfloor)}, \vartheta_{\mathrm{f}}^{(-\lfloor \frac{Q_i}{2} \rfloor + 1)}, \ldots, \vartheta_{\mathrm{f}}^{(\lfloor \frac{Q_i}{2} \rfloor - 1)}]^{\mathrm{T}} \tag{4.33}$$

and

$$\boldsymbol{\chi}_{\mathrm{d}i}(\xi_{l,i}) = [\vartheta_{\mathrm{d}i}^{0}, \vartheta_{\mathrm{d}i}^{1}, \ldots, \vartheta_{\mathrm{d}i}^{(N-1)}]^{\mathrm{T}} \tag{4.34}$$

are the complex exponential functions, in which $\vartheta_{\mathrm{f}} = e^{-j2\pi\theta_l}$ and $\vartheta_{\mathrm{d}i} = e^{j2\pi\xi_{l,i}}$, respectively. Then the approximated projections of the complex exponential functions on the DPS basis vectors $\tilde{\boldsymbol{\gamma}}_{l,i}^{\mathrm{f}}(\tau_l; W_{\mathrm{f}}, I_{\mathrm{f}i})$ and $\tilde{\boldsymbol{\gamma}}_{l,i}^{\mathrm{d}}(\psi_l; W_{\mathrm{d}i}, I_{\mathrm{d}})$ can be used to simplify the calculation of the complex exponential functions by the scaled and shifted approximated DPS wave functions as in (3.47). It can be seen that the approximated projection $\tilde{\boldsymbol{\gamma}}_{l,i}^{\mathrm{f}}(\tau_l; W_{\mathrm{f}}, I_{\mathrm{f}i})$ and $\tilde{\boldsymbol{\gamma}}_{l,i}^{\mathrm{d}}(\psi_l; W_{\mathrm{d}i}, I_{\mathrm{d}})$ are related to the sub-band. However, if we have the same number of sampled frequencies Q_i for all sub-bands, only the approximated projection $\tilde{\boldsymbol{\gamma}}_{l,i}^{\mathrm{d}}(\psi_l; W_{\mathrm{d}i}, I_{\mathrm{d}})$ in space is related to the sub-band. Finally, the relevant $H_{\mathrm{DPS}}^{(D)}[q, \mathbf{u}_n]$ in the entire frequency range can be obtained

$$H_{\mathrm{DPS}}[q, \mathbf{u}_n] = \left[H_{\mathrm{DPS}}^{(D_1)}[q_1, \mathbf{u}_n]^{\mathrm{T}}\ H_{\mathrm{DPS}}^{(D_2)}[q_2, \mathbf{u}_n]^{\mathrm{T}} \cdots\ H_{\mathrm{DPS}}^{(D_I)}[q_{\mathcal{I}}, \mathbf{u}_n]^{\mathrm{T}}\right]^{\mathrm{T}}. \tag{4.35}$$

4.4.3 Simulation Procedure

In order to show the performance of the proposed algorithm, a typical indoor scenario is generated according to the measurement description in [88]. Moreover, we consider two antennas with different radiation patterns in the evaluation: i) a discone antenna [103] and ii) an omnidirectional antenna at both the Tx and the Rx side, respectively.

4.4.3.1 Simulation Configuration

A 3-D view of the scenario is shown in Fig. 4.13, whose dimensions are 5.7 m × 5 m × 2.6 m. It consists of a concrete floor and ceiling, concrete walls, a wooden door, glass windows, as well as metallic and wooden furniture. Different materials are sketched with different colors in Fig. 4.13. The dielectric parameters can be found in [88]: $\varepsilon_r = 9$ and $\sigma = 0.01$ S/m for concrete blocks, $\varepsilon_r = 13$ and $\sigma = 10^{-5}$ S/m for wood blocks, and $\varepsilon_r = 7.6$ and $\sigma = 10^{-12}$ S/m for glass blocks, respectively. Moreover, we treat the metallic cabinet as a PEC. The location of the Tx antenna is fixed, whose coordinate is $\mathbf{u}_{\mathrm{Tx}} = [0.775\ 2.755\ 1.35]^{\mathrm{T}}$ m. The Rx antenna is placed linearly at $N = 200$ positions seen from the lower right corner of Fig. 4.13. The initial coordinate of the Rx is $\mathbf{u}_0 = [3.08\ 2.73\ 1.35]^{\mathrm{T}}$ m. We consider a fixed Rx antenna height, so that the spatial resolution vector is set as $\mathbf{d}_{\mathrm{S}} = [\frac{\sqrt{2}}{2}\ \frac{\sqrt{2}}{2}\ 0]^{\mathrm{T}}$ mm, resulting in Rx antenna separation of $\|\mathbf{d}_{\mathrm{S}}\| = 1$ mm. A close-up view of the Rx positions is included in Fig. 4.13 (b). A few exemplary propagation paths are visualized in Fig. 4.13 for the Rx position $\mathbf{u}_0$. In the simulation, we consider the propagation mechanisms including LOS, up to the fourth-order reflections, penetration, single-order diffraction and diffuse scattering. Note that penetration is embedded in all other mechanisms.

The frequency range is from 3.1 GHz to 10.6 GHz with a frequency resolution of $f_{\mathrm{S}} = 4.6875$ MHz. We divide the entire bandwidth of 7.5 GHz into $\mathcal{I} = 16$ sub-bands with a bandwidth $B_i = 468.75$ MHz. Note that $Q_i = 100$ for all sub-bands. Thus, the corresponding calculation of the subspace dimension $\boldsymbol{V_i}(W_{\mathrm{f}}, I_{\mathrm{f}i})$ and its relevant basis coefficients $\tilde{\boldsymbol{\gamma}}^{\mathrm{f}}_{l,i}(\tau_l; W_{\mathrm{f}}, I_{\mathrm{f}i})$ in frequency need to be performed only once. In the following analysis, the low-complexity SDRT algorithm is used as reference. There are $L = 60945$ propagation paths obtained based on low-complexity SDRT at the first sub-band B_1 of the initial position $\mathbf{u}_0$.

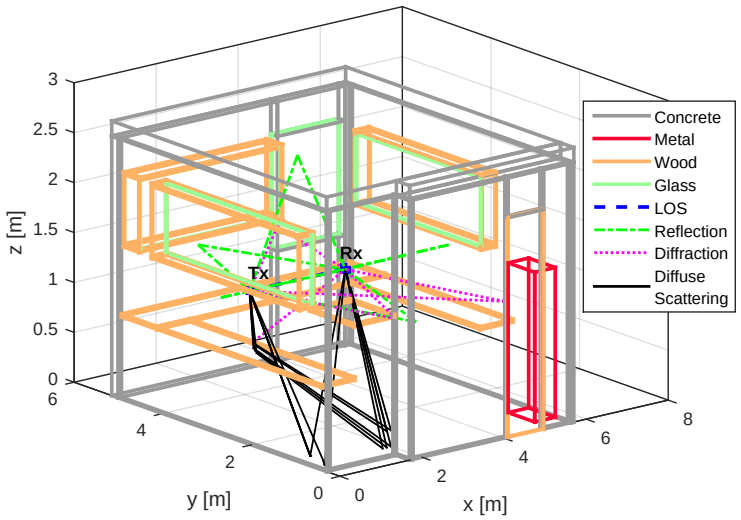

(a) 3D view

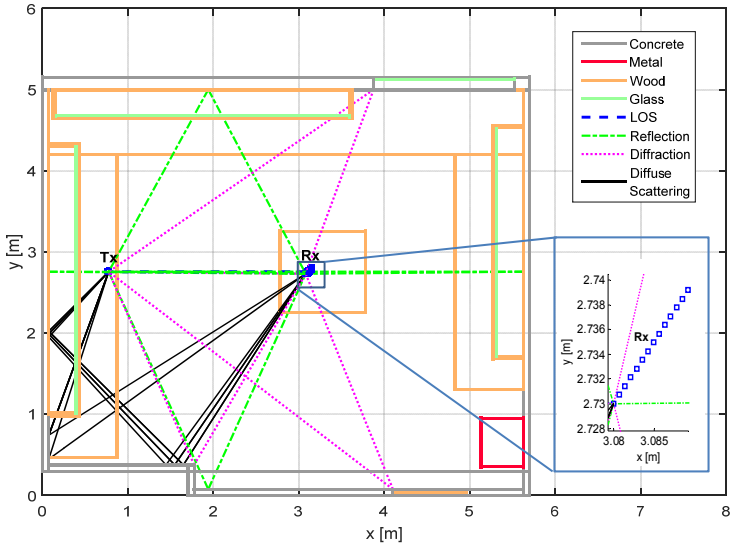

(b) 2D view

Figure 4.13: Pictorial view of the RT scenario considering one Rx position from the grid. (a) 3D view. (b) 2D view, including a close-up view of the Rx positions.

4.4.3.2 MSE Comparison

The MSE of the CTFs between low-complexity SDRT and the DPS subspace algorithm can be calculated as (4.36)

$$\mathrm{MSE}[\mathbf{u}_n] = \frac{\sum_q |H_{\mathrm{SDRT}}[q, \mathbf{u}_n] - H_{\mathrm{DPS}}[q, \mathbf{u}_n]|^2}{\sum_q |H_{\mathrm{SDRT}}[q, \mathbf{u}_n]|^2}. \tag{4.36}$$

The MSE between the remaining algorithms can be calculated in the same way. Note that the low-complexity SDRT assumes that the random phases of diffuse scattering paths are drawn independently for each Rx position, while the PRA and DPS algorithms initialize the relevant phases from Rx position $\mathbf{u}_0$. Thus, in order to avoid the influences from the random phases of diffuse scattering paths, we only consider the deterministic paths to obtain the associated MSE[$\mathbf{u}_n$] results. The relevant results are shown in Fig. 4.14, which includes two different antenna cases. It can be noticed

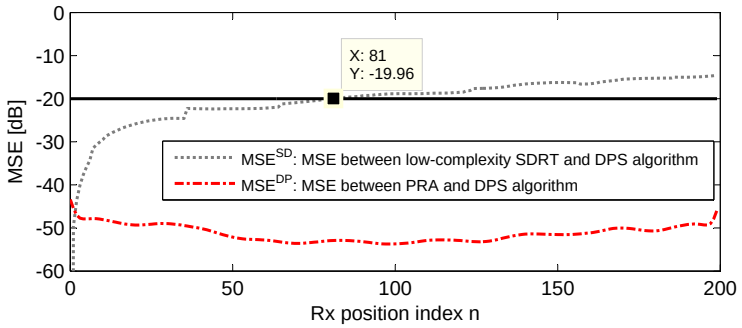

(a) Discone antenna

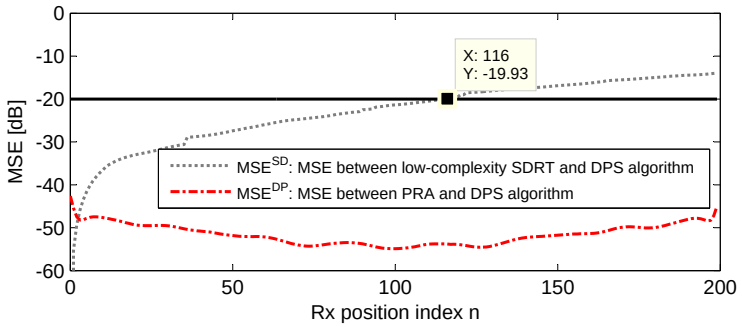

(b) Omnidirectional antenna

Figure 4.14: MSE of CTFs based on three algorithms, which only consider the deterministic paths, at the same Rx positions.

that the MSE values between the PRA and DPS algorithms are always smaller than $-45\,\mathrm{dB}$ for both antenna cases. This confirms that the approximation of the DPS subspace algorithm is as good as the PRA algorithm.

We can observe a jump in the MSE values at the Rx position $\mathbf{u}_{36}$ for both antenna cases. We find at the Rx position $\mathbf{u}_{36}$ in comparison to the Rx positions $\mathbf{u}_{\{n\leq 35\}}$ two additional deterministic components in the low-complexity SDRT algorithm. These components are obviously not included in the PRA and DPS algorithms, which leads to the jump in the MSE.

We set the acceptable error threshold to $\mathrm{MSE}_{\mathrm{thr}} = -20\,\mathrm{dB}$, which indicates how

accurate the proposed DPS algorithm is expected to be. With both antenna cases, the MSE between the RT and DPS subspace algorithm increases steadily along all Rx positions. For the discone antenna case, the MSE keeps smaller than $-20\,\mathrm{dB}$ until the Rx position $\mathbf{u}_{80}$. While for the omnidirectional antenna case, the MSE starts to exceed $-20\,\mathrm{dB}$ from the Rx position $\mathbf{u}_{116}$. It can be concluded that the antenna radiation pattern can influence the accuracy of the proposed DPS algorithm. In order to make the relevant results comparable, the considered maximum number of Rx positions is set to $N = 81$ for the remainder of this paper, which is equal to $8\,\mathrm{cm}$[1].

4.4.3.3 RMS Delay Spread Comparison

In Fig. 4.15, the RMS delay spread τ_{RMS} is shown for the three SDRT implementations and the two antenna configurations. It can be observed from Fig. 4.15 that

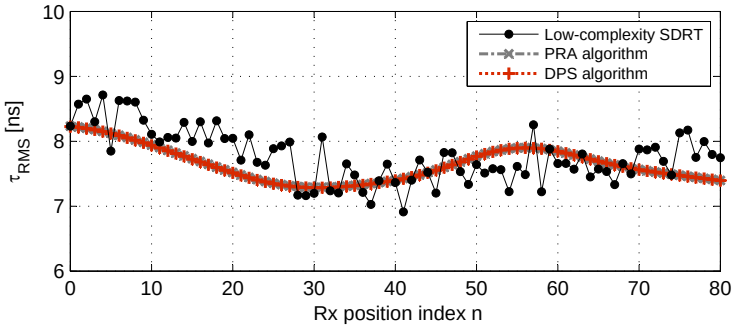

(a) Discone antenna

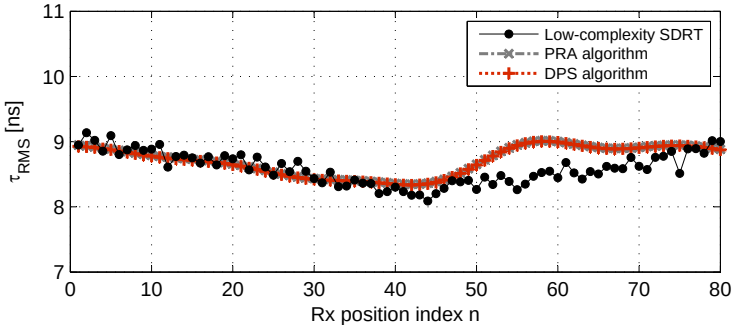

(b) Omnidirectional antenna

Figure 4.15: Comparison of RMS delay spread τ_{RMS} based on three algorithms at the same Rx positions.

[1]If the environment is larger, resulting in interactions to be further away and the plane wave assumptions to be better fulfilled, the MSE would increase slower and the maximum possible 'N' under the threshold would be larger.

Table 4.1: Computation Time

Algorithms	SDRT [h]	PRA [h]	DPS [h]
Computation time	6.78	0.078	0.012

the τ_{RMS} values based on low-complexity SDRT fluctuate. The τ_{RMS} values do not fluctuate for the PRA and DPS cases, but evolve rather smoothly. This is related to the random phases of the diffuse scattering paths, please refer to Section 4.4.3.2 for the detailed explanation. It also can be seen that the τ_{RMS} values for the PRA and DPS algorithm are practically identical. For the discone antenna case, the τ_{RMS} differences between low-complexity SDRT and the DPS algorithm is always smaller than 1 ns along all Rx positions, while for the omnidirectional antenna case, it is always smaller than 0.5 ns along all Rx positions. This is mainly caused by the antenna elevation pattern. It can be concluded that the antenna radiation pattern influences the RMS delay spread as well, however to a smaller degree.

4.4.3.4 Computation Time Comparison

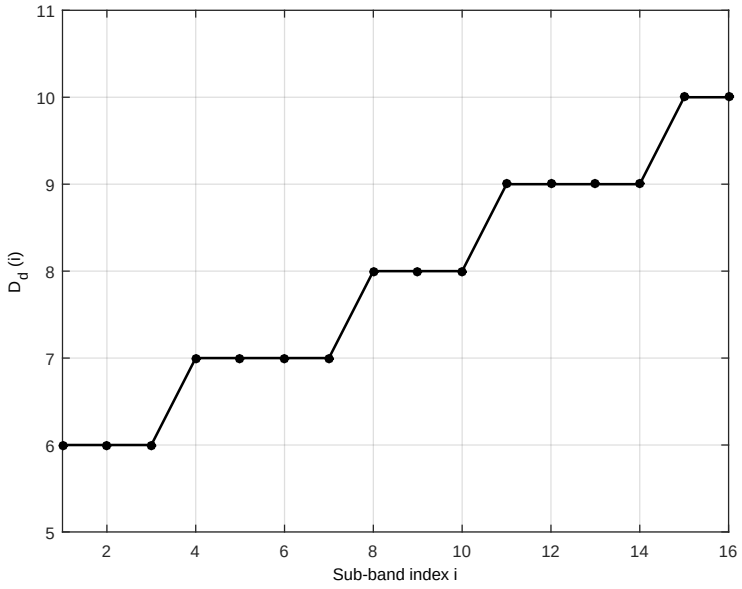

Figure 4.16: Subspace dimension $D_{\mathrm{d}}(i)$ in space.

The computation time comparison (2.4 GHz Intel Core i7 CPU with 8 GB RAM) based on the three considered low-complexity algorithms are presented in Table 4.1. The common simulation time of 0.086 h of RT for all three algorithms per-

formed at one sub-band at the initial Rx position $\mathbf{u}_0$ is not included. Note that the computation time is the same for both antenna configurations. Compared to low-complexity SDRT, the computation time can be reduced by a factor of $(6.78 + 0.086)/(0.012 + 0.086) = 70.06$ when using the DPS algorithm. While compared to the PRA algorithm, without considering the simulation time of RT performed at one sub-band at the initial Rx position $\mathbf{u}_0$, the corresponding reduction factor is about 6.5.

The essential subspace dimensions in frequency and space are the same for both antennas, respectively. The essential subspace dimension in frequency is $D_\mathrm{f} = 74$ for all sub-bands, while in space $D_\mathrm{d}(i)$ varies for different sub-bands. $D_\mathrm{d}(i)$ is shown in Fig. 4.16. It is evident that the subspace dimension in frequency is always smaller than the number of frequency samples in each sub-band. In addition, the dimension in space at different sub-bands is always smaller than the number of Rx positions. Therefore, we reduce the computation time with the DPS subspace algorithm. The proposed DPS subspace algorithm reduces the computation time by more than one order of magnitude compared to low-complexity SDRT.

5 Ray Tracing for Tunnel Scenarios

It is well-known that the radio wave propagation mechanisms inside tunnels are different from the typical outdoor and indoor situations. Since the tunnels represent a significant type of vehicular environments, understanding the channel characteristics for the in-tunnel scenario is crucial for ITS design. A widely used tool for simulating channel characteristics for outdoor and indoor scenarios is a deterministic propagation prediction tool, known as RT. However, RT applied for tunnel scenarios has not been studied adequately.

In this chapter, we firstly introduce in-tunnel measurements and their relevant time-varying analysis. Moreover, we present a low-complexity RT algorithm for tunnel scenarios by combining an approximated RT with higher-order reflection algorithm as the first step. Furthermore, a hybrid ray and graph method to simulate the in-tunnel time-variant V2V propagation channel is proposed as the second step.

5.1 Background

The performance and efficiency of ITS depend strongly on wireless communication systems. V2V wireless communications have received a lot of interest from both academia and vehicle industry. The development of suitable communication standards requires an adequate understanding of the V2V propagation channel. Due to fast changing propagation conditions, including geometries, variable vehicle speeds and a relatively low height of the Tx and the Rx antennas, the V2V propagation channel differs significantly from typical channels observed in cellular networks [58,104]. Moreover, the semi-enclosed in-tunnel scenario leads to V2V radio propagation characteristics that are different from typical situations. Full comprehension of the channel behavior in-tunnel is of great importance for ITS to improve the safety in tunnel scenarios, for instance by lane change assistance, cooperative forward collision warning, or slow vehicle warning, among others [105]. Furthermore, it is obvious that the reliability of the radio-link depends strongly on propagation mechanisms. Therefore, effective channel prediction tools and models are required for the development of suitable communication systems and standards.

Several theoretical and experimental studies for analyzing propagation of VHF

and UHF radio signals in tunnels have been summarized in [106, 107]. Channel models describing the propagation characteristics in tunnels are divided into deterministic and empirical channel models: (i) deterministic channel models include ray-based approaches [108–112], waveguide models [113–115] and numerical methods for solving Maxwell equations [116, 117], and (ii) typical representatives of an empirical channel model is the two-slope channel model [114,118]. We are interested in modeling the in-tunnel time-variant V2V propagation channel by RT. However, the accuracy of RT depends on a precise description of the propagation environment, which leads to high computational complexity. Due to this reason, a simplified RT tool is used in most of the published work to study the behavior of radio wave propagation in empty tunnels. Furthermore, due to the fast changing propagation conditions, vehicular communication channels are always characterized by a non-stationary time- and frequency-selective fading process. This requires a more efficient channel model to describe the V2V propagation channel.

In addition, it is important to validate the channel model by comparing the relevant results with measurements. However, there are only few published studies of in-tunnel V2V channel measurements [111, 119–122], most of which consider only infrastructure-to-vehicle communications and do not use the carrier frequency dedicated for ITS. Few in-tunnel channel measurements for 5.8 GHz can be found in [105, 120, 123], where a significant contribution from the dense multipath component along with a strong LOS component can be observed. In fact, these dense multipath components are mainly caused by high-order reflection paths [108]. Therefore, we propose a low-complexity RT algorithm for tunnel scenarios by combining RT with an approximated higher-order reflection algorithm. The approximated higher-order reflection algorithm only depends on the width and height of the tunnel, and the Tx and Rx positions. Therefore, the obtained propagation paths are the same at any time snapshot when the environment keeps constant.

It can be seen that the power of the dense multipath component drops off exponentially with increasing delay in the early part of the CIR. We denote the dense multipath component as the "reflection tail". Therefore, we introduce the concept of reverberant radio channels by propagation graphs [124] in our work. The recursive structure of the graph allows for a computationally efficient simulation of an infinite number of bounces and represents the reflection tail well. In addition, small or irregular shaped objects, such as traffic signs and the ventilation system, are difficult to be modeled by RT. These kind of objects are always approximated as perpendicular parallelepiped in our RT tool. Thus, we generate discrete scatterers on those small or irregular shaped objects based on the geometrical information of the scenario. This resembles the concept of a GSCM. The proposed propagation graph can easily

integrate these scatterer contributions. The aforementioned considerations motivate our interest in designing a hybrid ray and graph method to simulate the in-tunnel time-variant V2V propagation channel.

5.2 In-Tunnel Measurements and Time-Varying Analysis

The measurements used in the present work were collected in the DRIVEWAY'09 measurement campaign [119] in the Øresund tunnel connecting Denmark and Sweden. The observed fading process of the V2V channel is non-stationary [119]. The LSF is a useful quantity for characterizing non-stationary time-variant channels, which is a short-term representation of the power spectrum of the observed fading process [105].

5.2.1 In-Tunnel Measurements

The measurement starts when the Tx driving in front of the Rx enters the tunnel. At $t = 2\,\mathrm{s}$ enters the Rx the tunnel, see Fig. 5.2. The picture in Fig. 5.1 is taken from the video of the measurements when both, the Tx- and the Rx-vehicle, are inside the tunnel. The distance between both vehicles is about $d = 120\,\mathrm{m}$ and

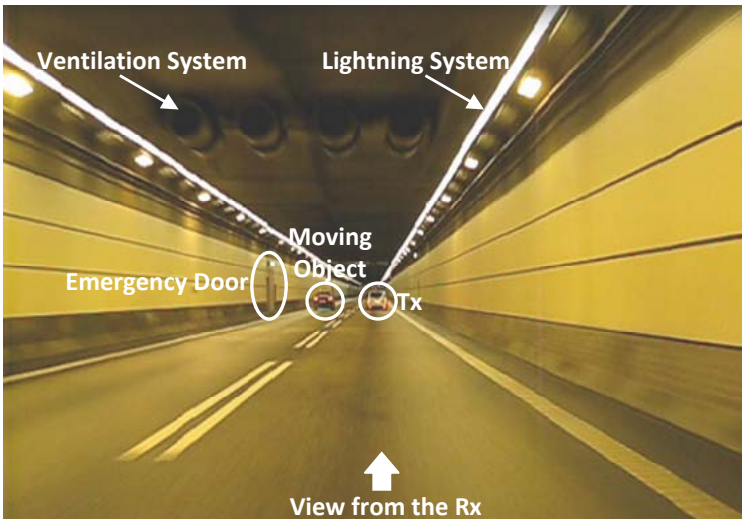

Figure 5.1: Video snapshot representing measurement environment.

their speed is kept constant at $v_{\mathrm{Rx}} = v_{\mathrm{Tx}} = 105\,\mathrm{km/h}$ for the whole measurement

time interval. Both the Tx- and the Rx-vehicle are equipped with an antenna array consisting of 4 elements that is placed on the roof-top of the vehicle. Moreover, each element is mainly radiating in one of four directions: left, right, back and front, thus the antenna array covers 360° in the azimuth plane. The CTF $H(t, f)$ is measured over a time interval of $T = 10\,\mathrm{s}$, with a time resolution of $t_\mathrm{s} = 307.2\,\mu\mathrm{s}$. In total, there are $S = 32000$ time snapshots. There are $Q = 769$ total frequency bins in the measurement bandwidth of $B = 240\,\mathrm{MHz}$, where the carrier frequency $f_\mathrm{c} = 5.6\,\mathrm{GHz}$. This results in a resolution in frequency domain of $f_\mathrm{s} = B/Q$. We denote the sampled time-varying CTF as

$$H_\iota[m, q] \triangleq H_\iota(t, f) \triangleq H_\iota(mt_\mathrm{s}, qf_\mathrm{s}), \tag{5.1}$$

where $\iota \in \{1, \cdots, \mathcal{L}\}$ is the link index, $\mathcal{L} = 16$ for our case, $m \in \{0, \cdots, S-1\}$ is the snapshot index and $q \in \{-\lfloor \frac{Q}{2} \rfloor, \ldots, \lfloor \frac{Q}{2} \rfloor - 1\}$ is the sampled frequency index. Note that $qf_\mathrm{s} \in [-B/2, B/2]$. In order to resemble an omnidirectional antenna radiation pattern, the CTF can be expressed as

$$H[m, q] = \frac{1}{\mathcal{L}} \sum_{\iota=1}^{\mathcal{L}} H_\iota[m, q]. \tag{5.2}$$

5.2.2 LSF Based Measurements Analysis

The observed fading process of the V2V channel is non-stationary [119]. The LSF, a short-term representation of the power spectrum of the observed fading process, is a useful tool for characterizing non-stationary time-variant channels [105]. We assume the fading process is locally stationary within a stationary region with size $M \times N$ samples in time and frequency, respectively. In order to calculate the LSF for consecutive stationary regions, the time index of each stationary region $k_\mathrm{t} \in \{1, \cdots, \lfloor S/M \rfloor\}$ and the frequency index of each stationary region $k_\mathrm{f} \in \{1, \cdots, \lfloor Q/N \rfloor\}$ are defined. The estimate of the discrete LSF is denoted as [125], [126]

$$\hat{\mathcal{C}}[k_\mathrm{t}, k_\mathrm{f}; n, p] = \frac{1}{IJ} \sum_{w=0}^{IJ-1} \left| \mathcal{H}^{(\mathbf{G}_w)}[k_\mathrm{t}, k_\mathrm{f}; n, p] \right|^2, \tag{5.3}$$

where $n \in \{0, \cdots, N-1\}$ denotes the delay index, $p \in \{-M/2, \cdots M/2 - 1\}$ the Doppler index, I is the number of orthogonal time-domain tapers, J is the number of orthogonal frequency-domain tapers, and w is the parameter of the windowed frequency response $\mathcal{H}^{(\mathbf{G}_w)}[k_\mathrm{t}, k_\mathrm{f}; n, p]$. The windowed frequency response reads [104]

$$\mathcal{H}^{(\mathbf{G}_w)}[k_\mathrm{t}, k_\mathrm{f}; n, p] = \sum_{m'=-M/2}^{M/2-1} \sum_{q'=-N/2}^{N/2-1} H[m' - k_\mathrm{t}, q' - k_\mathrm{f}] G_w[m', q'] e^{-j2\pi(pm' - nq')}, \tag{5.4}$$

where the window functions $G_w[m', q']$ shall be well localized within the support region $[-M/2, M/2-1] \times [-N/2, N/2-1]$.

The parameters selected for analyzing the measurements are $M = 128$ and $N = 769$, which results in a stationary region of 40 ms × 240 MHz. Note that we assume the channel is stationary over the total measured bandwidth. These parameters are the same as the ones used in [127]. Thus, the obtained resolutions are $t_\mathrm{s} = 307.2\,\mu$s in time domain, $f_\mathrm{s} = 312.09$ kHz in frequency domain, $\tau_\mathrm{s} = Q/(BN) = 1/B = 4.17$ ns in delay domain, and $\nu_\mathrm{s} = 1/(t_\mathrm{s}M) = 25.43$ Hz in Doppler domain, respectively.

Based on the LSF $\hat{\mathcal{C}}[k_\mathrm{t}, k_\mathrm{f}; n, p]$, the time-varying PDP and time-varying Doppler power spectral density (DSD) can be calculated by projecting the LSF in the delay and Doppler domain, respectively. They are defined as

$$\begin{aligned}\hat{P}_\tau[k_\mathrm{t}, k_\mathrm{f}; n] &= E_p\{\hat{\mathcal{C}}[k_\mathrm{t}, k_\mathrm{f}; n, p]\} \\ &= \frac{1}{M}\sum_{p=-M/2}^{M/2-1} \hat{\mathcal{C}}[k_\mathrm{t}, k_\mathrm{f}; n, p]\end{aligned} \tag{5.5}$$

and

$$\begin{aligned}\hat{P}_\nu[k_\mathrm{t}, k_\mathrm{f}; p] &= E_n\{\hat{\mathcal{C}}[k_\mathrm{t}, k_\mathrm{f}; n, p]\} \\ &= \frac{1}{N}\sum_{n=0}^{N-1} \hat{\mathcal{C}}[k_\mathrm{t}, k_\mathrm{f}; n, p],\end{aligned} \tag{5.6}$$

where $E_x\{\cdot\}$ denotes expectation over the variable x.

The time-varying PDP and DSD, shown in Fig. 5.2(a) and Fig. 5.2(b), are calculated according to (5.5) and (5.6). There are $K_\mathrm{t} = S/M = 250$ stationary time regions over a time interval of $T = 10$ s and $K_\mathrm{f} = Q/N = 1$ stationary frequency region over the bandwidth $B = 240$ MHz. Multiple signal components parallel to the direct LOS component are presented in Fig. 5.2, which are mainly caused by the higher-order reflections from the tunnel walls, ceiling and floor. Besides these significant contributions in the PDP, the components from objects inside the tunnel are also visible.

5.3 Tunnel RT Algorithm

RT in this work has been accelerated by using MEX functions. Moreover, the reflection algorithm has been improved by efficient implementation of finding reflection paths as described in Section 3.1.2. Despite of this, the computational complexity,

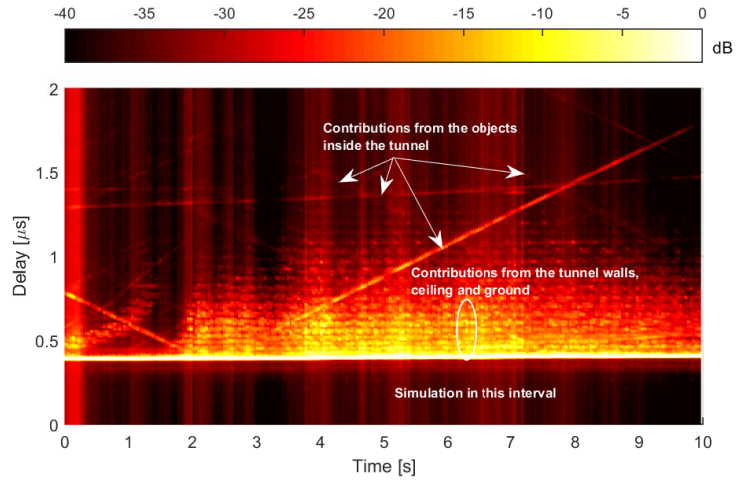

(a) Time-varying PDP

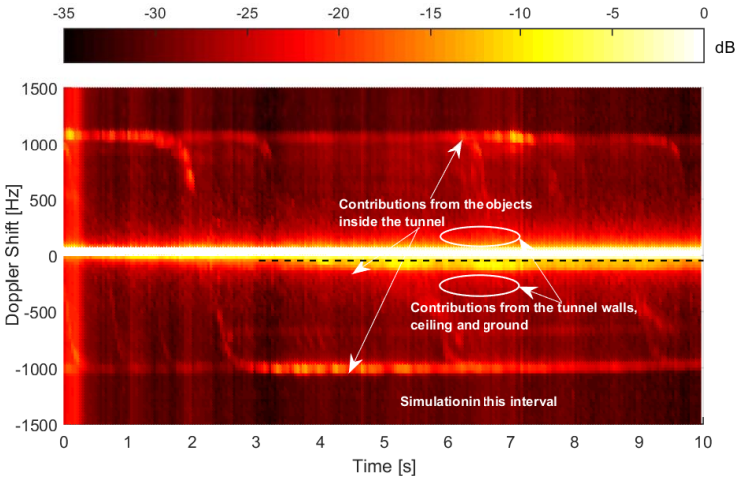

(b) Time-varying DSD

Figure 5.2: Normalized time-varying PDP and DSD measured over interval of $T = 10\,\mathrm{s}$.

involved in the backtracking procedure, is tremendously increased due to the higher-order reflection case. Therefore, we combine an approximate higher-order reflection algorithm with the RT algorithm.

5.3.1 Approximate Higher-order Reflection Algorithm

This algorithm does not consider the objects inside the tunnel, so that the tunnel is treated as an equivalent rectangle [128]. The input for the algorithm includes the positions of Tx and Rx, the width $2a$ and the height $2b$ of the tunnel, as well as

the permittivity and conductivity of the vertical and horizontal walls. An example of the set of reflection images of the Tx on the excitation plane are shown in Fig. 5.3. The origin of the coordinate system is located at the center of the rectangular tunnel. The propagation paths related to image $I_{p,q}$ experiences $|p|$ times vertical reflections and $|q|$ times horizontal reflections. Regardless of the reflection order, the incidence angles on the vertical and horizontal walls, β_v and α_h, remain the same for a certain path.

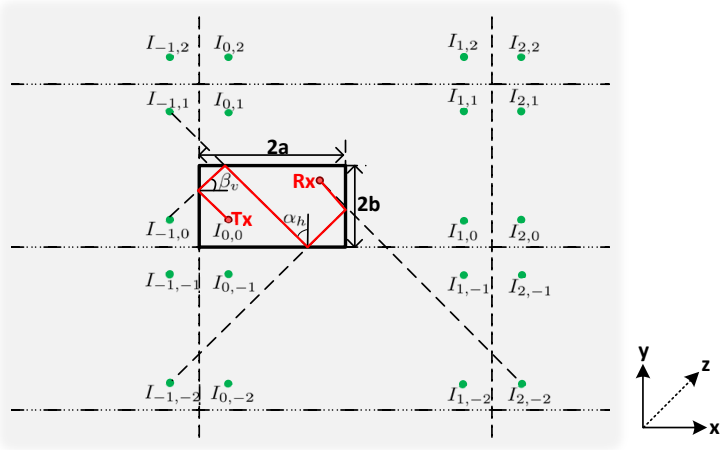

Figure 5.3: An example of the set of images within the tunnel.

For a Tx positioned at (x_0, y_0, z_0), the coordinate $(x_\mathrm{i}, y_\mathrm{i}, z_\mathrm{i})$ of the image point $I_{p,q}$ can be calculated as

$$\begin{cases} x_\mathrm{i} = 2a \cdot p \pm x_0, \\ y_\mathrm{i} = 2b \cdot q \pm y_0, \\ z_\mathrm{i} = z_0, \end{cases} \tag{5.7}$$

where the positive sign is selected if p or q is even while the negative sign is selected if p or q is odd. The Tx and Rx antennas used for the RT simulation are vertical half-wave dipole antennas in the present work. The electric field for a single order reflection component, can be expressed as

$$E_\mathrm{href} = [\bar{g}^\mathrm{R}_\mathrm{href}(f_\mathrm{c})]^* \cdot \overline{\overline{\mathbf{R}}}_\mathrm{href}(f_\mathrm{c}) \cdot \bar{g}^\mathrm{E}_\mathrm{href} \frac{e^{-j2\pi f_\mathrm{c} r_{p,q}/c}}{r_{p,q}} \bar{E}_0, \tag{5.8}$$

where $\overline{\overline{\mathbf{R}}}_\mathrm{href} = R_\parallel^{|q|} \cdot R_\perp^{|p|}$ is the reflection coefficient, $R_\parallel$ and $R_\perp$ are the perpendicular and parallel polarization coefficients, which can be calculated according to (2.11) and (2.12), and $r_{p,q}$ is the distance between the image point $I_{p,q}$ and the Rx, which is equal to the total length of the propagation path between the Tx and the Rx.

Compared to the reflection algorithm in RT, the approximate higher-order reflection algorithm requires no backtracking procedure. Based on the visibility procedure, all relevant information for the path calculation can be easily obtained. Therefore, we propose a hybrid approach by combining this higher-order reflection algorithm with RT to predict the propagation channel in real tunnels. Note that the effective subdivision algorithm has been applied for the diffuse scattering algorithm as introduced in Section 3.2.1. Due to the high computational complexity of RT, we limit the simulation of the CIR to 1 s, corresponding to $t = 7.5\,\mathrm{s}, \ldots, 8.5\,\mathrm{s}$ in the measurements, in the following analysis.

5.3.2 Analysis of Time-Varying PDP

The 3D and 2D view of the tunnel scenario used for RT is illustrated in Fig. 5.4, where the different materials are sketched with different colors. It should be noted that we do not have the detailed description of the tunnel. The dimensions of the tunnel and the objects inside are found in [129] and in the video of the measurements. Each block is modeled as a perpendicular parallelepiped and the moving object is also included by our RT tool. The width is $2a = 11.65\,\mathrm{m}$ and the height is $2b = 6.93\,\mathrm{m}$, while the considered length is 586 m. It should be noted that the length of the tunnel is longer than the considered length. The reason is that the propagation paths from the deeper inside of the tunnel, most likely coming from diffuse scattering, would contain very low power, but would result in extremely high computational complexity. The dielectric properties are included in the input database of RT, in which the metallic block is assumed as a PEC. The values of relative permittivity ε_r and the conductivity σ of the materials are: $\varepsilon_{r,\mathbf{c}} = 8.92$ and $\sigma_{\mathbf{c}} = 0.046\,\mathrm{S/m}$ for concrete blocks, and $\varepsilon_{r,\mathbf{g}} = 3.7$ and $\sigma_{\mathbf{g}} = 0\,\mathrm{S/m}$ for glass blocks [63]. According to the simulation parameters, dS is $1.23\,\mathrm{m}^2$ for the proposed subdivision algorithm based on (3.6). The Tx and the Rx antennas used for the RT simulation are half-wave dipole antennas.

RT takes into account the following propagation mechanisms: LOS, reflection up to the fourth order, single-order diffraction, single bounce scattering, scattering-reflection and reflection scattering cases. Penetration has been embedded into all other mechanisms. Some propagation paths are visualized in Fig. 5.4. For the approximate higher-order reflection paths, the vertical reflection order $|p|$ and horizontal reflection order $|q|$ satisfy the relationship as $4 \leq |p| + |q| \leq 40$. We assume that components with reflection order larger than 40 can be neglected as shown in [130]. In order to make the simulation results comparable to the measurements, RT is performed at $N = 3200$ time snapshots in a time interval of $T = 1\,\mathrm{s}$. The

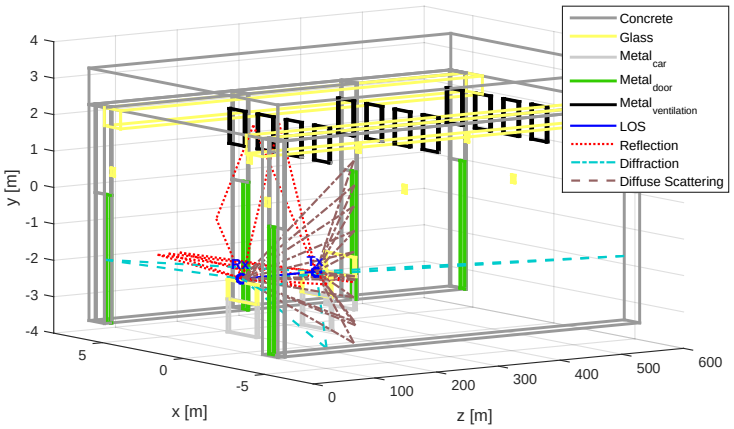

(a) 3D view

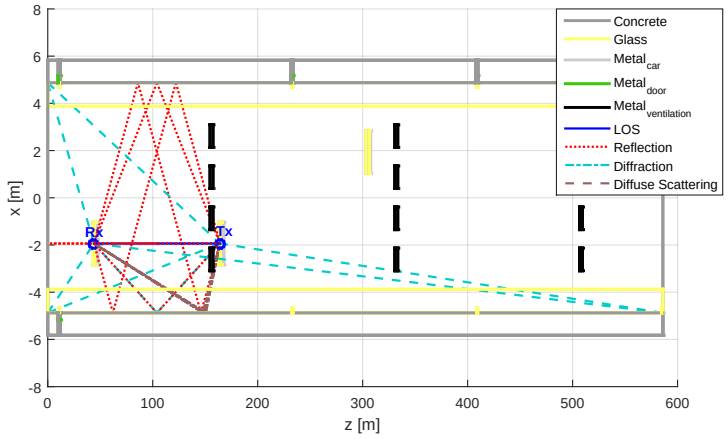

(b) 2D view

Figure 5.4: Pictorial view of the RT tunnel scenario. (a) 3D view. (b) 2D view.

simulation time of the tunnel RT for one snapshot is about 407 s (2.4GHz Intel Core i7 CPU with 8GB RAM). Furthermore, $K_{\mathrm{t}} = 25$ stationary time regions over the time interval $T = 1\,\mathrm{s}$ are used for the time-varying PDP analysis.

It is noteworthy that we do not involve the LSF in the following time-varying PDP. We average all obtained CIRs within each time stationary region directly. The normalized time-varying PDP $\hat{P}[k_{\mathrm{t}}; n]$ of the tunnel RT algorithm is shown in Fig. 5.5. The contributions from the objects inside the tunnel can be observed clearly. To clarify, we focus here at one time snapshot and compare the time-varying PDPs at stationary time region $k_{\mathrm{t}} = 20$, where $k_{\mathrm{RT,t}} \in \{0, \ldots, K_{\mathrm{t}} - 1\}$ denotes the stationary time region index. The results are shown in Fig. 5.6. From Fig. 5.6 (a), it can be seen that the normalized PDPs based on measurements and the tunnel RT algorithm are comparable to each other. Note that the normalized PDP based

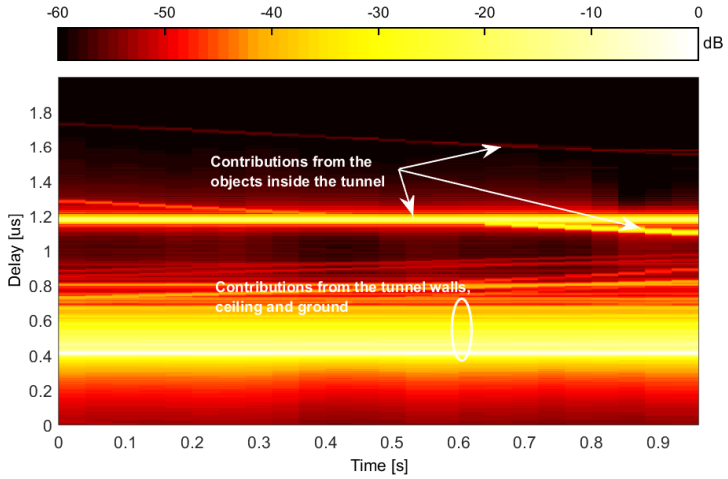

Figure 5.5: Time-varying PDP simulated with the tunnel RT algorithm for time interval of $T = 1\,\mathrm{s}$.

on the measurement here is different with the one shown in Fig. 5.2: i) In Fig. 5.6 (a), the PDP is calculated by averaging all CIRs within the stationary time region $k_\mathrm{t} = 20$, and ii) in Fig. 5.2, the PDPs is obtained based on the LSF. The peaks appearing between $1\,\mu\mathrm{s}$ and $1.5\,\mu\mathrm{s}$, marked by the red arrows, are mainly caused by the moving object and the ventilation system. The shifts in the delay domain and the imprecision of the power between the measurements and the tunnel RT are unavoidable in the present work, because the environmental information to the input of RT is not accurate enough. In the lower plots Fig. 5.6 (b)-(d), we analyze the composition of the PDP of the tunnel RT algorithm. Due to the dimension of the tunnel, the considered fourth-order reflection contributions are not enough, shown in Fig. 5.6 (b), which is usually used for typical outdoor and indoor scenarios. In Fig. 5.6 (c), it can be observed that the higher-order reflection components play a more important role in the delay interval $0.45\,\mu\mathrm{s} - 0.75\,\mu\mathrm{s}$, while the diffuse scattering components are more significant after $0.75\,\mu\mathrm{s}$, shown in Fig. 5.6 (d). Moreover, it can be concluded that the diffuse scattering components contain more power when they are close to the specular components.

5.4 Hybrid Model for Tunnel Scenarios

In Fig. 5.5, it can be seen that the obtained higher-order reflection paths are the same at any time stamp when the environment is kept constant. In Fig. 5.6 (c), it can be seen that the power of the higher-order reflection paths drops off exponentially

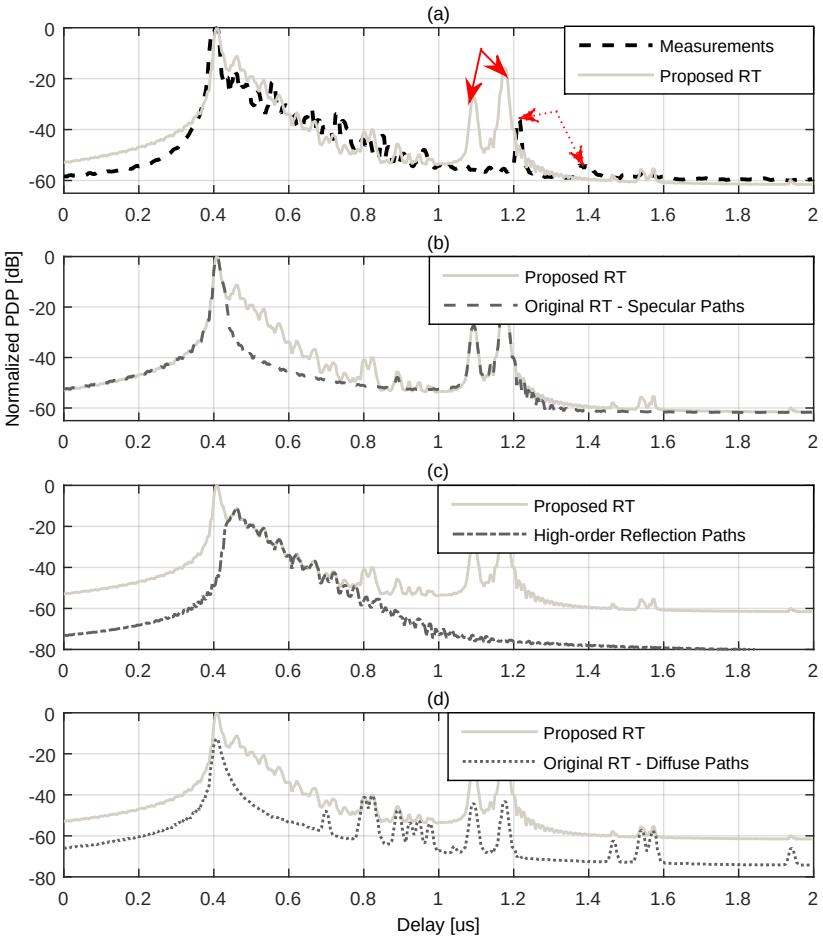

Figure 5.6: Time-varying PDP based on the tunnel RT algorithm at time stamp $k_{\mathrm{t}} = 20$.

with delay in the early part of the PDP. We denote the contribution of the higher-order reflection paths as the "reflection tail". This reflection tail is difficult to be included in RT due to its computational complexity requirements. Moreover, objects with small size or irregular shape are difficult to be described by a RT tool. Furthermore, modeling the time-variant V2V channel by RT requires extremely high computational complexity. Therefore, we propose a hybrid model in this section, which combines RT with the propagation graph. Based on the tunnel measurements analyzed by LSF, we include the time evolution of relevant channel parameters in the proposed model depending on the obtained stationary time region.

5.4.1 Propagation Graphs

The so-called propagation graph is a directed graph, that can be set up according to the propagation scenario. The directed graph $\mathcal{G}$ is defined as a pair $(\mathcal{V}, \mathcal{E})$ of disjoint sets of vertices $\mathcal{V}$ and edges $\mathcal{E}$. The vertex set $\mathcal{V} = \mathcal{V}_{\mathrm{Tx}} \cup \mathcal{V}_{\mathrm{Rx}} \cup \mathcal{V}_{\mathrm{S}}$ represents a union of the set of Txs (in $\mathcal{V}_{\mathrm{Tx}}$), the set of Rxs (in $\mathcal{V}_{\mathrm{Rx}}$) and the set of scatterers (in $\mathcal{V}_{\mathrm{S}}$). The edge set $\mathcal{E}$ can be partitioned into four subsets as $\mathcal{E}_{\mathrm{TR}}$ the set of Tx-Rx edges, $\mathcal{E}_{\mathrm{TS}}$ Tx-scatterer edges, $\mathcal{E}_{\mathrm{SR}}$ scatterer-Rx edges, and $\mathcal{E}_{\mathrm{SS}}$ scatterer-scatterer edges. The signals propagate via the edges of the directed graph. Each Tx vertex emits a signal via the outgoing edges, while a Rx vertex sums up the signals arriving via the ingoing edges. A scatterer vertex sums up the signals on its ingoing edges and re-emits this on its outgoing edges. Fig. 5.7 shows an example propagation graph with four Tx vertices, three Rx vertices and seven scatterer vertices.

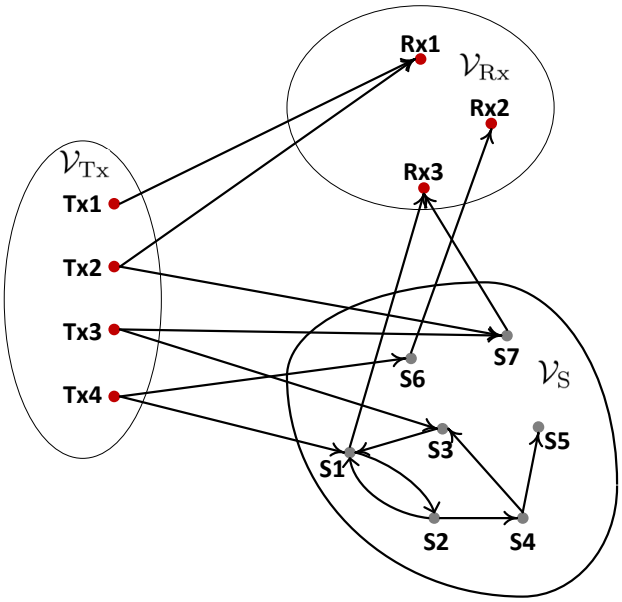

$$\mathcal{E}_{\mathrm{TR}} = \{(\mathrm{Tx1}, \mathrm{Rx1}), (\mathrm{Tx2}, \mathrm{Rx1})\}$$

$$\mathcal{E}_{\mathrm{TS}} = \{(\mathrm{Tx2}, \mathrm{S7}), (\mathrm{Tx3}, \mathrm{S3}), (\mathrm{Tx3}, \mathrm{S7}), (\mathrm{Tx4}, \mathrm{S1}), (\mathrm{Tx4}, \mathrm{S6})\}$$

$$\mathcal{E}_{\mathrm{SR}} = \{(\mathrm{S1}, \mathrm{Rx3}), (\mathrm{S6}, \mathrm{Rx2}), (\mathrm{S7}, \mathrm{Rx3})\}$$

$$\mathcal{E}_{\mathrm{SS}} = \{(\mathrm{S1}, \mathrm{S2}), (\mathrm{S2}, \mathrm{S1}), (\mathrm{S3}, \mathrm{S1}), (\mathrm{S2}, \mathrm{S4}), (\mathrm{S4}, \mathrm{S3}), (\mathrm{S4}, \mathrm{S5})\}$$

Figure 5.7: An example propagation graph with four Tx vertices, three Rx vertices and seven scatterer vertices.

The weighted adjacency matrix $\mathbf{A}[q] \in \mathbb{C}^{(N_{\mathrm{Tx}}+N_{\mathrm{Rx}}+N_{\mathrm{S}})\times(N_{\mathrm{Tx}}+N_{\mathrm{Rx}}+N_{\mathrm{S}})}$, where N_{Tx},

N_{Rx} and N_{S} are the number of Txs, Rxs and scatterers involved into the propagation graph $\mathcal{G}$, respectively, takes the form [124]

$$\mathbf{A}[q] = \begin{bmatrix} \mathbf{0} & \mathbf{0} & \mathbf{0} \\ \mathbf{D}[q] & \mathbf{0} & \mathbf{R}[q] \\ \mathbf{T}[q] & \mathbf{0} & \mathbf{B}[q] \end{bmatrix}, \tag{5.9}$$

where $\mathbf{0}$ denotes the all-zero matrix of the appropriate dimension and the transfer matrices

$\mathbf{D}[q] \in \mathbb{C}^{N_{\mathrm{Rx}} \times N_{\mathrm{Tx}}}$ connecting $\mathcal{V}_{\mathrm{Tx}}$ to $\mathcal{V}_{\mathrm{Rx}}$,

$\mathbf{R}[q] \in \mathbb{C}^{N_{\mathrm{Rx}} \times N_{\mathrm{S}}}$ connecting $\mathcal{V}_{\mathrm{S}}$ to $\mathcal{V}_{\mathrm{Rx}}$,

$\mathbf{T}[q] \in \mathbb{C}^{N_{\mathrm{S}} \times N_{\mathrm{Tx}}}$ connecting $\mathcal{V}_{\mathrm{Tx}}$ to $\mathcal{V}_{\mathrm{S}}$,

$\mathbf{B}[q] \in \mathbb{C}^{N_{\mathrm{S}} \times N_{\mathrm{S}}}$ interconnecting $\mathcal{V}_{\mathrm{S}}$.

Furthermore, the transfer function $\mathbf{H}_{\mathrm{PG}}[q]$, considering infinite interactions of the propagation path, can be calculated in a closed form as [124]

$$\mathbf{H}_{\mathrm{PG}}[q] = \mathbf{D}[q] + \mathbf{R}[q][\mathbf{I} - \mathbf{B}[q]]^{-1}\mathbf{T}[q], \tag{5.10}$$

An expression for the partial transfer function is also derived in [124]. When accounting for $K-$th or more interactions, the partial transfer function can be obtained as

$$\mathbf{H}_{\mathrm{PG},K:\infty}[q] = \mathbf{R}[q]\mathbf{B}^{K-1}[q][\mathbf{I} - \mathbf{B}[q]]^{-1}\mathbf{T}[q]. \tag{5.11}$$

Comparing both expressions, it can be observed that the full transfer function (5.10) is recovered from $K = 1$ to an unbounded number of interactions and by adding $\mathbf{D}[q]$. This is typical for the case when the reverberation effect occurs. Each element $A_e[q]$ of $\mathbf{A}[q]$, where $e \in \mathcal{E}$, is associated to an edge transfer function. The edge transfer function is defined in Section 5.4.2.

5.4.2 Hybrid Channel Model

We consider a hybrid model, which is a linear system summing up the time-varying CTF obtained from RT and the propagation graph as

$$H_{\mathrm{HY}}[m, q] = H_{\mathrm{RT},0:\mathrm{n_{RT}}}[m, q] + H_{\mathrm{PG},\mathrm{n_{PG}}:\infty}[m, q], \tag{5.12}$$

where $m = (k_{\mathrm{t}} - 1)M + m'$, $k_{\mathrm{t}} \in \{1, \cdots, K_{\mathrm{t}}\}$ and $m' \in \{0, \cdots, M-1\}$ is the time snapshot index for each stationary time region. The CTF $H_{\mathrm{RT},0:\mathrm{n_{RT}}}[m, q]$ computed

by RT contains specular reflections up to the order $\mathrm{n_{RT}}$, penetration, diffraction, and diffuse scattering. The CTF $H_{\mathrm{PG},\mathrm{n_{PG}}:\infty}[m,q]$ computed by the propagation graph includes the partial response from the order $\mathrm{n_{PG}}$ to infinity for calculating the reflection tail and the response related to the contribution from discrete scatterers. This consideration provides a clear contributions from both models. We set $\mathrm{n_{RT}} = 4$ and $\mathrm{n_{PG}} = 2$ in the proposed hybrid model based on a certain path length threshold. Note that this setting does not cause any overlapped paths based on RT and the propagation graph. The detail is discussed in Section 5.4.3. In the following, we use $H_{\mathrm{RT}}[m,q]$ and $H_{\mathrm{PG}}[m,q]$ to express the time-varying CTF based on RT and the propagation graph, respectively. In order to save computational complexity, the time evolution of relevant parameters is considered in the proposed model based on the stationary time region. In the following, we describe how to set the parameters for RT and the propagation graph.

5.4.2.1 Settings for Ray Tracing

In general, the geometric and electromagnetic parameters for RT are given by the considered environment. In theory, we could set the order of interactions of the propagation path as any positive integer. However, the computational complexity of RT limits the order of interactions occurring for each path. For the considered tunnel scenario, the maximum order of a reflection path is $\mathrm{n_{RT}}$. Moreover, we consider single-order diffraction and single-order diffuse scattering contributions. For the time-variant CTF of RT $H_{\mathrm{RT}}[m,q]$, we firstly calculate the RT results at the initial time snapshot $m' = 0$ for each stationary time region k_{t}. Then we use the SoCE algorithm (3.36) to calculate the time-varying CTF $H_{\mathrm{RT}}[m',q]$ for stationary time region k_{t} as

$$H_{\mathrm{RT}}[m',q] = \sum_{l=1}^{L_{\mathrm{RT},k_{\mathrm{t}}}} \eta_l[0] e^{-j2\pi q f_{\mathrm{s}} \tau_l[0]} \cdot e^{j2\pi m' t_{\mathrm{s}} \nu_l[0]}, \tag{5.13}$$

where l is the propagation path index, $L_{\mathrm{RT},k_{\mathrm{t}}}$ is the total number of propagation paths at stationary time region k_{t}, $\eta_l[0]$, $\tau_l[0]$ and $\nu_l[0]$ are the complex-valued weighting coefficient, delay and Doppler shift of the $l-$th path at $m' = 0$ at stationary time region k_{t}, respectively. The Doppler shift at the center frequency f_{c} is given as [131]

$$\nu_l[0] = (|v_{\mathrm{Rx}}| \cos(\phi_l[0]) + |v_{\mathrm{Tx}}| \cos(\beta_l[0])) f_{\mathrm{c}}/c, \tag{5.14}$$

where c is the speed of light, $\phi_l[0]$ is the angle between the moving direction of the Rx and the line connecting the $l-$th interaction point with the Rx and $\beta_l[0]$ is the angle between the moving direction of the Tx and the line connecting the $l-$th interaction

point with the Tx at $m' = 0$ at stationary time region k_t, respectively. Note that we also can use the DPS subspace instead of the SoCE algorithm here. However, we cannot save the computational complexity for the considered scenario due to the time resolution and the frequency resolution in measurements. If the radio propagation occurs in a frame based communication system, the DPS subspace would be a better solution than the SoCE algorithm considering the computational complexity [60].

In order to save simulation time for diffuse scattering paths, a subdivision algorithm based on concentric circles is applied, which significantly reduces the computational complexity of RT with no loss in accuracy [64], see Section 3.2. The proper tile size can be calculated based on (3.6). The diffuse scattering tiles are kept constant for one stationary time region. The complex-valued scattering weighting coefficient $\eta_\ell[0]$, where ℓ is the diffuse scattering tile index, can be calculated by (3.34) and (3.35) as

$$\eta_\ell[0] = \sqrt{|\eta_{\ell_\mathrm{max}}[0]|^2 \cdot \Big(\frac{1+\cos(\varphi_\ell[0])}{2}\Big)^{\alpha_\mathrm{r}}}\, e^{-j\theta_\ell[0]}, \tag{5.15}$$

where $\eta_{\ell_\mathrm{max}}[0]$ is the maximum amplitude related to the $\ell-$th scattering lobe at $m' = 0$, $\varphi_\ell[0]$ is the angle between the $\ell-$th scattering wave and the $\ell-$th reflection wave directions at $m' = 0$, α_r is an integer defined as the width of the scattering lobe and $\theta_\ell[0]$ is the random phase associated with the $\ell-$th path at $m' = 0$ with an uniform distribution in $[0, 2\pi]$. Note that $\theta_\ell[0]$ is constant within one stationary time region.

5.4.2.2 Settings for Propagation Graph

For the propagation graph, we consider the Tx and the Rx positions within each stationary time region k_t as the set of Txs $\mathcal{V}_\mathrm{Tx} = \{\mathrm{Tx}_0, \cdots, \mathrm{Tx}_{M-1}\}$ and the set of Rxs $\mathcal{V}_\mathrm{Rx} = \{\mathrm{Rx}_0, \cdots, \mathrm{Rx}_{M-1}\}$, respectively. The positions of scatterer vertices $\mathcal{V}_\mathrm{S}$ in the graph are obtained from geometric RT results and the geometrical description of the scenario. The set of scatterers can be split as $\mathcal{V}_\mathrm{S} = \mathcal{V}_\mathrm{IP} \cup \mathcal{V}_\mathrm{SD} \cup \mathcal{V}_\mathrm{MD}$, where the "interaction points (IPs)" $\mathcal{V}_\mathrm{IP}$ are directly obtained by the RT reflection points. The "static discrete (SD) scatterers" $\mathcal{V}_\mathrm{SD}$ are located on significant static objects in the tunnel, and "mobile discrete (MD) scatterers" $\mathcal{V}_\mathrm{MD}$ are located on moving objects in the tunnel. The significant static objects involved in the propagation graph are the ones made of metal or glass and hard to describe by RT. We update $\mathcal{V}_\mathrm{IP}$ and $\mathcal{V}_\mathrm{SD}$ positions for each stationary time region k_t. It is further explained as we keep using the same $\mathcal{V}_\mathrm{IP}$ and $\mathcal{V}_\mathrm{SD}$ positions at each stationary time region k_t. While for the $\mathcal{V}_\mathrm{MD}$, we need to update their positions at each time snapshot according to their speeds.

The edges of the graph are defined by considering the specific geometry of the tunnel scenario. We further define that the Txs have edges to all three scatterer types based on different probability of visibility P_{TI}, P_{TS} and P_{TM}. Similarly, all three scatterer types have edges to the Rxs based on different probability of visibility P_{IR}, P_{SR} and P_{MR}. We assume that the probability of visibility between the three scatterer types is zero. The reason is that we consider the contribution either from a SD or from a MD scatterer to be a single path, similar as the contributions from single objects in the tunnel shown in Fig. 5.2(a). Furthermore, due to the plane surface, it is reasonable to assume that there are no edges between scatterers on the same surface [132]. In addition, due to the semi-enclosed tunnel scenario, where the length is much larger than the width and the height of the tunnel, we cannot allow that any two scatterers can see each other without considering the distance. This requires to set a distance threshold d_{th} for which a visibility between scatterers is possible.The particular form of the edge transfer functions $\mathbf{T}[q]$, $\mathbf{R}[q]$ and $\mathbf{B}[q]$ are given as

$$\mathbf{T}[q] = \begin{bmatrix} \mathbf{T}_{\mathrm{IP}}[q] \\ \mathbf{T}_{\mathrm{SD}}[q] \\ \mathbf{T}_{\mathrm{MD}}[q] \end{bmatrix}, \tag{5.16}$$

$$\mathbf{R}[q] = \begin{bmatrix} \mathbf{R}_{\mathrm{IP}}[q] & \mathbf{R}_{\mathrm{SD}}[q] & \mathbf{R}_{\mathrm{MD}}[q] \end{bmatrix} \tag{5.17}$$

and

$$\mathbf{B}[q] = \begin{bmatrix} \mathbf{B}_{\mathrm{II}}[q] & \mathbf{0} & \mathbf{0} \\ \mathbf{0} & \mathbf{B}_{\mathrm{SS}}[q] & \mathbf{0} \\ \mathbf{0} & \mathbf{0} & \mathbf{B}_{\mathrm{MM}}[q] \end{bmatrix} \tag{5.18}$$

with submatrices according to

$\mathbf{T}_{\mathrm{IP}}[q] \in \mathbb{C}^{N_{\mathrm{IP}} \times M}$ connecting $\mathcal{V}_{\mathrm{Tx}}$ to $\mathcal{V}_{\mathrm{IP}}$,

$\mathbf{T}_{\mathrm{SD}}[q] \in \mathbb{C}^{N_{\mathrm{SD}} \times M}$ connecting $\mathcal{V}_{\mathrm{Tx}}$ to $\mathcal{V}_{\mathrm{SD}}$,

$\mathbf{T}_{\mathrm{MD}}[q] \in \mathbb{C}^{N_{\mathrm{MD}} \times M}$ connecting $\mathcal{V}_{\mathrm{Tx}}$ to $\mathcal{V}_{\mathrm{MD}}$,

$\mathbf{R}_{\mathrm{IP}}[q] \in \mathbb{C}^{M \times N_{\mathrm{IP}}}$ connecting $\mathcal{V}_{\mathrm{IP}}$ to $\mathcal{V}_{\mathrm{Rx}}$,

$\mathbf{R}_{\mathrm{SD}}[q] \in \mathbb{C}^{M \times N_{\mathrm{SD}}}$ connecting $\mathcal{V}_{\mathrm{SD}}$ to $\mathcal{V}_{\mathrm{Rx}}$,

$\mathbf{R}_{\mathrm{MD}}[q] \in \mathbb{C}^{M \times N_{\mathrm{MD}}}$ connecting $\mathcal{V}_{\mathrm{MD}}$ to $\mathcal{V}_{\mathrm{Rx}}$,

$\mathbf{B}_{\mathrm{II}}[q] \in \mathbb{C}^{N_{\mathrm{IP}} \times N_{\mathrm{IP}}}$ interconnecting $\mathcal{V}_{\mathrm{IP}}$,

$\mathbf{B}_{\mathrm{SS}}[q] \in \mathbb{C}^{N_{\mathrm{SD}} \times N_{\mathrm{SD}}}$ interconnecting $\mathcal{V}_{\mathrm{SD}}$,

Table 5.1: Edge Definitions at Each Stationary Time Region k_{t}

Edge type	$\mathbb{P}(e \in \mathcal{E})$	Edge gain g_e	Submatrix
Tx-Rx, $e \in \mathcal{V}_{\mathrm{Tx}} \times \mathcal{V}_{\mathrm{Rx}}$	P_{TR}	$\frac{1}{(4\pi f[q]\tau_e)}$	$\mathbf{D}[q]$
Tx-IP, $e \in \mathcal{V}_{\mathrm{Tx}} \times \mathcal{V}_{\mathrm{IP}}$	P_{TI}	$\sqrt{\frac{1}{4\pi f[q]\tau_{(\mathcal{V}_{\mathrm{Tx}} \times \mathcal{V}_{\mathrm{IP}} \times \mathcal{V}_{\mathrm{Rx}})}}}$	$\mathbf{T}_{\mathrm{IP}}[q]$
Tx-SD, $e \in \mathcal{V}_{\mathrm{Tx}} \times \mathcal{V}_{\mathrm{SD}}$	P_{TS}	$\sqrt{\frac{S_{e,\mathrm{TS}}}{4\pi f[q]\tau_{(\mathcal{V}_{\mathrm{Tx}} \times \mathcal{V}_{\mathrm{SD}} \times \mathcal{V}_{\mathrm{Rx}})}}}$	$\mathbf{T}_{\mathrm{SD}}[q]$
Tx-MD, $e \in \mathcal{V}_{\mathrm{Tx}} \times \mathcal{V}_{\mathrm{MD}}$	P_{TM}	$\sqrt{\frac{S_{e,\mathrm{TM}}}{4\pi f[q]\tau_{(\mathcal{V}_{\mathrm{Tx}} \times \mathcal{V}_{\mathrm{MD}} \times \mathcal{V}_{\mathrm{Rx}})}}}$	$\mathbf{T}_{\mathrm{MD}}[q]$
IP-IP, $e \in \mathcal{V}_{\mathrm{IP}} \times \mathcal{V}_{\mathrm{IP}}$	P_{II}	$\frac{g_{\mathrm{II}}}{\sqrt{\mathrm{odi}(e)}} e^{j\theta_{\mathrm{II}}}$	$\mathbf{B}_{\mathrm{II}}[q]$
IP-Rx, $e \in \mathcal{V}_{\mathrm{IP}} \times \mathcal{V}_{\mathrm{Rx}}$	P_{IP}	$\sqrt{\frac{1}{4\pi f[q]\tau_{(\mathcal{V}_{\mathrm{Tx}} \times \mathcal{V}_{\mathrm{IP}} \times \mathcal{V}_{\mathrm{Rx}})}}}$	$\mathbf{R}_{\mathrm{IP}}[q]$
SD-Rx, $e \in \mathcal{V}_{\mathrm{SD}} \times \mathcal{V}_{\mathrm{Rx}}$	P_{SR}	$\sqrt{\frac{S_{e,\mathrm{SR}}}{4\pi f[q]\tau_{(\mathcal{V}_{\mathrm{Tx}} \times \mathcal{V}_{\mathrm{SD}} \times \mathcal{V}_{\mathrm{Rx}})}}}$	$\mathbf{R}_{\mathrm{SD}}[q]$
MD-Rx, $e \in \mathcal{V}_{\mathrm{MD}} \times \mathcal{V}_{\mathrm{Rx}}$	P_{MR}	$\sqrt{\frac{S_{e,\mathrm{MR}}}{4\pi f[q]\tau_{(\mathcal{V}_{\mathrm{Tx}} \times \mathcal{V}_{\mathrm{MD}} \times \mathcal{V}_{\mathrm{Rx}})}}}$	$\mathbf{R}_{\mathrm{MD}}[q]$
Other edges types	$\mathbf{0}$	-	-

$\mathbf{B}_{\mathrm{MM}}[q] \in \mathbb{C}^{N_{\mathrm{MD}} \times N_{\mathrm{MD}}}$ interconnecting $\mathcal{V}_{\mathrm{MD}}$,

where N_{IP}, N_{SD} and N_{MD} are the number of IPs, SD and MD scatterers involved into the propagation graph, and $N_{\mathrm{S}} = N_{\mathrm{IP}} + N_{\mathrm{SD}} + N_{\mathrm{MD}}$.

The LOS contribution is included in RT, so that we set $\mathbf{D}[q] = \mathbf{0}_{M \times M}$ for one stationary time region in the propagation graph. The time-varying transfer function $H_{\mathrm{PG}}[m', q]$ of the propagation graph at one stationary time region k_{t}, accounting for interactions from n_{PG} to infinity in the proposed hybrid model, can be expressed in closed form as

$$H_{\mathrm{PG}}[m', q] = \mathbf{r}[m', q]\mathbf{B}^{\mathrm{n_{PG}}-1}[k_{\mathrm{t}}, q][\mathbf{I} - \mathbf{B}[k_{\mathrm{t}}, q]]^{-1}\mathbf{t}[m', q], \tag{5.19}$$

where $\mathbf{r}[m', q]$ is the $m'-$th row vector of $\mathbf{R}[q]$, $\mathbf{t}[m', q]$ is the $m'-$th column vector of $\mathbf{T}[q]$, and $\mathbf{B}[k_{\mathrm{t}}, q] \in \mathbb{C}^{N_{\mathrm{S}} \times N_{\mathrm{S}}}$ is constant for each stationary time region k_{t}.

In the propagation graph, the edge definitions at each stationary time region k_{t} are listed in Table 5.1.

- We introduce different edge probabilities of visibility $\mathbb{P}(e \in \mathcal{E})$ and different edge gains g_e for different edge types in Table 5.1. As the LOS contribution is included in RT, we set $P_{\mathrm{TR}} = 0$. It also can be seen that the edge probability of visibility $\mathbb{P}(e \in \mathcal{E})$ is set to $\mathbf{0}$ for the edge types $\mathcal{V}_{\mathrm{SD}} \times \mathcal{V}_{\mathrm{SD}}$ and $\mathcal{V}_{\mathrm{MD}} \times \mathcal{V}_{\mathrm{MD}}$. We further treat the contribution from a SD or from a MD scatterer to be a single path. Therefore, we further set $P_{\mathrm{TS}} = P_{\mathrm{TM}} = P_{\mathrm{SR}} = P_{\mathrm{MR}} = 1$. In addition, for P_{TI}, P_{II} and P_{IR}, it is noteworthy that the available edges

are deterministically obtained via edge distances. Therefore, we calculate the relevant logical matrices based on the edge distance. For the corresponding logical matrices $\mathbf{L}_{\mathrm{TI}}$ or $\mathbf{L}_{\mathrm{IR}}$, its element $L_{\mathrm{i}',\mathrm{j}'}$ is defined as

$$L_{\mathrm{i}',\mathrm{j}'} = \begin{cases} 1, & d_{\mathrm{i}',\mathrm{j}'} >= d_{\mathrm{th,min}}, \\ 0, & \text{otherwise.} \end{cases} \tag{5.20}$$

While for logical matrix $\mathbf{L}_{\mathrm{II}}$, its element $L_{\mathrm{i}'',\mathrm{j}''}$ is defined as

$$L_{\mathrm{i}'',\mathrm{j}''} = \begin{cases} 1, & d_{\mathrm{th,min}} <= d_{\mathrm{i}'',\mathrm{j}''} <= d_{\mathrm{th,max}}, \\ 0, & \text{otherwise.} \end{cases} \tag{5.21}$$

$d_{\mathrm{th,min}}$ and $d_{\mathrm{th,max}}$ are two distance thresholds. When the element $L_{\mathrm{i}',\mathrm{j}'} = 1$ or $L_{\mathrm{i}'',\mathrm{j}''} = 1$, we define that the edge is available. Based on (5.20) and (5.21), the number of available edges in each matrix $\mathbf{L}_{\mathrm{TI}}$, $\mathbf{L}_{\mathrm{IR}}$ or $\mathbf{L}_{\mathrm{II}}$ can be calculated. Furthermore, we can obtain the probability of visibility P_{TI}, P_{IR} and P_{II}.

- The defined edge gains g_e in Table 5.1 are used for calculating the edge transfer function $A_e[q]$. It is an element of the matrices $\mathbf{T}[q]$, $\mathbf{R}[q]$ and $\mathbf{B}[q]$ taking into account different edges. In order to use the propagation graph, specifying the edge transfer function $A_e[q]$ is required. For a vertex position $\mathbf{r}_v$, associated to each vertex $v \in \mathcal{V}$, the edge transfer function is defined as

$$A_e[q] = \begin{cases} g_e[q] \exp(-j2\pi\tau_e f[q]), & e \in \mathcal{E}, \\ 0, & e \notin \mathcal{E}. \end{cases} \tag{5.22}$$

where $\tau_e = \|\mathbf{r}_v - \mathbf{r}_{v'}\|/c$ is the propagation delay between the vertex $\mathbf{r}_v$ and the vertex $\mathbf{r}_{v'}$, and $f[q] = f_{\mathrm{c}} + q f_{\mathrm{s}}$. Please distinguish τ_e with $\tau_{(\mathcal{V}_{\mathrm{Tx}} \times \mathcal{V}_{\mathrm{S}} \times \mathcal{V}_{\mathrm{Rx}})}$ in Table 5.1, which is the propagation delay of the edges from the Tx to the scatterer and from the scatterer to the Rx. odi(e) denotes the number of outgoing edges of the initial vertex of edge e, and $\theta_{\mathrm{II}} \in [0, 2\pi]$ is the random phase set only once for each stationary time region k_{t}. The defined edge gain related to scatterers resembles Friis equation considering the first order interaction. It can be seen that this definition is different to [124]. For the edge gain related to IPs, the distance threshold has weighted the edge. For the edge gain related to SD and MD scatterers, S_e is used to weight the edge according to the scatterer material, which is defined as

$$S_e = (1 - a_e)^2, \tag{5.23}$$

where the average absorption coefficient a_e is related to the scatterer material [67]. Referring to the edge gain g_{II}, it depends on the slope ρ of the delay-power spectrum of higher-order reflection paths as

$$g_{\mathrm{II}} \approx 10^{\frac{\rho\mu(\mathcal{E}_{\mathrm{II}})}{20}}, \tag{5.24}$$

where $\mu(\mathcal{E}_{\mathrm{II}}) = \frac{1}{|\mathcal{E}_{\mathrm{II}}|}\sum_{e\in\mathcal{E}_{\mathrm{II}}}\tau(e \in \mathcal{E}_{\mathrm{II}})$ is the average delay among all edges $e \in \mathcal{E}_{\mathrm{II}}$. For our study, we predict the slope ρ based on applying the approximate higher-order reflection algorithm at only one time snapshot. After obtaining the CIR of the higher-order reflection algorithm, a least-squares linear regression line is superimposed on the delay-power spectrum plot to obtain the slope ρ.

5.4.3 Numerical Results

5.4.3.1 Simulation Setup

A pictorial view of the scenario considering one Tx and one Rx position at one time snapshot is illustrated in Fig. 5.8, where different materials are sketched with different colors. Note that the coordinate system in Fig. 5.8 is different with the one used in Fig. 5.4. Modeling the tunnel scenario in RT is the same as in Section 5.3.2. RT takes into account the following propagation mechanisms: LOS, reflections up to the fourth order ($n_{\mathrm{RT}} = 4$), single-order diffraction and single bounce scattering. Penetration has been embedded into all other mechanisms. Some propagation paths are visualized in Fig. 5.8(a). It is noteworthy that we do not consider the ventilation systems, EXIT signs, metallic structure and the moving vehicle in the RT simulation. The contributions from these objects are considered by the propagation graph. In the following, we introduce the settings for propagation graph, including the positions of scatterers, edge probability of visibility and edge gain.

- *Positions of Scatterers*: The scatterers in the propagation graph at one time snapshot are shown in Fig. 5.8(b), where different scatterer types are marked with different colors. The IPs are directly obtained from all reflection points obtained by RT. The number of IPs N_{IP} is different for different stationary time regions. $N_{\mathrm{SD}} = 12$ is defined in the propagation graph, in which 3 SD scatterers on ventilation systems, 8 SD scatterers on the EXIT signs and 1 SD scatterer on the big metallic structure at the entrance. We define these SD scatterers according to i) blocks are made of metal or glass, which are important reflectors in the scenario, ii) the ventilation system and the big metallic structure are hard to be accurately described by RT due to their

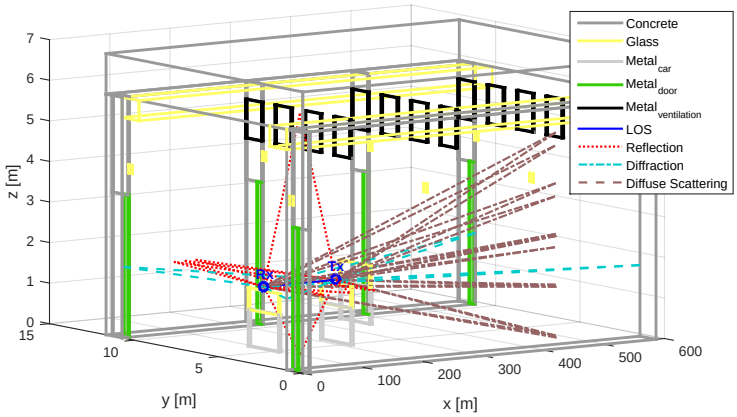

(a) 3D View

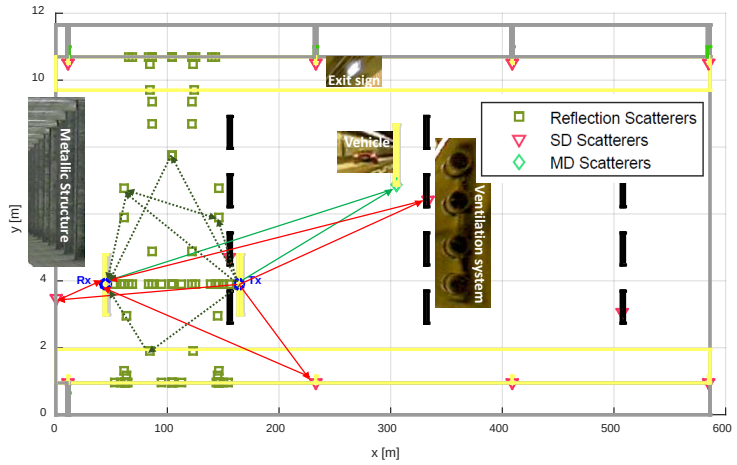

(b) 2D View

Figure 5.8: Pictorial view of the scenario built by RT considering the Tx and the Rx positions at one time snapshot. (a) 3D view. (b) 2D view.

irregular shapes, and iii) the EXIT signs are small in size. Moreover, there is $N_{\mathrm{MD}} = 1$ MD scatterer on the moving vehicle, which is in front of the Tx vehicle during the simulation period. In Fig. 5.8(a), it can be seen that the blocks, including ventilation systems, EXIT signs, big metallic structure and the moving vehicle, have been roughly described in RT. Then both SD and MD scatterers positions $\mathbf{r}_v$ are located on the described blocks in Fig. 5.8(b).

- *Edge Probability of Visibility*: There are some examples of edges shown in Fig. 5.8(b). The edges in solid lines are considered within $\mathbb{P}(e \in \mathcal{E}) = 1$, while the dotted lines indicate edges within P_{TI}, P_{IR} and P_{II} in the propagation graph. According to (5.20) and (5.21), we need to set the distance thresholds $d_{\mathrm{th,min}}$

Table 5.2: Setting of Average Absorption Coefficient and Edge Weights

Scatterer location	Material	a_e	S_e
Metallic structure	Metal (PEC)	0	1
EXIT sign	Glass	0.4	0.36
Ventilation system	Metal	0.4	0.36
Moving vehicle	Metal (PEC)	0	1

and $d_{\text{th,max}}$. The distance threshold $d_{\text{th,min}}$ limits the visibility between the Txs and the IPs, the visibility between the IPs and the Rxs, and the visibility between IPs. As described in Section 5.2.1, the LOS path length is 120 m. The longest reflection path length calculated by RT is 126.15 m. Therefore, we approximately set $d_{\text{th,min}} = (126.15 - 120)/2 = 3.075\,\text{m}$, which makes sure that propagation paths calculated based on RT and the propagation graph cannot overlap with each other. This is also the reason that we can set $n_{\text{PG}} = 2$ in the propagation graph. The distance threshold $d_{\text{th,max}}$ limits the interconnection among all IPs. We approximately set $d_{\text{th,max}} = 36\,\text{m}$, which is determined by the average distance between any two IP $v \in \mathcal{V}_{\text{IP}}$ among all stationary time regions.

- *Edge Gain*: For the edge gain, the average absorption coefficient a_e and the slope ρ need to be determined. We select a_e as in [67]. The relevant values are listed in Table 5.2. Due to the irregular shape of the ventilation system, shown in Fig. 5.8(b), we do not set its edge weight to 1.

  For obtaining the slope ρ, the approximate higher-order reflection algorithm is performed at one time snapshot to obtain the CIR firstly. Then a least-squares linear regression line is superimposed on the delay-power spectrum plot in Fig. 5.9, where $\rho = -72.20\,\text{dB}/\mu\text{s}$.

We aim to compare the simulation results with the measurements for the time interval $T = 5\,\text{s}$, corresponding to $[4, 9]\text{s}$ in Fig. 5.2, which contains $K_{\text{t}} = 125$ stationary time regions in the following analysis. RT and the propagation graph are performed once for each stationary region k_{t}. The relevant CTFs $H_{\text{RT}}[m, q]$ and $H_{\text{PG}}[m, q]$ at $S = 16000$ snapshots can be obtained by using (5.13) and (5.19) for each stationary time region, respectively.

5.4.3.2 Simulation Time

Due to the complicated implementation of RT, it is hard to calculate the computational complexity. Therefore, we evaluate the simulation time here (2.4 GHz Intel

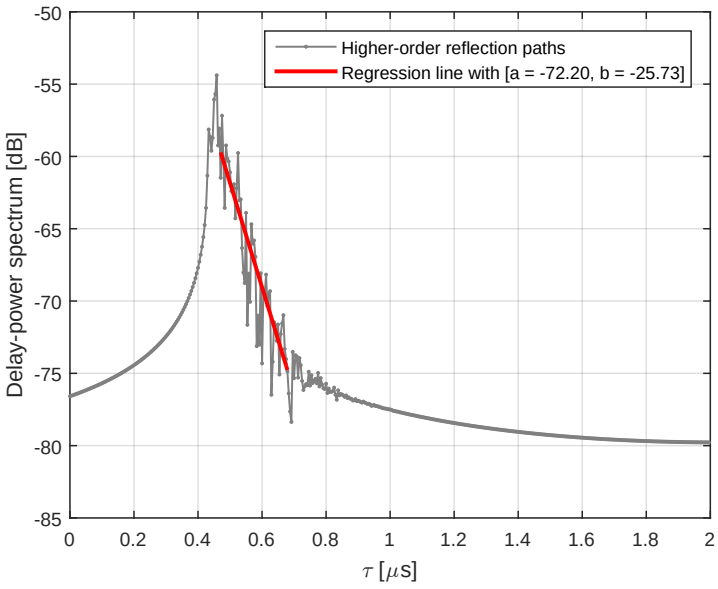

Figure 5.9: Delay-power spectrum plot based on the approximate higher-order reflection algorithm at one time snapshot and a corresponding least-squares linear regression line.

Core i7 CPU with 8 GB RAM). The simulation time of obtaining the time-varying CTF $H_{\mathrm{RT}}[m, q]$ at one stationary time region is about 51 s, in which calculating deterministic paths and diffuse scattering paths takes 6 s and 45 s, respectively. Moreover, the simulation time for obtaining the time-varying CTF $H_{\mathrm{PG}}[m, q]$ at one stationary time region is about 21 s. In total, the proposed hybrid model takes about 72 s to get the time-varying CTF $H_{\mathrm{HY}}[m, q]$ for one stationary time region k_{t}. Comparing the simulation time based on the tunnel RT algorithm in Section 5.3.2, where the algorithm takes about 407 s at one time snapshot. The proposed hybrid channel model in this section reduces the computational complexity significantly.

5.4.3.3 Analysis of Time-Varying PDP and DSD

The normalized time-varying PDP $\hat{P}_{\mathrm{HY},\tau}[k_{\mathrm{t}}; n]$ and time-varying DSD $\hat{P}_{\mathrm{HY},\nu}[k_{\mathrm{t}}; p]$ of the proposed hybrid channel model are calculated based on (5.5) and (5.6), respectively. The obtained results are shown in Fig. 5.10. In order to make a reasonable comparison with the measurement data, we add white Gaussian noise $n[m, q]$ with variance $\sigma_n^2 = \frac{1}{\mathrm{SNR}}$ with $\mathrm{SNR} = -40\,\mathrm{dB}$.

The contribution from the objects inside the tunnel are clearly distinguishable. It can be seen that the simulation results predict well the time-varying PDP and DSD

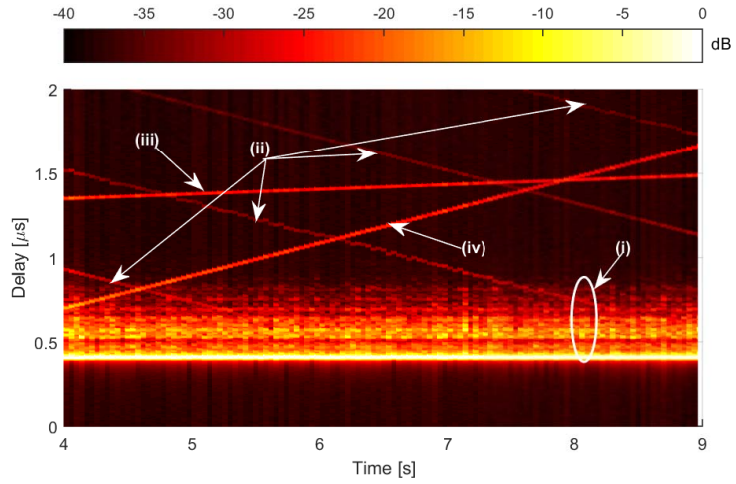

(a) Time-varying PDP

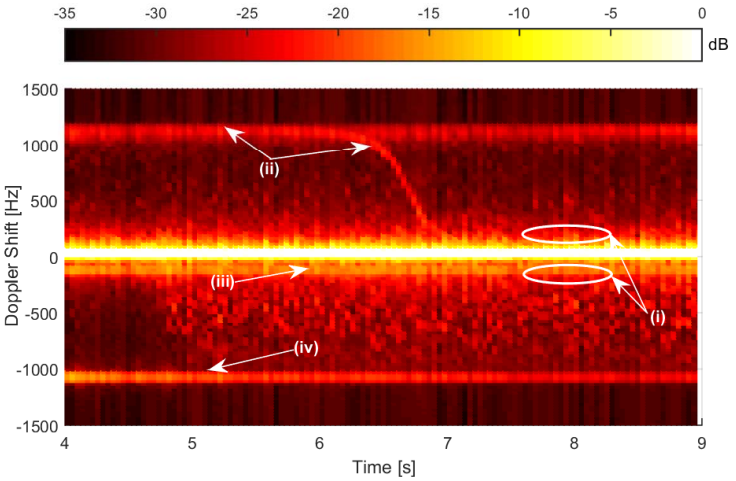

(b) Time-varying DSD

Figure 5.10: Normalized time-varying PDP and DSD obtained based on the proposed hybrid channel model over interval of $T = 5\,\mathrm{s}$, where $t = 4\,\mathrm{s}, \ldots, 9\,\mathrm{s}$.

when comparing to the measurement data in Fig. 5.2. The following propagation phenomena are analyzed: (i) higher-order reflection components which are mainly caused by the tunnel walls, ceiling and ground, (ii) multipath components from the ventilation system and from traffic signs in front of the Rx, (iii) multipath components caused by the car driving approximately 10 km/h faster than the Tx and Rx, and (iv) strong multipath components caused by a big metallic structure at the entrance ceiling and traffic signs which are behind the Rx.

In Fig. 5.11, we focus on one stationary time region $k_\mathrm{t} = 45$ and compare the PDP and DSD of our proposed hybrid model with measurements. From Fig. 5.11 (a), it

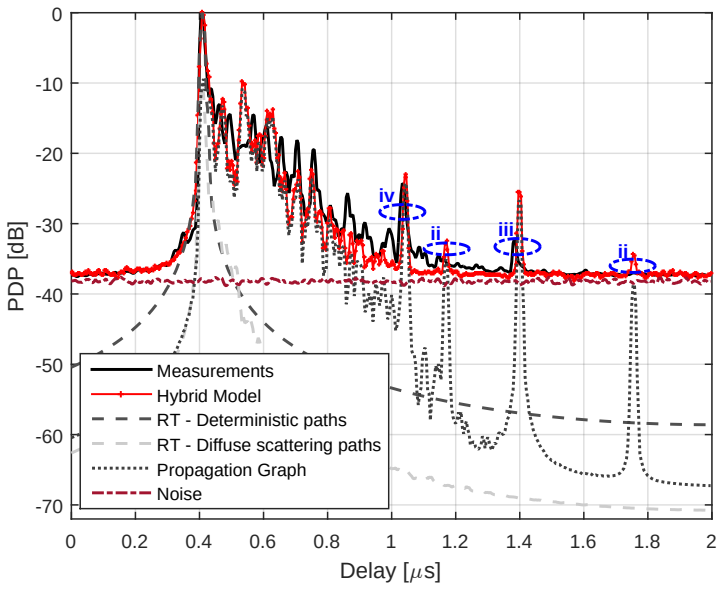

(a) Time-varying PDP at $k_t = 45$

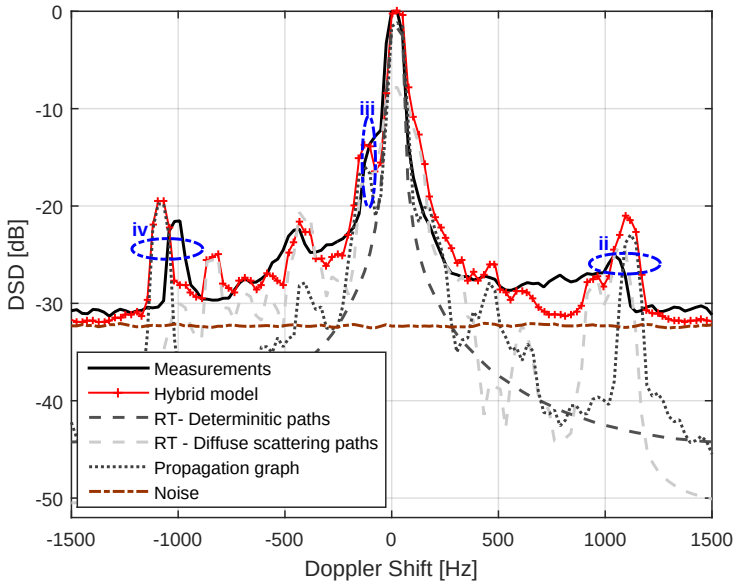

(b) Time-varying DSD at $k_t = 45$

Figure 5.11: Normalized time-varying PDP and DSD based on the tunnel RT algorithm at stationary time region $k_t = 45$.

can be seen that the normalized PDP based on measurements and the proposed hybrid channel model are comparable to each other. The peaks appearing at 1 μs, 1.2 μs, 1.4 μs and 1.8 μs, marked by the blue indexed ellipses, are mainly caused by the big metallic structure, the ventilation system, the moving vehicle, and the traffic

signs, respectively. The imprecision of the power of the path marked as 'iii' in Fig. 5.11 (a) is 6 dB higher than the measurement. This is mainly caused by assuming the vehicle as a PEC in our simulation. However, the same path seen in Fig. 5.11 (b) is similar with the measurement, because the diffuse scattering also contributes to the path 'iii'. Moreover, it can be seen that diffuse scattering components contain more power when they are close to the LOS path in Fig. 5.11 (a). In addition, it can be observed from Fig. 5.11 (b) that diffuse scattering components play an important role in the DSD evaluation, whose power is higher than the noise power.

5.4.4 Analysis of Time-Varying Delay Spread and Doppler Spread

The time-varying RMS delay spread at stationary time region k_t is defined as [104]

$$\sigma_\tau[k_\mathrm{t}] = \sqrt{\frac{\sum_{n=0}^{N-1}(n\tau_\mathrm{s})^2\hat{P}_\tau[k_\mathrm{t};n]}{\sum_{n=0}^{N-1}\hat{P}_\tau[k_\mathrm{t};n]} - \bar{\tau}[k_\mathrm{t}]^2}, \tag{5.25}$$

with

$$\bar{\tau}[k_\mathrm{t}] = \frac{\sum_{n=0}^{N-1}(n\tau_\mathrm{s})\hat{P}_\tau[k_\mathrm{t};n]}{\sum_{n=0}^{N-1}\hat{P}_\tau[k_\mathrm{t};n]}, \tag{5.26}$$

and the time-varying RMS Doppler spread at stationary time region k_t is defined as

$$\sigma_\nu[k_\mathrm{t}] = \sqrt{\frac{\sum_{p=-M/2}^{M/2-1}(p\nu_\mathrm{s})^2\hat{P}_\nu[k_\mathrm{t};p]}{\sum_{p=-M/2}^{M/2-1}\hat{P}_\nu[k_\mathrm{t};p]} - \bar{\nu}[k_\mathrm{t}]^2}, \tag{5.27}$$

with

$$\bar{\nu}[k_\mathrm{t}] = \frac{\sum_{p=-M/2}^{M/2-1}(p\nu_\mathrm{s})\hat{P}_\nu[k_\mathrm{t};p]}{\sum_{p=-M/2}^{M/2-1}\hat{P}_\nu[k_\mathrm{t};p]}. \tag{5.28}$$

Note that in the following comparison, we do not involve the noise in simulation. We compare the RMS delay spreads based on the measurements and different algorithms

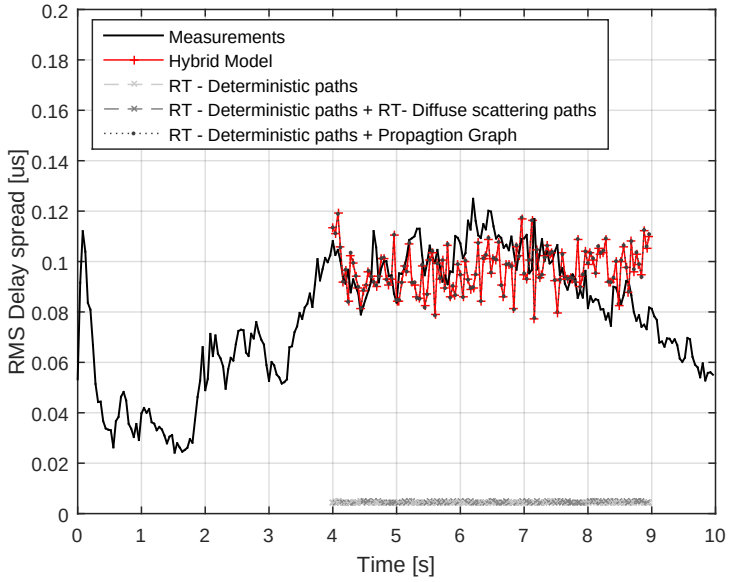

(a) RMS Delay Spread

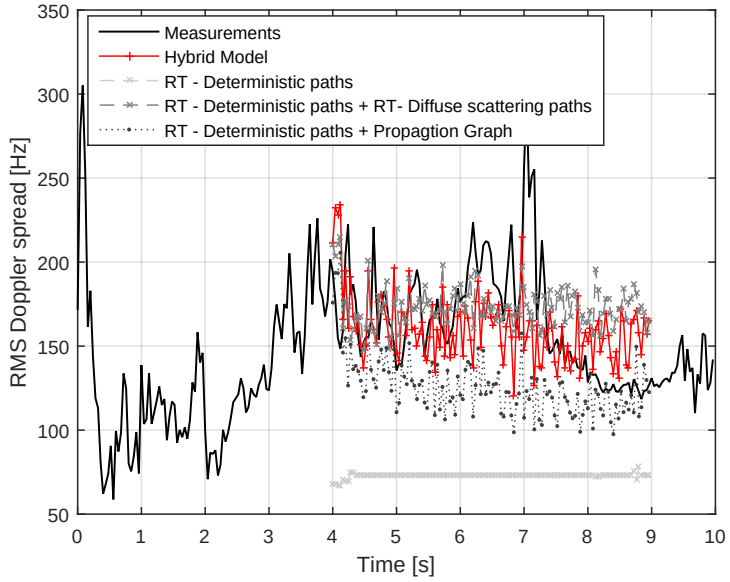

(b) RMS Doppler Spread

Figure 5.12: Time-varying RMS delay and Doppler spreads comparison.

in Fig. 5.12 (a). The RMS delay spread σ_τ of the measurements oscillates around 0.1 μs. The proposed hybrid channel model provides a similar trend and mean value as the measurements. RT with only deterministic paths provides a smaller constant σ_τ value around 0.004 μs, and RT with deterministic and diffuse scattering paths provides the similar σ_τ value around 0.004 μs. When considering deterministic paths

in RT and the paths generated by the propagation graph, the σ_τ value is similar as the proposed hybrid channel model. Thus, we conclude that the RMS delay spread σ_τ is dominantly determined by the contribution from the deterministic paths in RT and the paths obtained by the propagation graph. The diffuse scattering paths, containing low power, would not influent the RMS delay spread σ_τ significantly.

Moreover, we compare the RMS Doppler spreads in Fig. 5.12 (b). The RMS Doppler spread σ_ν of the measurement oscillates around 170 Hz. The proposed hybrid channel model provides a similar mean value as the measurement. RT with only deterministic paths provides a smaller constant σ_ν value around 70 Hz, while RT with deterministic and diffuse scattering paths provides the similar σ_ν value as the proposed hybrid channel model. When deterministic paths in RT and the paths generated by the propagation graph, the σ_ν value is a slightly lower than the proposed hybrid channel model. Therefore, we can see that the contribution from diffuse scattering paths plays an important role in the RMS Doppler spread analysis.

6 Conclusion

6.1 Summary

In this thesis, we investigated methods to reduce the computational complexity of RT with no loss of accuracy in three scenarios: wideband indoor, UWB indoor and tunnel scenarios. We started by briefly describing the RT tool used throughout the thesis and the propagation mechanisms were presented. Three major wave propagation mechanisms are: (i) LOS, (ii) specular and (iii) diffuse scattering. The specular mechanism refers to reflection, penetration and diffraction.

In order to accelerate the execution of the RT tool, the implemented MATLAB code was firstly optimized by converting time-consuming algorithms to MEX functions by using MATLAB Coder. Moreover, we focused on speeding up the reflection algorithm, because the construction of the image tree required a great amount of CPU time and saving all the information for every node in the image tree required a huge memory. Thus, we devised an efficient implementation for building the image tree and for calculating reflection paths to solve the memory issue.

We were interested in reducing the computational complexity of RT not only for one terminal position but also for multiple mobile terminal positions in this thesis. This is important for modeling the performance of moving nodes, e.g. vehicles, people, planes etc. For one terminal position, an efficient subdivision algorithm of diffuse scattering based on concentric circles was proposed and evaluated in a wideband indoor scenario. While simulating the radio propagation conditions for a mobile terminal, we presented a low-complexity RT algorithm based on two-dimensional DPS sequences for wideband indoor scenarios.

In UWB indoor scenarios, we firstly devised a SDRT algorithm for one terminal position. The reason is the computational complexity of the conventional SDRT is directly proportional to the number of sub-bands. Our new proposed SDRT algorithm is almost independent of the number of sub-bands. Furthermore, we presented a low-complexity SDRT algorithm based on two-dimensional DPS sequences for multiple mobile terminal positions, where we extended the wideband case to the UWB case by expanding the DPS sequences to each sub-band. In addition, the accuracy of RT is strictly limited by the available description of the environment. We pro-

posed a calibration method for indoor UWB low-complexity SDRT. The method estimates the optimal material parameters, including the dielectric parameters and the scattering parameters, using channel measurements and MOSA.

We also considered to apply RT in tunnel scenarios. As the first step, we combined an approximated higher-order reflection algorithm with RT for ITS in tunnel scenarios. The approximated higher-order reflection algorithm only depends on the width and height of the tunnel, and the Tx and the Rx position. Therefore, the obtained propagation paths are the same at any time snapshot when the environment keeps constant. This motivated our interest in designing a hybrid ray and graph method to simulate the in-tunnel time-variant V2V propagation channel. The concerned propagation graph models not only the higher-order reflection paths, but also the significant contribution from discrete scatterers on those small or irregular shaped objects.

6.2 Key Results

In this section, we list the main results of the thesis topic-wise.

Ray Tracing for Wideband Indoor Scenarios
A simulated indoor scenario with 10 blocks was used to test the simulation time of RT based on the original MATLAB implementation and the one with updated MEX functions. According to the efficient implementation of the reflection algorithm, the simulation time was strongly reduced from 154 s to 3 s. Considering all generated MEX functions, about 90% total simulation time of the original code was saved.

An effective subdivision algorithm for diffuse scattering of RT in indoor scenarios was presented. The algorithm is based on concentric circles and the system bandwidth. The random characteristic of the diffuse scattering was demonstrated and the tile size is independent of the scenario. The new algorithm based on concentric circles was verified by comparing its results with the one based on the far-field condition through evaluating: (i) the normalized PDPs of both methods had a correlation of 0.968, (ii) the MRE of the delay spread was about -25 dB between these two subdivision algorithms and (iii) the MREs of the AoA and the EoA spread were about -35 dB and -27.5 dB between the mentioned two subdivision algorithms, respectively. Furthermore, the computational complexity was significantly reduced because of the smaller number of diffuse scattering paths.

Moreover, we presented a low-complexity RT algorithm to reduce the computation time of RT in time-variant indoor environments. The temporal correlation of diffuse scattering components was considered for a short moving distance of the Rx.

In the first step, the SoCE channel model was applied to reduce the RT complexity. The accuracy of the SoCE channel model with respect to RT was verified using an error threshold. In order to further reduce the simulation time, the two-dimensional DPS subspace channel model was implemented to approximate the SoCE model. The computational complexity reduction factor of the proposed RT algorithm using the DPS subspace is bound by the number of time samples. Furthermore, the computational complexity reduction achieved by the DPS subspace channel model increases with the number of propagation paths when the number of time samples is fixed.

Ray Tracing for UWB Indoor Scenarios

For UWB indoor scenarios, we presented a low-complexity SDRT firstly. The algorithm was derived from the electromagnetic illumination of the propagation paths base on two important assumptions: (i) the effective permittivity of each material and (ii) the transfer function in the dyadic diffraction coefficient are both independent of frequency. According to our approach, not only the geometrical calculation, but also the electromagnetic calculation of the propagation paths at one specific location needs to be performed only once. Therefore, a reduction of the computational complexity by a factor equal to the number of sub-bands, can be achieved. Furthermore, the normalized PDPs of the conventional SDRT and low-complexity SDRT are comparable to each other. Based on the proposed implementation, we can increase the number of sub-bands without increasing simulation time.

Based on this developed low-complexity algorithm, we calibrated the SDRT algorithm for UWB indoor channels using the MOSA algorithm to optimize the dielectric material parameters and the scattering parameters. Our method allowed the joint tuning of these parameters to reduce the mismatch between measurements and RT simulations. Firstly, the deterministic and diffuse scattering paths were distinguished in the measurement data relying upon cross correlation and a search and subtract algorithm. The MOSA algorithm is based on the weighted sum approach, in which two objective functions are used. From the finally determined Pareto set, an optimal set of material parameters can be obtained. Based on the optimal material parameters, the differences of the normalized PDP and the RMS delay spread between measurements and low-complexity SDRT simulation results were minimized.

For multiple mobile terminal positions, we presented a SDRT algorithm using a projection on DPS subspaces to reduce the computational complexity for multiple Rx positions in UWB indoor scenarios. The proposed DPS subspace algorithm requires RT results only for one sub-band at the initial Rx position in order to

obtain CTFs for the remaining Rx positions. Because the geometrical information of the propagation paths is the same for all sub-bands, the subspace dimension and the basis coefficients in the frequency domain need to be calculated only once for all sub-bands. Moreover, we evaluated the accuracy of the proposed algorithm, opposed to low-complexity SDRT. The accuracy evaluation includes the MSE of CTFs and the RMS delay spread. In addition, we considered the effect of antenna characteristics on the proposed algorithm. We found that the antenna radiation pattern influences the MSE of CTFs and the RMS delay spread. Furthermore, the computation time of these algorithms was analyzed. The proposed DPS subspace algorithm reduced the computation time by more than one order of magnitude compared to low-complexity SDRT.

Ray Tracing for Tunnel Scenarios
We presented a RT algorithm for modeling V2V communication links in-tunnel channels by combining conventional RT enhanced with an effective subdivision algorithm for diffuse scattering and the approximate higher-order reflection algorithm. The accuracy of the proposed algorithm was verified by comparing its time-varying PDP to the ones obtained from the real-world measurements. Moreover, we have shown that by implementing solely the higher-order reflection algorithm the important contributions from the objects inside the tunnel can not be distinguished.

Due the limitation of the higher-order reflection algorithm, a hybrid non-stationary V2V channel model was proposed. The hybrid model combines RT, enhanced with an effective subdivision algorithm for diffuse scattering, with the propagation graph, to yield a novel channel model for the in-tunnel environments. We included the time evolution of the relevant parameters in the proposed model based on the LSF. In order to reduce the computational complexity of RT, the time evolution of the propagation paths is considered by using the SoCE algorithm for each stationary time region. The propagation graph generates not only the reflection tail, but also the contributions from other important SD and MD scatterers in the tunnel. All parameter settings for the propagation graph were obtained from the RT tool. The SD scatterers locations were updated for every stationary time region based on the RT results, while the MD scatterers locations were updated for every time snapshot based on their speed. The accuracy of the proposed algorithm was verified by comparing with channel measurements. The proposed hybrid model allowed us to obtain PDP, DSD, RMS delay and Doppler spreads that are very similar to the measured ones. We also showed that the contribution from the diffuse scattering paths play an important role in the DSD and RMS Doppler spread evaluation.

6.3 Outlook

Recently, extensive research is on-going to understand the specific radio propagation characteristics for 5G mobile communications systems. Two obvious aspects are concerned: i) the radically higher carrier frequencies in the mmW range and ii) the use of substantially larger antenna arrays, e.g., massive MIMO. These requires better channel models for 5G, where RT is considered as a potential channel modeling tool. However, as explained in this thesis, the computational complexity and the accuracy needs to be balanced. How to reduce the computational complexity with no loss of accuracy of RT always needs to be considered when applying it in a specific scenario.

Bibliography

[1] A. F. Molisch, *Wireless Communications*, ser. Wiley - IEEE. Wiley, 2005.

[2] V. Degli-Esposti, F. Fuschini, E. M. Vitucci, and G. Falciasecca, "Measurement and modelling of scattering from buildings," in *IEEE Transactions on Antennas and Propagation*, vol. 55, no. 1, January 2007, pp. 143 – 153.

[3] C. Shannon, "A mathematical theory of communication," in *Bell System Technical Journal*, vol. 27, 1948, pp. 379–423.

[4] T. S. Rappaport, *Wireless Communications: Principles and Practice*, 1st ed. Piscataway, NJ, USA: IEEE Press, 1996.

[5] J. G. Andrews, S. Buzzi, W. Choi, S. V. Hanly, A. Lozano, A. C. K. Soong, and J. C. Zhang, "What will 5G be?" in *IEEE Journal on Selected Areas in Communications*, vol. 32, no. 6, June 2014, pp. 1065–1082.

[6] M. Zhu, "Geometry-based radio channel charaterization and modeling: Parameterization, implementation and validation," in *PHD dissertation*, Aug. 2014.

[7] A. Goldsmith, *Wireless Communications*. Cambridge University Press, 2005.

[8] S. S. Ghassemzadeh, L. J. Greenstein, A. Kavcic, T. Sveinsson, and V. Tarokh, "UWB indoor path loss model for residential and commercial buildings," in *IEEE 58th Vehicular Technology Conference (VTC Fall)*, vol. 5, October 2003, pp. 3115–3119.

[9] S. Deng, M. K. Samimi, and T. S. Rappaport, "28 GHz and 73 GHz millimeter-wave indoor propagation measurements and path loss models," in *IEEE International Conference on Communication Workshop (ICCW)*, June 2015, pp. 1244–1250.

[10] F. Mani, "Improved ray-tracing for advanced radio propagation channel modeling," in *PHD dissertation*, June 2012.

[11] V. Erceg, L. J. Greenstein, S. Y. Tjandra, S. R. Parkoff, A. Gupta, B. Kulic, A. A. Julius, and R. Bianchi, "An empirically based path loss model for wireless channels in suburban environments," in *IEEE Journal on Selected Areas in Communications*, vol. 17, no. 7, July 1999, pp. 1205–1211.

[12] B. H. Fleury, "An uncertainty relation for WSS processes and its application to WSSUS systems," in *IEEE Transactions on Communications*, vol. 44, no. 12, December 1996, pp. 1632–1634.

[13] M. Hatay, "Empirical formula for propagation loss in land mobile radio services," in *IEEE Transactions on Vehicular Technology*, vol. 29, no. 3, August 1980, pp. 317–325.

[14] COST231, "Digital mobile radio: COST231 view on the evolution towards third generation systems," in *European Commision/COST Telecommunications, Tech. Rep.*, 1998.

[15] A. A. M. Saleh and R. A. Valenzuela, "A statistical model for indoor multipath propagation," in *IEEE Journal on Selected Areas in Communications*, vol. 5, no. 2, February 1987, pp. 128–137.

[16] J. Kåredal, F. Tufvesson, N. Czink, A. Paier, C. Dumard, T. Zemen, C. Mecklenbräuker, and A. F. Molisch, "A geometry-based stochastic MIMO model for vehicle-to-vehicle communications," in *IEEE Transactions on Wireless Communications*, vol. 8, no. 7, July 2009, pp. 3646 – 3657.

[17] P. Almers, E. Bonek, A. Burr, N. Czink, M. Debbah, V. Degli-esposti, H. Hofstetter, P. Kyösti, D. Laurenson, G. Matz, A. F. Molisch, C. Oestges, and H. Özcelik, "Survey of channel and radio propagation models for wireless MIMO systems," in *EURASIP Journal on Wireless Communications and Networking*, 2007.

[18] "IST-4-027756 WINNER II D1.1.2 V1.2," in *WINNER II channel models*, 2008. [Online]. Available: Available:http://www.ist-winner.org

[19] R. Verdone and A. Zanella, *Pervasive mobile and ambient wireless communications : COST Action 2100 (Signals and Communication Technology)*, 1st ed. London: Springer, 2012.

[20] B. E. Gschwendtner, G. Wölfle, B. Burk, and F. M. Landstorfer, "Ray tracing vs. ray launching in 3-D microcell modelling," in *1st European Personal and Mobile Communications Conference (EPMCC)*, November 1995.

[21] M. C. Lawton and J. P. McGeehan, "The application of a deterministic ray launching algorithm for the prediction of radio channel characteristics in small-cell environments," in *IEEE Transactions on Vehicular Technology*, vol. 43, no. 4, November 1994, pp. 955–969.

[22] K. Rizk, J.-F. Wagen, and F. Gardiol, "Ray tracing based path loss prediction in two microcellular environments," in *IEEE 5th International Symposium on Personal, Indoor and Mobile Radio Communications, 1994. Wireless Networks - Catching the Mobile Future.*, vol. 2, September 1994, pp. 384–388.

[23] G. E. Athanasiadou, A. R. Nix, and J. P. McGeehan, "A microcellular ray-tracing propagation model and evaluation of its narrow-band and wide-band predictions," in *IEEE Journal on Selected Areas in Communications*, vol. 18, no. 3, March 2000, pp. 322–335.

[24] H. Li, C. Chen, T. Liu, and H. Lin, "Applicability of ray-tracing technique for the prediction of outdoor channel characteristics," in *IEEE Transactions on Vehicular Technology*, vol. 49, no. 6, November 2000, pp. 2336–2349.

[25] C. Oestges, B. Clerckx, L. Raynaud, and D. Vanhoenacker-Janvier, "Deterministic channel modeling and performance simulation of microcellular wideband communication systems," in *IEEE Transactions on Vehicular Technology*, vol. 51, no. 6, November 2002, pp. 1422 – 1430.

[26] T. Rautiainen, G. Wolfle, and R. Hoppe, "Verifying path loss and delay spread predictions of a 3D ray tracing propagation model in urban environment," in *IEEE 56th Vehicular Technology Conference (VTC Fall)*, vol. 4, 2002, pp. 2470–2474.

[27] F. Fuschini, H. El-Sallabi, V. Degli-Esposti, L. Vuokko, D. Guiducci, and P. Vainikainen, "Analysis of multipath propagation in urban environment through multidimensional measurements and advanced ray tracing simulation," in *IEEE Transactions on Antennas and Propagation*, vol. 56, no. 3, March 2008, pp. 848–857.

[28] Y. Corre and Y. Lostanlen, "Three-dimensional urban EM wave propagation model for radio network planning and optimization over large areas," in *IEEE Transactions on Vehicular Technology*, vol. 58, no. 7, September 2009, pp. 3112–3123.

[29] H. Nguyen, G. R. MacCartney, T. Thomas, T. S. Rappaport, B. Vejlgaard, and P. Mogensen, "Evaluation of empirical ray-tracing model for an urban outdoor scenario at 73 GHz E-band," in *IEEE 80th Vehicular Technology Conference (VTC Fall)*, September 2014, pp. 1–6.

[30] S. Baek, Y. Chang, H. Kim, and A. Agiwal, "Comparison analysis of outdoor channel characteristics at 28 GHz and 2 GHz using 3D ray-tracing technique," in *IEEE 80th Vehicular Technology Conference (VTC Fall)*, September 2014, pp. 1–5.

[31] M. K. Samimi, T. Rappaport, and G. R. MacCartney, "Probabilistic omnidirectional path loss models for millimeter-wave outdoor communications," in *IEEE Wireless Communications Letters*, vol. PP, no. 99, March 2015, pp. 1–1.

[32] G. E. Athanasiadou and A. R. Nix, "A novel 3-D indoor ray-tracing propagation model: the path generator and evaluation of narrow-band and wide-band predictions," in *IEEE Transactions on Vehicular Technology*, vol. 49, no. 4, Jul. 2000, pp. 1152–1168.

[33] F. S. de Adana, O. Gutierrez Blanco, I. G. Diego, J. Perez Arriaga, and M. F. Catedra, "Propagation model based on ray tracing for the design of personal communication systems in indoor environments," in *IEEE Transactions on Vehicular Technology*, vol. 49, no. 6, November 2000, pp. 2105–2112.

[34] A. Burr, "Evaluation of capacity of indoor wireless MIMO channel using ray tracing," in *International Zurich Seminar on Broadband Communications Access, Transmission, Networking.*, February. 2002, pp. 28–1–28–6.

[35] T. Rautiainen, R. Hoppe, and G. Wolfle, "Measurements and 3D ray tracing propagation predictions of channel characteristics in indoor environments," in *IEEE 18th International Symposium on Personal, Indoor and Mobile Radio Communications (PIMRC)*, September 2007, pp. 1–5.

[36] S. Priebe, M. Jacob, C. Jastrow, T. Kleine-Ostmann, T. Schrader, and T. Kürner, "A comparison of indoor channel measurements and ray tracing simulations at 300 GHz," in *International 35th Conference on Infrared Millimeter and Terahertz Waves (IRMMW-THz)*, September 2010, pp. 1–2.

[37] E. Haddad, N. Malhouroux, P. Pajusco, and M. Ney, "Optimization of 3D ray tracing for MIMO indoor channel," in *XXXth URSI General Assembly and Scientific Symposium*, August 2011, pp. 1–4.

[38] F. Mani, F. Quitin, and C. Oestges, "Directional spreads of dense multipath components in indoor environments: Experimental validation of a ray-tracing approach," in *IEEE Transactions on Antennas and Propagation*, vol. 60, no. 7, July 2012, pp. 3389–3396.

[39] S. Priebe, M. Kannicht, M. Jacob, and T. Kürner, "Ultra broadband indoor channel measurements and calibrated ray tracing propagation modeling at THz frequencies," in *Journal of Communications and Networks*, vol. 15, no. 6, December 2013, pp. 547–558.

[40] M.-T. Martinez-Ingles, D. P. Gaillot, J. Pascual-Garcia, J.-M. Molina-Garcia-Pardo, M. Lienard, and J.-V. Rodriguez, "Deterministic and experimental indoor mmW channel modeling," in *IEEE Antennas and Wireless Propagation Letters*, vol. 13, May 2014, pp. 1047–1050.

[41] S. Sun, T. S. Rappaport, T. A. Thomas, and A. Ghosh, "A preliminary 3D mm wave indoor office channel model," in *International Conference on Computing, Networking and Communications (ICNC)*, February 2015, pp. 26–31.

[42] V. Degli-Esposti, F. Fuschini, E. Vitucci, M. Barbiroli, M. Zoli, L. Tian, X. Yin, D. Dupleich, R. Muller, C. Schneider, and R. Thomä, "Ray-tracing-based mm-Wave beamforming assessment," in *IEEE Access*, vol. 2, October 2014, pp. 1314–1325.

[43] C. Sturm, W. Sorgel, T. Kayser, and W. Wiesbeck, "Deterministic UWB wave propagation modeling for localization applications based on 3D ray tracing," in *IEEE MTT-S International Microwave Symposium Digest*, June 2006, pp. 2003–2006.

[44] C.-F. Yang, B.-C. Wu, and C.-J. Ko, "A ray-tracing method for modeling indoor wave propagation and penetration," in *IEEE Transactions on Antennas and Propagation*, vol. 46, no. 6, June 1998, pp. 907–919.

[45] Y. Wang, S. K. Chaudhuri, and S. Safavi-Naeini, "An FDTD/ray-tracing analysis method for wave penetration through inhomogeneous walls," in *IEEE Transactions on Antennas and Propagation*, vol. 50, no. 11, November 2002, pp. 1598–1604.

[46] H. Suzuki, "Accurate and efficient prediction of coverage map in an office environment using frustum ray tracing and in-situ penetration loss measurement," in *IEEE 57th Vehicular Technology Conference (VTC Spring)*, vol. 1, April 2003, pp. 236–240.

[47] F. Mani and C. Oestges, "A ray based indoor propagation model including depolarizing penetration," in *Proceedings of the 3rd European Conference on Antennas and Propagation (EuCAP)*, March 2009, pp. 3835–3838.

[48] A. Kausar, A. Reza, K. Noordin, M. Islam, and H. Ramiah, "Nearest object priority based integrated rough surface scattering algorithm for 3D indoor propagation prediction," in *China Communications*, vol. 11, no. 10, October 2014, pp. 147–158.

[49] C. Jansen, S. Priebe, C. Moller, M. Jacob, H. Dierke, M. Koch, and T. Kürner, "Diffuse scattering from rough surfaces in THz communication channels," in *IEEE Transactions on Terahertz Science and Technology*, vol. 1, no. 2, November 2011, pp. 462–472.

[50] F. Mani, F. Quitin, and C. Oestges, "Accuracy of depolarization and delay spread predictions using advanced ray-based modeling in indoor scenarios," in *EURASIP Journal on Wireless Communications and Networking*, vol. 2011, 2011, p. 11.

[51] E. M. Vitucci, F. Mani, C. Oestges, and V. Degli-Esposti, "Analysis and modeling of the polarization characteristics of diffuse scattering in indoor and outdoor radio propagation," in *International 21st Conference on Applied Electromagnetics and Communications (ICECom)*, October 2013, pp. 1–5.

[52] F. Mani and C. Oestges, "Evaluation of diffuse scattering contribution for delay spread and crosspolarization ratio prediction in an indoor scenario," in *Proceedings of the 4th European Conference on Antennas and Propagation (EuCAP)*, April 2010, pp. 1 – 4.

[53] F. Mani, F. Quitin, and C. Oestges, "Directional spreads of dense multipath components in indoor environments: Experimental validation of a ray-tracing approach," in *IEEE Transactions on Antennas and Propagation*, vol. 60, no. 7, July 2012, pp. 3389 – 3396.

[54] A. S. Abdellatif and S. Safavi-Naeini, "GPU accelerated channel modeling ray tracing tool," in *IEEE Radio and Wireless Symposium (RWS)*, January 2014, pp. 238–240.

[55] A. Navarro, D. Guevara, and N. Cardona, "Using game engines and graphic technologies for ray-tracing in future wireless," in *Proceedings of the 8th European Conference on Antennas and Propagation (EuCAP)*, April 2014, pp. 1780–1784.

[56] J. Tan, Z. Su, and Y. Long, "A full 3-D GPU-based beam-tracing method for complex indoor environments propagation modeling," in *IEEE Transactions on Antennas and Propagation*, vol. 63, no. 6, June 2015, pp. 2705–2718.

[57] T. Fugen, J. Maurer, T. Kayser, and W. Wiesbeck, "Capability of 3-D ray tracing for defining parameter sets for the specification of future mobile communications systems," in *IEEE Transactions on Antennas and Propagation*, vol. 54, no. 11, November 2006, pp. 3125–3137.

[58] T. Abbas, J. Nuckelt, T. Krner, T. Zemen, C. Mecklenbräuker, and F. Tufvesson, "Simulation and measurement based vehicle-to-vehicle channel characterization: Accuracy and constraint analysis," in *IEEE Transactions on Antennas and Propagation*, vol. 63, no. 7, July 2015, pp. 3208–3218.

[59] M. Janson, J. Pontes, C. Sturm, and T. Zwick, "BER simulations of a UWB spatial multiplexing system using an extended ray-tracing approach," in *IEEE Antennas and Wireless Propagation Letters,*, vol. 9, December 2010, pp. 1096–1098.

[60] M. Gan, F. Mani, F. Kaltenberger, C. Oestges, and T. Zemen, "A ray tracing algorithm using the discrete prolate spheroidal subspace," in *IEEE International Conference on Communications (ICC)*, June 2013, pp. 5710–5714.

[61] P. Meissner, M. Gan, F. Mani, E. Leitinger, M. Fröhle, C. Oestges, T. Zemen, and K. Witrisal, "On the use of ray tracing for performance prediction of UWB indoor localization systems," in *IEEE International Conference on Communications Workshops (ICC)*, June 2013, pp. 68–73.

[62] M. Gan, P. Meissner, F. Mani, E. Leitinger, M. Fröhle, C. Oestges, K. Witrisal, and T. Zemen, "Low-complexity sub-band divided ray tracing for UWB indoor channels," in *IEEE Wireless Communications and Networking Conference (WCNC)*, April 2014, pp. 305–310.

[63] ——, "Calibration of indoor UWB sub-band divided ray tracing using multiobjective simulated annealing," in *IEEE International Conference on Communications (ICC)*, June 2014, pp. 4844–4849.

[64] M. Gan, X. Li, F. Tufvesson, and T. Zemen, "An effective subdivision algorithm for diffuse scattering of ray tracing," in *XXXIth URSI General Assembly and Scientific Symposium (URSI GASS)*, August 2014, pp. 1–4.

[65] M. Gan, Z. Xu, V. Shivaldova, A. Paier, F. Tufvesson, and T. Zemen, "A ray tracing algorithm for intelligent transport systems in tunnels," in *IEEE 6th International Symposium on Wireless Vehicular Communications (WiVeC)*, September 2014, pp. 1–5.

[66] M. Gan, Z. Xu, M. Hofer, G. Steinböck, and T. Zemen, "A sub-band divided ray tracing algorithm using the DPS subspace in UWB indoor scenarios," in *IEEE 81st Vehicular Technology Conference (VTC-Spring)*, May 2015, pp. 1–5.

[67] G. Steinböck, M. Gan, P. Meissner, E. Leitinger, K. Witrisal, T. Zemen, and T. Pedersen, "Hybrid model for reverberant indoor radio channels using rays and graphs," in *IEEE Transactions on Antennas and Propagations*, 2015, submitted.

[68] S. U. Inan and S. A. Inan, *Electromagnetic Waves*. Prentice, 2000.

[69] R. Luebbers, "Finite conductivity uniform GTD versus knife edge diffraction in prediction of propagation path loss," in *IEEE Transactions on Antennas and Propagation*, vol. 32, no. 1, January 1984, pp. 70 – 76.

[70] C. Oestges, "Propagation modelling of low earh-orbit satellite personal communication systems," in *PHD dissertation*, December 2000.

[71] J. Keller, "Geometrical theory of diffraction," in *Journal of the optical society of America*, vol. 52, no. 2, February 1962, pp. 116–130.

[72] R. G. Kouyoumjian and P. H. Pathak, "A uniform geometrical theory of diffraction for an edge in a perfectly conducting surface," in *Proceedings of the IEEE*, vol. 62, no. 11, 1974, pp. 1448 – 1461.

[73] V. Degli-Esposti and H. L. Bertoni, "Evaluation of the role of diffuse scattering in urban microcellular propagation," in *IEEE 50th Vehicular Technology Conference (VTC Fall)*, vol. 3, September 1999, pp. 1392–1396.

[74] MathWorks, *MATLAB® Coder™ Getting Started Guide R2015a*. The MathWorks Inc., 2015.

[75] X. Li, "Efficient ray tracing simulation," in *Master dissertation*, April 2014.

[76] O. Franek, J. B. Andersen, and G. F. Pedersen, "Diffuse scattering model of indoor wideband propagation," in *IEEE Transactions on Antennas and Propagation*, vol. 59, no. 8, August 2011, pp. 3006–3012.

[77] P. Petrus, J. H. Reed, and T. S. Rappaport, "Geometrical-based statistical macrocell channel model for mobile environments," in *IEEE Transactions on Communications*, vol. 50, no. 3, March 2002, pp. 495–502.

[78] H. Chen, G. Wang, Z. Wang, H. C. So, and H. V. Poor, "Non-line-of-sight node localization based on semi-definite programming in wireless sensor networks," in *IEEE Transactions on Wireless Communications*, vol. 11, no. 1, January 2012, pp. 108 – 116.

[79] T. Öktem and D. Slock, "Power delay doppler profile fingerprinting for mobile localization in NLOS," in *IEEE 21st International Symposium on Personal Indoor and Mobile Radio Communications (PIMRC)*, September 2010, pp. 876 – 881.

[80] T. Callaghan, N. Czink, F. Mani, A. Paulraj, and G. Papanicolaou, "Correlation-based radio localization in an indoor environment," in *EURASIP Journal in Wireless Commmunications and Networking*, 2011.

[81] D. Slepian, "Prolate spheroidal wave functions, fourier analysis, and uncertainty - V:the discrete case," in *The Bell System Technical Journal*, vol. 57, no. 5, 1978, pp. 1371 – 1430.

[82] T. Zemen, "OFDM multi-user communication over time-variant channels," in *PHD dissertation*, July 2004.

[83] T. Zemen and C. Mecklenbräuker, "Time-variant channel estimation using discrete prolate spheroidal sequences," in *IEEE Transactions on Signal Processing*, vol. 53, no. 9, September 2005, pp. 3597–3607.

[84] F. Kaltenberger, T. Zemen, and C. W. Ueberhuber, "Low-complexity geometry-based MIMO channel simulation," in *EURASIP Journal on Advanced Signal Processing*, vol. 2007, 2007.

[85] F. Kaltenberger, "Low-complexity real-time signal processing for wireless communications," in *PHD dissertation*, May 2007.

[86] N. Czink, F. Kaltenberger, Y. Zhou, L. Bernadó, T. Zemen, and X. Yin, "Low-complexity geometry-based modeling of diffuse scattering," in *Proceedings of the 4th European Conference on Antennas and Propagation (EuCAP)*, April 2010, pp. 1 – 4.

[87] T. Zemen and A. F. Molisch, "Adaptive reduced-rank estimation of nonstationary time-variant channels using subspace selection," in *IEEE Transactions on Vehicular Technology*, vol. 61, no. 9, November 2012, pp. 4042 – 4056.

[88] G. Tiberi, S. Bertini, W. Q. Malik, A. Monorchio, D. J. Edwards, and G. Manara, "Analysis of realistic ultrawideband indoor communication channels by using an efficient ray-tracing based method," in *IEEE Transactions on Antennas and Propagation*, vol. 57, no. 3, March 2009, pp. 777 – 785.

[89] P. Meissner and K. Witrisal, "Analysis of position-related information in measured UWB indoor channels," in *Proceedings of the 6th European Conference on Antennas and Propagation (EuCAP)*, 2012, pp. 6–10.

[90] B. Alavi, N. Alsindi, and K. Pahlavan, "UWB channel measurements for accurate indoor localization," in *IEEE Military Communications Conference (MILCOM)*, 2006, pp. 1–7.

[91] A. Molisch, "Ultrawideband propagation channels-theory, measurement, and modeling," in *IEEE Transactions on Vehicular Technology*, vol. 54, no. 5, 2005, pp. 1528–1545.

[92] H. Sugahara, Y. Watanabe, T. Ono, K. Okanoue, and S. Yarnazaki, "Development and experimental evaluations of "RS-2000" - a propagation simulator for UWB systems," in *International Workshop on Ultra Wideband Systems, Joint with Conference on Ultrawideband Systems and Technologies (Joint UWBST IWUWBS)*, May 2004, pp. 76 – 80.

[93] J. Jemai, P. Eggers, G. F. Pedersen, and T. Kürner, "On the applicability of deterministic modelling to indoor UWB channels," in *Proceedings of the 3rd Workshop on Positioning, Navigation and Communication (WPNC)*, 2006.

[94] P. Meissner, E. Leitinger, M. Fröhle, and K. Witrisal. (2013) MeasureMINT. [Online]. Available: http://www.spsc.tugraz.at/tools/UWBmeasurements

[95] S. Priebe, M. Jacob, and T. Kürner, "Calibrated broadband ray tracing for the simulation of wave propagation in mm and sub-mm wave indoor communication channels," in *18th European Wireless Conference*, April 2012, pp. 1 – 10.

[96] J. Jemai, P. C. F. Eggers, G. F. Pedersen, and T. Kürner, "Calibration of a UWB sub-band channel model using simulated annealing," in *IEEE Transactions on Antennas and Propagation*, vol. 57, no. 10, 2009, pp. 3439–3443.

[97] T. Santos, J. Kåredal, P. Almers, F. Tufvesson, and A. F. Molisch, "Modeling the ultra-wideband outdoor channel: Measurements and parameter extraction method," in *IEEE Transactions on Wireless Communications*, vol. 9, no. 1, 2010, pp. 282–290.

[98] B. Suman and P. Kumar, "A survey of simulated annealing as a tool for single and multiobjective optimization," in *Journal of the Operational Research Society*, vol. 57, no. 10, 2005, pp. 1143–1160. [Online]. Available: http://dx.doi.org/10.1057/palgrave.jors.2602068

[99] A. Muqaibel, A. Safaai-Jazi, A. Bayram, A. M. Attiya, and S. M. Riad, "Ultra-wideband through-the-wall propagation," in *IEE Proceedings on Microwaves, Antennas and Propagation*, 2005, pp. 581–588.

[100] B. De Backer, H. Börjeson, D. De Zutter, and F. Olyslager, "Propagation mechanisms for UHF wave transmission through walls and windows," in *IEEE Transactions on Vehicular Technology*, vol. 52, no. 5, 2003, pp. 1297–1307.

[101] H. Suzuki and A. S. Mohan, "Measurement and prediction of high spatial resolution indoor radio channel characteristic map," in *IEEE Transactions on Vehicular Technology*, vol. 49, no. 4, 2000, pp. 1321–1333.

[102] J. Jemai, T. Kürner, A. Varone, and J.-F. Wagen, "Determination of the permittivity of building materials through WLAN measurements at 2.4 GHz," in *IEEE 16th International Symposium on Personal, Indoor and Mobile Radio Communications (PIMRC)*, vol. 1, 2005, pp. 589–593.

[103] W. Q. Malik, D. J. Edwards, and C. J. Stevens, "Angular-spectral antenna effects in ultra-wideband communications links," in *IEEE Proceedings on Communications*, vol. 153, no. 1, February 2006, pp. 99–106.

[104] L. Bernadó, T. Zemen, F. Tufvesson, A. F. Molisch, and C. Mecklenbräuker, "Delay and Doppler spreads of nonstationary vehicular channels for safety-relevant scenarios," in *IEEE Transactions on Vehicular Technology*, vol. 63, no. 1, January 2014, pp. 82–93.

[105] L. Bernadó, A. Roma, A. Paier, T. Zemen, N. Czink, J. Kåredal, A. Thiel, F. Tufvesson, A. F. Molisch, and C. F. Mecklenbräuker, "In-tunnel vehicular radio channel characterization," in *IEEE 73rd Vehicular Technology Conference (VTC Spring)*, May 2011, pp. 1–5.

[106] A. E. Forooshani, S. Bashir, D. G. Michelson, and S. Noghanian, "A survey of wireless communications and propagation modeling in underground mines," in *IEEE Communications Surveys Tutorials*, vol. 15, no. 4, Fourth Quarter 2013, pp. 1524–1545.

[107] A. Hrovat, G. Kandus, and T. Javornik, "A survey of radio propagation modeling for tunnels," in *IEEE Communications Surveys Tutorials*, vol. 16, no. 2, Second Quarter 2014, pp. 658–669.

[108] S.-H. Chen and S.-K. Jeng, "SBR image approach for radio wave propagation in tunnels with and without traffic," in *IEEE Transactions on Vehicular Technology*, vol. 45, no. 3, August 1996, pp. 570–578.

[109] M. H. Kermani and M. Kamarei, "A ray-tracing method for predicting delay spread in tunnel environments," in *IEEE International Conference on Personal Wireless Communication*, December 2000, pp. 538–542.

[110] D. Didascalou, T. M. Schafer, F. Weinmann, and W. Wiesbeck, "Ray-density normalization for ray-optical wave propagation modeling in arbitrarily shaped tunnels," in *IEEE Transactions on Antennas and Propagation*, vol. 48, no. 9, September 2000, pp. 1316–1325.

[111] F. M. Pallares, F. J. P. Juan, and L. Juan-Llacer, "Analysis of path loss and delay spread at 900 MHz and 2.1 GHz while entering tunnels," in *IEEE Transactions on Vehicular Technology*, vol. 50, no. 3, May 2001, pp. 767–776.

[112] J. Molina-Garcia-Pardo, J.-V. Rodriguez, and L. Juan-Llacer, "Wide-band measurements and characterization at 2.1 GHz while entering in a small tunnel," in *IEEE Transactions on Vehicular Technology*, vol. 53, no. 6, November 2004, pp. 1794–1799.

[113] Y. P. Zhang and Y. Hwang, "Characterization of UHF radio propagation channels in tunnel environments for microcellular and personal communications," in *IEEE Transactions on Vehicular Technology*, vol. 47, no. 1, February 1998, pp. 283–296.

[114] Y. P. Zhang, "Novel model for propagation loss prediction in tunnels," in *IEEE Transactions on Vehicular Technology*, vol. 52, no. 5, September 2003, pp. 1308–1314.

[115] S. F. Mahmoud, "On modal propagation of high frequency electromagnetic waves in straight and curved tunnels," in *IEEE Antennas and Propagation Society International Symposium*, vol. 3, June 2004, pp. 2963–2966.

[116] M. M. Rana and A. S. Mohan, "Segmented-locally-one-dimensional-FDTD method for EM propagation inside large complex tunnel environments," in *IEEE Transactions on Magnetics*, vol. 48, no. 2, February 2012, pp. 223–226.

[117] P. Bernardi, D. Caratelli, R. Cicchetti, V. Schena, and O. Testa, "A numerical scheme for the solution of the vector parabolic equation governing the radio wave propagation in straight and curved rectangular tunnels," in *IEEE Transactions on Antennas and Propagation*, vol. 57, no. 10, October 2009, pp. 3249–3257.

[118] A. Hrovat, G. Kandus, and T. Javornik, "Four-slope channel model for path loss prediction in tunnels at 400 MHz," in *IET Microwaves, Antennas and Propagation*, vol. 4, no. 5, May 2010, pp. 571–582.

[119] A. Paier, L. Bernadó, J. Kåredal, O. Klemp, and A. Kwoczek, "Overview of vehicle-to-vehicle radio channel measurements for collision avoidance applications," in *IEEE 71st Vehicular Technology Conference (VTC Spring)*, May 2010, pp. 1–5.

[120] A. V. B. da Silva and M. Nakagawa, "Radio wave propagation measurements in tunnel entrance environment for intelligent transportation systems applications," in *IEEE Intelligent Transportation Systems Proceedings*, August 2001, pp. 883–888.

[121] D. G. Dudley, M. Lienard, S. F. Mahmoud, and P. Degauque, "Wireless propagation in tunnels," in *IEEE Antennas and Propagation Magazine*, vol. 49, no. 2, April 2007, pp. 11–26.

[122] G. S. Ching, M. Ghoraishi, M. Landmann, N. Lertsirisopon, J.-I. Takada, T. Imai, I. Sameda, and H. Sakamoto, "Wideband polarimetric directional propagation channel analysis inside an arched tunnel," in *IEEE Transactions on Antennas and Propagation*, vol. 57, no. 3, March 2009, pp. 760–767.

[123] J. Alonso, S. Capdevila, B. Izquierdo, and J. Romeu, "Propagation measurements and simulations in tunnel environment at 5.8 GHz," in *IEEE Antennas and Propagation Society International Symposium*, July 2008, pp. 1–4.

[124] T. Pedersen, G. Steinböck, and B. H. Fleury, "Modeling of reverberant radio channels using propagation graphs," in *IEEE Transactions on Antennas and Propagation*, vol. 60, no. 12, December 2012, pp. 5978–5988.

[125] G. Matz, "Doubly underspread non-WSSUS channels: analysis and estimation of channel statistics," in *IEEE 4th Workshop on Signal Processing Advances in Wireless Communications*, June 2003, pp. 190–194.

[126] A. Paier, T. Zemen, L. Bernadó, G. Matz, J. Kåredal, N. Czink, C. Dumard, F. Tufvesson, A. F. Molisch, and C. F. Mecklenbräuker, "Non-WSSUS vehicular channel characterization in highway and urban scenarios at 5.2 GHz using the local scattering function," in *International ITG Workshop on Smart Antennas (WSA)*, February 2008, pp. 9–15.

[127] L. Bernadó, T. Zemen, A. Paier, J. Kåredal, and B. Fleury, "Parametrization of the local scattering function estimator for vehicular-to-vehicular channels," in *IEEE 70th Vehicular Technology Conference Fall (VTC Fall)*, September 2009, pp. 1–5.

[128] Z. Sun and I. F. Akyildiz, "Channel modeling and analysis for wireless networks in underground mines and road tunnels," in *IEEE Transactions on Communications*, vol. 58, no. 6, June 2010, pp. 1758–1768.

[129] C. Marshall, "The Øresund tunnel - making a success of design and build," in *Tunneling and Underground Space Technolody*, vol. 58, no. 3, 1999, pp. 355–365.

[130] C. Zhou, J. Waynert, T. Plass, and R. Jacksha, "Modeling RF propagation in tunnels," in *IEEE Antennas and Propagation Society International Symposium (APSURSI)*, July 2013, pp. 1916–1917.

[131] M. Walter, D. Shutin, and U.-C. Fiebig, "Delay-dependent doppler probability density functions for vehicle-to-vehicle scatter channels," in *IEEE Transactions on Antennas and Propagation*, vol. 62, no. 4, April 2014, pp. 2238–2249.

[132] T. Pedersen, G. Steinböck, and B. H. Fleury, "Modeling of outdoor-to-indoor radio channels via propagation graphs," in *XXXIth URSI General Assembly and Scientific Symposium (URSI GASS)*, August 2014, pp. 1–4.